Coiling Instability in Liquid and Solid Ropes

Mehdi Habibi

Département de Physique
de l'École Normale Supérieure

Laboratoire de Physique Statistique

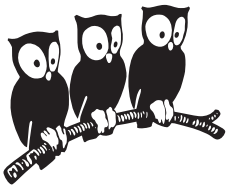

THÈSE DE DOCTORAT
DE L'UNIVERSITÉ PARIS 6 – PIERRE ET MARIE CURIE
Spécialité : Physique des Liquides

présentée par
Mehdi HABIBI

pour obtenir le grade de
DOCTEUR DE L'UNIVERSITÉ PARIS 6

Sujet de la thèse :

L'instabilité de Flambage Hélicoïdal de Filaments Liquides et Solides (Coiling Instability in Liquid and Solid Ropes)

Soutenue le 8 juin 2007 devant le jury composé de :

H. KELLAY	Rapporteur
J. R. LISTER	Rapporteur
B. AUDOLY	Examinateur
M. BEN AMAR	Examinateur
M. R. H. KHAJEPOUR	Examinateur
N. RIBE	Invité
R. GOLESTANIAN	Directeur de thèse
D. BONN	Directeur de thèse

Coiling Instability in Liquid and Solid Ropes

Advisors: Daniel Bonn & Ramin Golestanian

May 21, 2007

Acknowledgements

I would like to thank my supervisors, Daniel Bonn and Ramin Golestanian, from whom I have learned a lot. I have enjoyed a professional and insightful supervision by both of them, either directly or from the long distance. I am deeply indebted to them for their constant support, encouragement and helping through my research.

I also thank my advisor, Mohamad Reza Khajepour, who helped me a lot at IASBS.

I have benefitted from most fruitful collaborations on these problems with Neil Ribe and I wish to express my gratitude to him.

I am grateful to my colleagues, Maniya Maleki at IASBS and Peder Moller at Ecole Normale Superieure with whom I collaborated in doing the experiments in the laboratory, as well as having good time with them as very good friends.

I have also enjoyed helpful discussions with Jacques Meunier, Jens Eggers, Mokhtar Adda Bedia, Sebastien Moulinet, Dirk Aarts and Hamid Reza Khalesifard.

I wish to thank the hospitality of Ecole Normale Superieure in Paris and IASBS in Zanjan.

I would like to specially thank Bahman Farnudi, who was very kind and helped me, whenever I needed help. I also thank Nader S. Reyhani, Jafar M. Amjad, S. Rasuli and other people who help me for the experiments at IASBS.

I am grateful to Jens Eggers and the people of School of Mathematics at Bristol university, especially for their kind hospitality.

My visits to Paris were supported financially by the French embassy in Tehran, IASBS and LPS.

The Institute for Advanced Studies in Basic Sciences (IASBS) has served as a

wonderful place for scientific work as well as for an enjoyable life, throughout the course of my graduate studies. I wish to thank Y. Sobouti , the director, M.R.H. Kajehpour, the deputy, professors, students, and staff of the Institute, who created such an atmosphere with their coherent cooperations.

I had wonderful time with my friends during my studies at IASBS, namely Jaber Dehghani, Majid Abedi, Ehsan Jafari, Reza Vafabakhsh, Said Ansari, Alireza Akbari, Roohola Jafari, Davood Noroozi, Mohamad Charsooghi, Farshid Mohamadrafie and Sharareh Tavaddod and Didi Derks, Geoffroy Guena, Ulysse Delabre and Cristophe Chevalier at Ecole Normale Superieure, I wish to express my sincere gratitude to all of them.

Lastly, my special thanks go to: my family, who have always supported me during my life; Marzie my best friend, who has always been encouraging and helpful to me.

Preface

This thesis is a joint thesis work (thèse en co-tutelle) between the ENS Paris and the IASBS Zanjan.

Since fluid mechanics is a very large field with many applications, we set up a fluid dynamics laboratory at IASBS for doing experiments on wetting and viscous fluids. Daniel Bonn from the Ecole Normale Superieure in Paris helped us a lot to set up this laboratory. The experiments which are presented in this work were done at the Laboratoire de Physique Statistique (L.P.S) of Ecole Normale Superieure, and in the new fluid dynamics laboratory at IASBS.

This thesis is the result of a collaborative work which is evident also from the publications shown in the publication list at the end of the thesis. The Author collaborated with Maniya Maleki on the experiments related to Figs. 2.5 and 2.6 in chapter 2 and with Peder Moller on the experiments and the mathematical model of chapter 4. All the other experiments and data analysis were performed by the author. The numerical calculations and calculations of coiling frequency were performed by Neil Ribe; those in chapter 2, Figs. 2.8 and 2.9 and chapter 3, Fig. 3.3 were performed by the author using Ribe's code.

Contents

List of Figures

Chapter 1

Introduction

1.1 Introduction

A thin stream of honey poured from a sufficient height onto toast forms a regular coil. A similar phenomenon happens for a falling viscous sheet: it folds. Why does this happen, and what determines the frequency of coiling or folding? When pouring a viscous liquid on a solid surface, we encounter instabilities. A high viscosity can allow instabilities like buckling which normally happens only for solids, to happen for a liquid. In solid mechanics, the concept of buckling is an important and well-understood phenomenon. Buckling, which means the transition from a straight to a bent configuration due to the application a load, occurs because the straight configuration is not stable. This instability arises as a result of the competition between axial compression and bending in slender objects [1]. Within the realm of fluid mechanics, similar phenomena can be observed. An example is coiling of a thin stream of honey as it falls onto a flat plate. The spontaneous transition from a steady, stable flow to oscillations of parts of the jet column is called fluid buckling, in analogy with its counterpart in solid mechanics (Fig. 1.1).

When a vertical thin flexible rope falls on a horizontal surface such as a floor a similar phenomenon to liquid coiling is observed. This familiar phenomenon can also be reproduced at the lunch table when a spaghetti falls down into one's plate, (Fig. 1.2). When the rope reaches the surface it buckles and then starts to coil regularly.

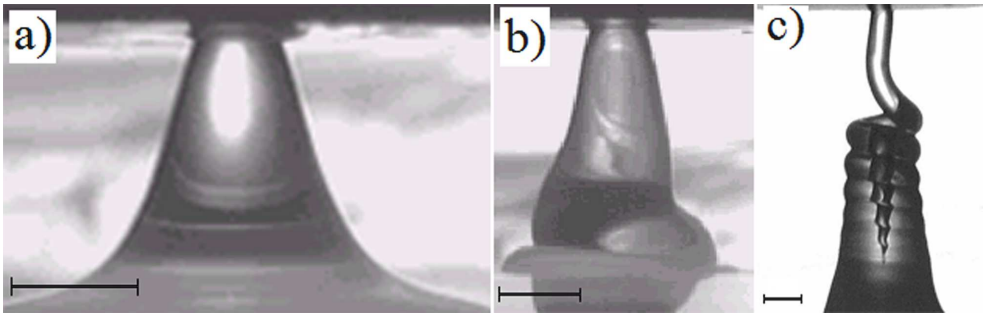

Figure 1.1: A viscous jet of silicon oil falling onto a plate. a) stable, unbuckled jet, b) buckled jet at critical height, c) coiling jet. The scale shown is 1 mm.

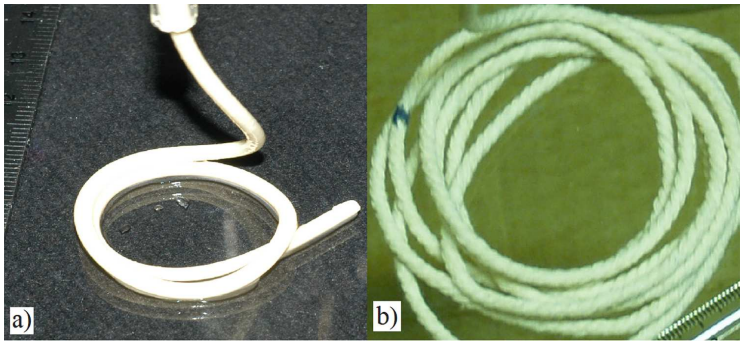

Figure 1.2: Coiling of elastic rope on solid surface. a) Spaghetti b) Cotton rope.

If the rope is fed continuously towards the surface from a fixed height its motion quickly settles down into a steady state in which the rope is laid out in a circular coil of uniform radius. The radius of the coil which depends on the height, stiffness and feeding velocity, determines the frequency of coiling.

1.2 Previous Works

The coiling instability of liquid filaments was called "liquid rope coiling" by Barnes & Woodcock (1958), whose pioneering work was the first in a series of experimental studies spanning nearly 50 years (Barnes & Woodcock 1958; Barnes & MacKenzie 1959; Cruickshank 1980; Cruickshank & Munson 1981; Huppert 1986; Griffiths & Turner 1988; Mahadevan *et al.* 1998). The first theoretical study of liquid rope

coiling was undertaken by Taylor [2], who suggested that the instability is similar to the buckling instability of an elastic rod (or solid rope) under an applied compressive stress. Subsequent theoretical studies based on linear stability analysis determined the critical fall height and frequency of incipient coiling [3, 4, 5]. They showed that the instability takes place for low Reynolds numbers and heights larger than a threshold height, which depends on the properties of the liquid (viscosity and surface tension). The nominal Reynolds number Ua_0/ν, must be multiplied by $(H/a_0)^2$ to account for different time scales for bending and axial motions, so the modified Reynolds number is $UH^2/a_0\nu$ [12].

1.2.1 Fluid Buckling

When a jet of a viscous liquid like honey is falling on a horizontal plate from a small height, it will smoothly connect to the horizontal surface (Fig. 1.1 (a)). In this case, the jet is stable. For a given flow rate and diameter, notably if the height exceeds a critical value H_c [5], the jet becomes unstable and will buckle (Figure 1.1 (b)). Buckled jet is unstable and cannot remain falling onto the same spot. It bends to the right or left and this causes a torque, which makes the jet continue to move on a circle and form a coil (Fig. 1.1 (c)).

A viscous jet can buckle, because it may be either in tension or compression, depending on the velocity gradient along its axis. If the diameter of the jet increases in the downstream direction, the viscous normal stress along its axis is one of compression. If this viscous compressive component of the normal stress is large enough, the net axial stress in the jet (including surface tension) may be compressive. Thus, near the flat plate, a sufficiently large axial compressive stress for a sufficiently slender jet can cause buckling [5, 6, 7].

The periodic buckling of a fluid jet incident on a surface is an instability with applications from food processing to polymer processing and geophysics [8, 9, 10, 11].

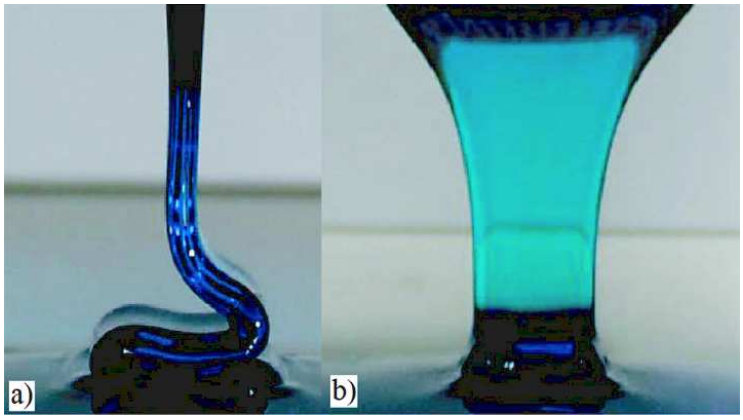

Figure 1.3: Periodic folding of a sheet of glucose syrup with viscosity μ=120 Pa s, viewed parallel to (a) and normal to (b) the sheet. The height of fall is 7.0 cm, and the dimensions of the extrusion slot are 0.7 cm×5.0 cm. Photographs by Neil Ribe, [14].

1.2.2 Liquid Folding

If instead of a liquid jet a liquid sheet is considered, the buckling takes the form of folding of the viscous sheet [12, 14, 15, 16]. (Fig. 1.3). In one's kitchen, this phenomenon is easily reproduced using honey, cake batter, or molten chocolate. The same instability is observed during the commercial filling of food containers [8], in polymer processing [9], and may occur in the earth when subducted oceanic lithosphere encounters discontinuities in viscosity and density at roughly 1000 km depth [10, 13]. Yet despite its importance, periodic folding of viscous sheets has proved surprisingly resistant to theoretical explanation. In 2003, Ribe numerically solved the asymptotic thin-layer equations for the combined stretching-bending deformation of a two-dimensional sheet to determine the folding frequency as a function of the sheets initial thickness, the pouring speed, the height of fall, and the fluid properties[14].

1.2.3 Liquid Coiling

Recently, Mahadevan et al. [17, 18] experimentally measured coiling frequencies of silicon oil in the high frequency or 'inertial' limit, and showed that they obey a scaling

law involving a balance between rotational inertia and the viscous forces that resist the bending of the rope. This behavior however is just one among several that are possible for liquid ropes. Ribe [19] proposed a numerical model for coiling based on asymptotic 'slender rope' theory, and solved the resulting equations using a numerical continuation method (see the Appendix for details). The solutions showed that three distinct coiling regimes (viscous, gravitational, and inertial) can exist depending on the relative magnitudes of the viscous, gravitational and inertial forces acting on the rope.

1.2.4 Elastic Rope Coiling

In 1996 Mahadevan and Keller [20, 21] numerically investigated the coiling of flexible ropes, they analyzed the problem as a geometrically nonlinear free boundary problem for a linear elastic rope. The stiffness and velocity of the rope and its falling height determine the coiling frequency; they solved the equations for the rope coiling by a numerical continuation method.

1.3 Scope of This Thesis

In this thesis, we present an experimental investigation of the coiling instability for both "liquid" and "solid" ropes and then compare the results with a numerical model for the instability.

In chapter 2, we study the coiling instability for a liquid thread. We report a detailed experimental study of the coiling instability of viscous jets on solid surfaces, including measuring the frequency of coiling, radii of the coil, and the jet and the maximum height of the coil and compare the results with the predictions of the numerical model of Ribe. We uncover three different regimes of coiling (viscous, gravitational and inertial) and present the experimental measurements of frequency vs. the height (from which the liquid is poured) in each regime. Finally, we describe "secondary buckling", which is the buckling of the column of the coils in high frequencies, and present measurements of the critical (buckling) height of the column.

In chapter 3 we investigate experimentally and theoretically a curious feature of this instability: the existence of multiple states with different frequencies at a fixed value of the fall height. In addition to the three coiling modes previously identified (viscous, gravitational, and inertial), we find a new multivalued "inertio-gravitational" coiling mode that occurs at heights intermediate between gravitational and inertial coiling. In the limit when the rope is strongly stretched by gravity, inertio-gravititational coiling occurs. The frequencies of the individual branches agree closely with the eigenfrequencies of a whirling liquid string with negligible resistance to bending and twisting. The laboratory experiments are in excellent agreement with predictions of the numerical model. Inertio-gravitational coiling is characterized by oscillations between states with different frequencies, and we present experimental observations of four distinct branches of such states in the frequency-fall height space. The transitions between coexisting states have no characteristic period, may take place with or without a change in the sense of rotation, and usually but not always occur via an intermediate figure of eight state. We show that between steps in the frequency vs. height curve we have unstable solution of the equations. Linear stability analysis shows that the multivalued portion of the curve of steady coiling frequency vs. height comprises alternating stable and unstable segments.

In chapter 4, we report that in a relatively small region in gravitational coiling regimes the buckling coil will trap air bubbles in a very regular way, and that these air bubbles will subsequently form surprising and very regular spiral patterns. We also present a very simple model that explains how these beautiful patterns are formed, and how the number of spiral branches and their curvature depends on the coiling frequency, the frequency of rotation of the coiling center, the total flow rate and the fluid film thickness.

In chapter 5 we present an experimental study of "solid rope coiling", we study the coiling of both real ropes and spaghetti falling or being pushed onto a solid surface. We show that three different regimes of coiling are possible; in addition to those suggested previously [20] by the numerics, for high speeds of the falling rope the coiling becomes dominated by inertial forces. We in addition provide a theoretical and numerical framework to understand and quantify the behavior of the ropes in

the different regimes, and relate the measured elastic properties of the materials to their coiling behavior, notably their coiling frequency. The numerical predictions are in excellent agreement with the experiments, showing that we have succeeded to quantitatively understand solid rope coiling also.

Chapter 2

Liquid Rope Coiling

2.1 Introduction

In this chapter, we report experiments covering the three regimes of coiling, with measurements of all the parameters necessary for a detailed comparison with the theory. We find that, as the fall height increases, the coiling frequency decreases and subsequently increases again, and we show that all of the results can be rescaled in a universal way that allows us to predict for instance the frequency of coiling of honey on your morning toast. Finally we describe the secondary buckling, which is the buckling of the column of the coils in high frequencies, and present measurements of the critical (buckling) height of the column.

2.2 Experimental System and Techniques

Fig. (2.1) shows a schematic view of the the experiment, in which fluid with density ρ, kinematic viscosity ν and surface tension γ is injected at a volumetric rate Q from a hole of diameter $d = 2a_0$ and then falls a distance H onto a solid surface. In general, the rope comprises a long, nearly vertical "tail" and a helical "coil" of radius R near the plate. For convenience, we characterize each set of experiment by its associated

values of the dimensionless parameters Π_1, Π_2 and Π_3 which are defined as [34, 35]:

$$\Pi_1 = \left(\frac{\nu^5}{gQ^3}\right)^{1/5}, \tag{2.1}$$

$$\Pi_2 = \left(\frac{\nu Q}{gd^4}\right)^{1/4}, \tag{2.2}$$

$$\Pi_3 = (\frac{\gamma d^2}{\rho \nu Q}). \tag{2.3}$$

We used two different experimental setups for low frequency and high-frequency coiling experiments. In both cases, silicone oil with density ρ =0.97 g cm^{-3}, surface tension γ =21.5 dyn cm^{-1}, and variable kinematic viscosity ν was injected at a volumetric rate Q from a hole of diameter $d = 2a_0$ and subsequently fell a distance H onto a glass plate. The advantage of the silicon oil is that it can have different kinematic viscosity with the same density and surface tension. We can change the kinematic viscosity in a very wide range. (Between 100 to 5000 cm^2 s^{-1} for our experiments.)

To study low-frequency coiling, we used an experimental apparatus schematically shown in Fig. 2.2 (a), in which a thin rope of silicone oil is extruded downward from a syringe pump by a piston driven by a computer controlled stepper motor. In a typical experiment, the fluid was injected continuously at a constant rate Q while the fall height H was varied over a range of discrete values, sufficient time being allowed at each height to measure the coiling frequency by taking a movie with a CCD camera coupled to a computer. This arrangement allowed access to the very low flow rates required to observe both low frequency viscous coiling and the multivalued inertio-gravitational coiling with more than two distinct branches discussed in detail below. The hole diameter could be changed by attaching tubes at different diameters to the syringe. The flow rate was measured to within 10^{-4} cm^{3}s^{-1} by recording the volume of fluid in the syringe as a function of time. A CCD camera operating at 25 frames/s was used to make movies, from which the radius could be determined directly and the coiling frequency was measured by frame counting. The radius of the rope and the fall height especially for small fall heights were measured on the still images to

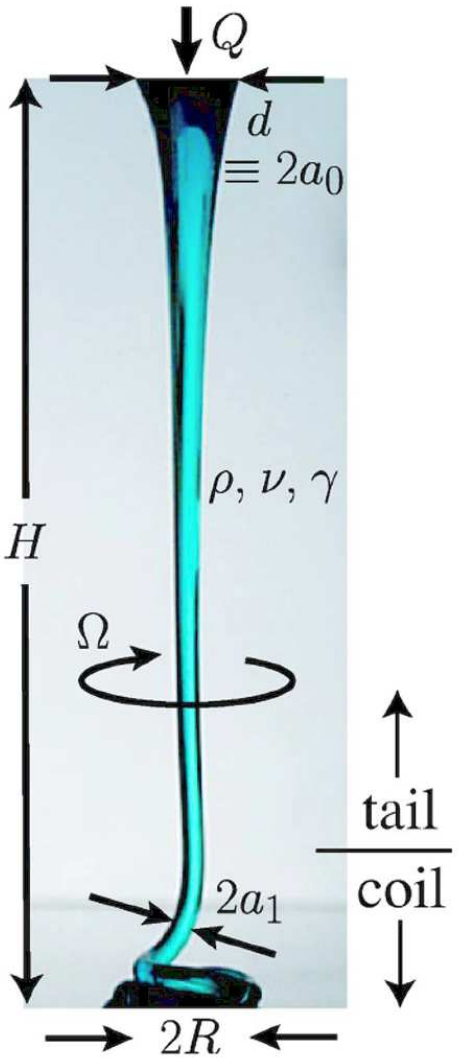

Figure 2.1: Coiling of a jet of viscous corn syrup (photograph by Neil Ribe), showing the parameters of a typical laboratory experiment.

within 0.02 and 0.2 mm, respectively. For large heights we used a ruler to determine H to within 1 mm.

In the setup used to study high-frequency coiling Fig. 2.2 (b), silicone oil with viscosity ν =300 $\mathrm{cm^2 s^{-1}}$ fell freely from a hole of radius a_0=0.25 cm at the bottom of a reservoir. To maintain a constant flow rate Q, the reservoir was made to overflow continually by the addition of silicone oil from a second beaker. Three series of experiments were performed with flow rates Q=0.085, 0.094, and 0.104 $\mathrm{cm^3 s^{-1}}$ and fall heights 2.0-49.4 cm. The coiling frequency was measured by frame counting on movies taken with a high speed camera operating at 125 - 1000 frames/s, depending on the temporal resolution required. The flow rate was measured to within 1 % by weighing the amount of oil on the plate as a function of time during the experiment. The radius a_1 of the rope just above the coil was measured from still pictures taken with a high resolution Nikon digital camera with a macro objective and a flash to avoid motion blur.

For both setups, the fall height H was varied using a mechanical jack. The values of H reported here are all effective values, measured from the orifice down to the point where the rope first comes into contact with a previously extruded portion of itself. The effective fall height H is thus the total orifice-to-plate distance less the height of the previously extruded fluid that has piled up beneath the falling rope. Anticipating the possibility of hysteresis, we made measurements both with height increasing and decreasing, and in a few cases we varied the height randomly.

2.3 Regimes of Coiling

The motion of a coiling jet is controlled by the balance between viscous forces, gravity and inertia. Viscous forces arise from internal deformation of the jet by stretching (localized mainly in the tail) and by bending and twisting (mainly in the coil). Inertia includes the usual centrifugal and Coriolis accelerations, as well as terms proportional to the along-axis rate of change of the magnitude and direction of the axial velocity.

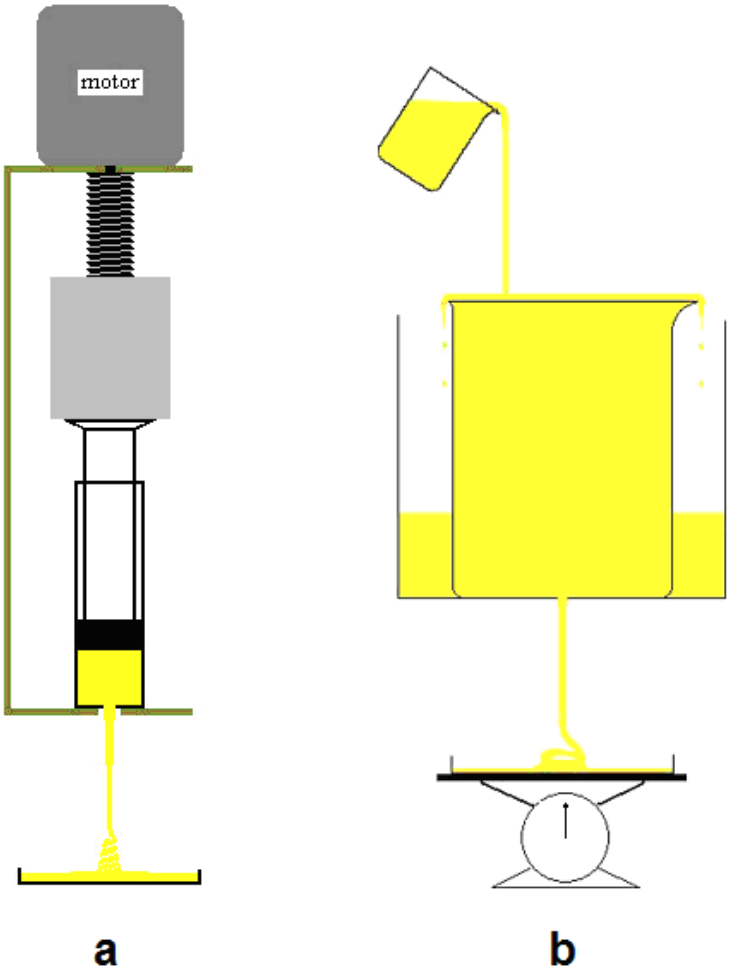

Figure 2.2: Experimental setups for: (a) low coiling frequencies, (b) high coiling frequencies.

The dynamical regime in which coiling takes place is determined by the magnitudes of the viscous (F_V), gravitational (F_G) and inertial (F_I) forces per unit rope length within the coil. These are (Mahadevan *et al.* 2000, Ribe 2004)

$$F_V \sim \rho\nu a_1^4 U_1 R^{-4}, \quad F_G \sim \rho g a_1^2, \quad F_I \sim \rho a_1^2 U_1^2 R^{-1}, \tag{2.4}$$

where a_1 is the radius of the rope within the coil and $U_1 \equiv Q/\pi a_1^2$ is the corresponding axial velocity of the fluid. Because the rope radius is nearly constant in the coil, we define a_1 to be the radius at the point of contact with the plate. Each of the forces (2.4) depends strongly on a_1, which in turn is determined by the amount of gravity-induced stretching that occurs in the tail. Because this stretching increases strongly with the height H, the relative magnitudes of the forces F_V, F_G and F_I are themselves functions of H. As H increases, the coiling traverses a series of distinct dynamical regimes characterized by different force balances in the coil. Fig. 2.3 shows how these regimes show up in curves of $\Omega(H)$, the frequency of coiling and $a_1(H)$ the radius of the rope, for one set of experimental parameters. These curves were determined by solving numerically the thin-rope equations of Ribe (2004). In Fig. 2.3 for simplicity, we neglected surface tension, which typically modifies the coiling frequency by no more than a few percent for a surface tension coefficient $\gamma \approx 21.5$ dyne cm^{-1} typical of silicone oil. We have included surface tension effect in most of our numerical calculations. Surface tension is however important in related phenomena such as the thermal bending of liquid jets by Marangoni stresses (Brenner & Parachuri 2003).

We observe that different modes of coiling are possible, depending on how the three forces in the coil are balanced. For small dimensionless heights $H(g/\nu^2)^{1/3} < 0.08$, coiling occurs in the viscous (V) regime, in which both gravity and inertia are negligible and the net viscous force on each fluid element is zero. Coiling is here driven entirely by the injection of the fluid, like toothpaste squeezed from a tube. Because the jet deforms by bending and twisting with negligible stretching, its radius is nearly constant, Therefore, $a_1 \approx a_0$ and $U_1 \approx U_0$. Fig. 2.4 (a,e). We observe that, for very small height the rope is slightly compressed against the fluid pile as shown in Fig. 2.5.

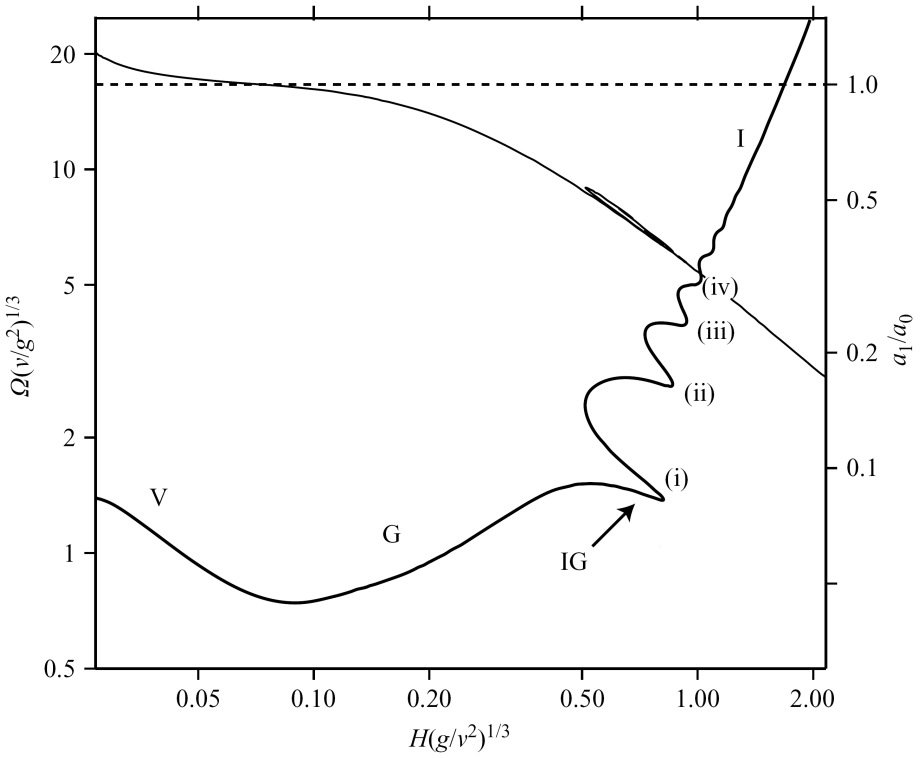

Figure 2.3: Dimensionless coiling frequency $\Omega d^3/Q$ (heavy solid line, left scale) and rope radius a_1/a_0 (light solid line, right scale) as a function of dimensionless fall height $H(g/\nu^2)^{1/3}$, predicted numerically for $\Pi_1 = 7142$ and $\Pi_2 = 3.67$. Dashed line at $a_1/a_0 = 1$ is for reference. Portions of the heavy solid line representing the different coiling regimes are labelled: viscous (V), gravitational (G), inertio-gravitational (IG), and inertial (I).

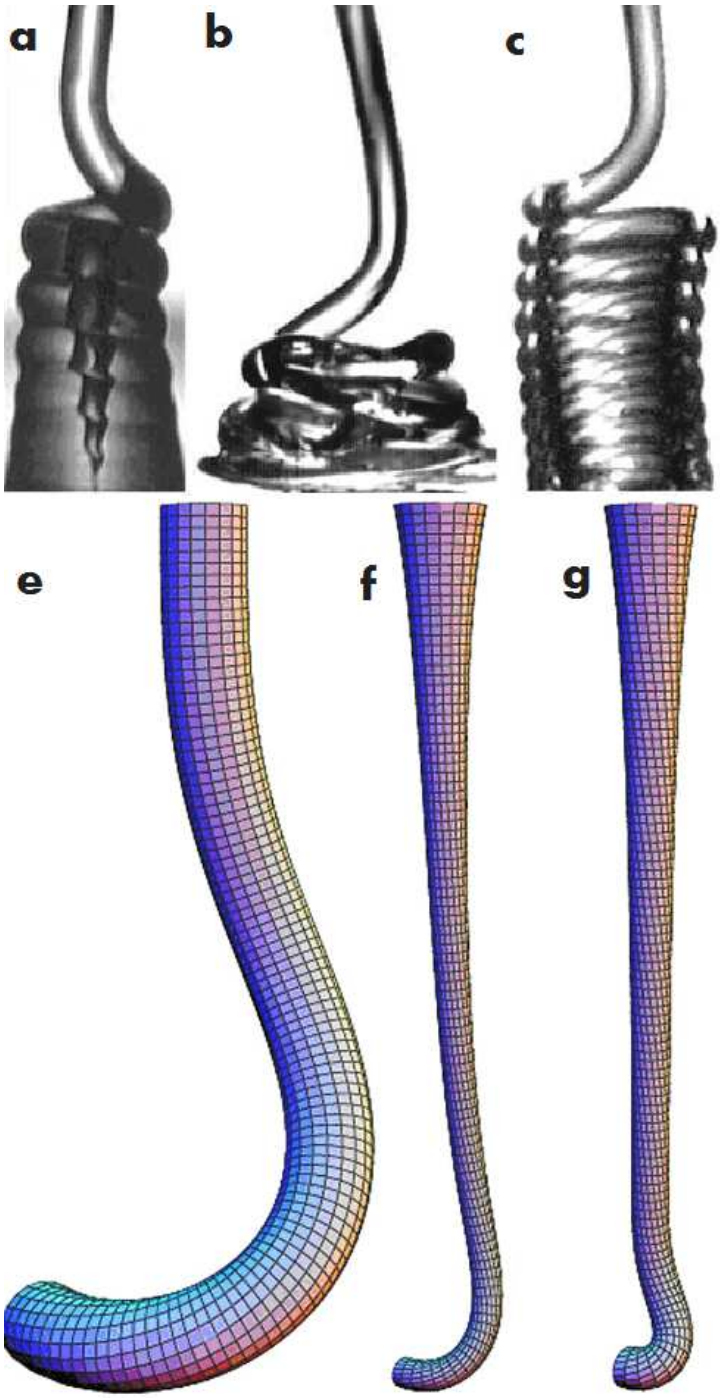

Figure 2.4: Different coiling regimes. (a) Viscous regime: coiling of silicone oil with $\nu = 1000$ cm^2/s, injected from an orifice (top of image) of radius $a_0 = 0.034$ cm at a volumetric rate $Q = 0.0044$ cm^3/s. Effective fall height $H = 0.36$ cm. (b) Gravitational regime: coiling of silicone oil with $\nu = 300$ cm^2/s, falling from an orifice of radius $a_0 = 0.25$ cm at a flow rate $Q = 0.093$ cm^3/s. Fall height is 5 cm. The radius of the portion of the rope shown is 0.076 cm. (c) Inertial regime: coiling of silicone oil with $\nu = 125$ cm^2/s, $a_0 = 0.1$ cm, $Q = 0.213$ cm^3/s and $H = 10$ cm. The radius a_1 is 0.04 cm. (e)-(g) Jet shapes calculated using Auto97 (Doedel et al. 2002) for three modes of fluid coiling [19]. (e) Viscous coiling. (f) Gravitational coiling. (g) Inertial coiling.

Figure 2.5: Rope of silicon oil with $\nu = 1000$ cm^2/s, injected from an orifice of radius $a_0 = 0.034$ cm at a volumetric rate $Q = 0.0044$ cm^3/s and effective fall height $H = 0.30$ cm. is slightly compressed against the plate, so the diameter at bottom is larger than the diameter of the filament near the nuzzle.

Dimensional considerations (Ribe 2004) and the general relation $\Omega \sim U_1/R$ then imply

$$R \sim H \quad , \quad \Omega_V = \frac{Q}{Ha_1^2}. \tag{2.5}$$

After the viscous coiling regime, $0.08 \leq H(g/\nu^2)^{1/3} \leq 0.4$, when inertia is negligible, viscous forces in the coil are balanced by gravity ($F_G \approx F_V \gg F_I$), giving rise to gravitational (G) coiling. Fig. 2.4(b,f). The scaling laws for this mode are (Ribe 2004)

$$\rho\nu a_1^4 U_1 R^{-4} \sim \rho g a_1^2 \tag{2.6}$$

$$R \sim g^{-1/4}\nu^{1/4}Q^{1/4} \equiv R_G, \qquad \Omega \sim g^{1/4}\nu^{1/4}a_1^{-2}Q^{3/4} \equiv \Omega_G \tag{2.7}$$

which is identical to the typical frequency for the folding of a rope confined to a plane (Skorobogatiy and Mahadevan 2000). The rope's radius is nearly constant ($a_1 \approx a_0$) at the lower end ($0.08 \leq H(g/\nu^2)^{1/3} \leq 0.15$) of the gravitational regime, implying the seemingly paradoxical conclusion that gravitational stretching in the tail can be negligible in "gravitational" coiling. This apparent paradox is resolved by noting that for a given strain rate, the viscous forces associated with bending and twisting of a slender rope are much smaller than those that accompany stretching.

The influence of gravity is therefore felt first in the (bending/twisting) coil and only later in the (stretching) tail, and thus can be simultaneously dominant in the former and negligible in the latter.

When the height gradually increases to $H(g/\nu^2)^{1/3} \approx 1.2$, a third mode, 'inertial' coiling is observed. (Fig. 2.4(c,g)). Viscous forces in the coil are now balanced almost entirely by inertia ($F_I \approx F_V \gg F_G$), giving rise to inertial (I) coiling with this scaling law: (Mahadevan *et al.* 2000)

$$\rho\nu a_1^4 U_1 R^{-4} \sim \rho a_1^2 U_1^2 R^{-1}. \tag{2.8}$$

The radius and frequency for this mode are proportional to

$$R \sim \nu^{1/3} a_1^{4/3} Q^{-1/3} \equiv R_I, \qquad \Omega \sim \nu^{-1/3} a_1^{-10/3} Q^{4/3} \equiv \Omega_I. \tag{2.9}$$

For $0.4 \leq H(g/\nu^2)^{1/3} \leq 1.2$, viscous forces in the coil are balanced by both gravity and inertia, giving rise to a complex transitional regime "inertio-gravitational" (IG) The curve of frequency vs. height is now multivalued. We will concentrate on this part in the next chapter and only discuss the results for the three "pure" regimes here.

2.4 Frequency versus height

2.4.1 Viscous-Gravitational Transition

Fig. 2.6(a) shows the angular coiling frequency Ω (circles) as a function of height measured using the first setup with $Q = 0.0038$ cm^3/s. The frequency decreases as a function of height for $0.25 < H < 0.8$ cm, and then saturates or increases slightly thereafter. The behavior for $0.25 < H < 0.8$ cm is in agreement with the scaling law 2.5 for viscous coiling, which predicts $\Omega \propto H^{-1}$, shown as the dashed line in Fig.

2.6(a). For comparison, the solid line shows the coiling frequency predicted numerically for the parameters of the experiment, including the effect of surface tension. The trends of the numerical curve and of the experimental data are in good agreement, although the latter are 15%-20% lower on average for unknown reasons. The rapid increase of frequency with height predicted by the numerical model for $H < 0.25$ cm corresponds to coiling states in which the rope is strongly compressed against the plate. We were unable to observe such states because the rope coalesced rapidly with the pool of previously extruded fluid flowing away from it.

In this regime, the coiling frequency is independent of viscosity and depends only on the geometry and the flow rate even though the fluid's high viscosity is what makes coiling possible in the first place (water does not coil). The physical reason for this rather surprising behavior is that the velocity in the rope is determined purely kinematically by the imposed injection rate. This ceases to be the case for fall heights $H > 0.8$ cm for which the influence of gravity becomes significant, as we demonstrate below.

Now we want to rescale the axes of the frequency-height curve to obtain a universal curve for viscous-gravitational transition. We anticipate that the control parameter for this transition will be the ratio of the characteristic frequencies Ω_G and Ω_V of the two modes, defined by equations 2.7 and 2.5. Accordingly, a log-log plot of Ω/Ω_V versus $\Omega_G/\Omega_V = H(g/\nu Q)^{1/4}$ should give a universal curve, where viscous and gravitational coiling are represented by segments of slope zero and unity, respectively. To test this, we compare all of the experimental data obtained using the first setup with the theoretically predicted universal curve in Fig. 2.7 (a). Segments of slope zero and unity are clearly defined by the rescaled measurements, although the latter are again 15%-20% lower than the numerical predictions.

2.4.2 Gravitational-Inertial Transition

For larger fall heights, both gravitational and inertial forces are important. Fig. 2.6(b) shows the frequency versus height curve measured using the second setup with $Q = 0.094$ cm^3/s. As we will see below, the low frequencies correspond to

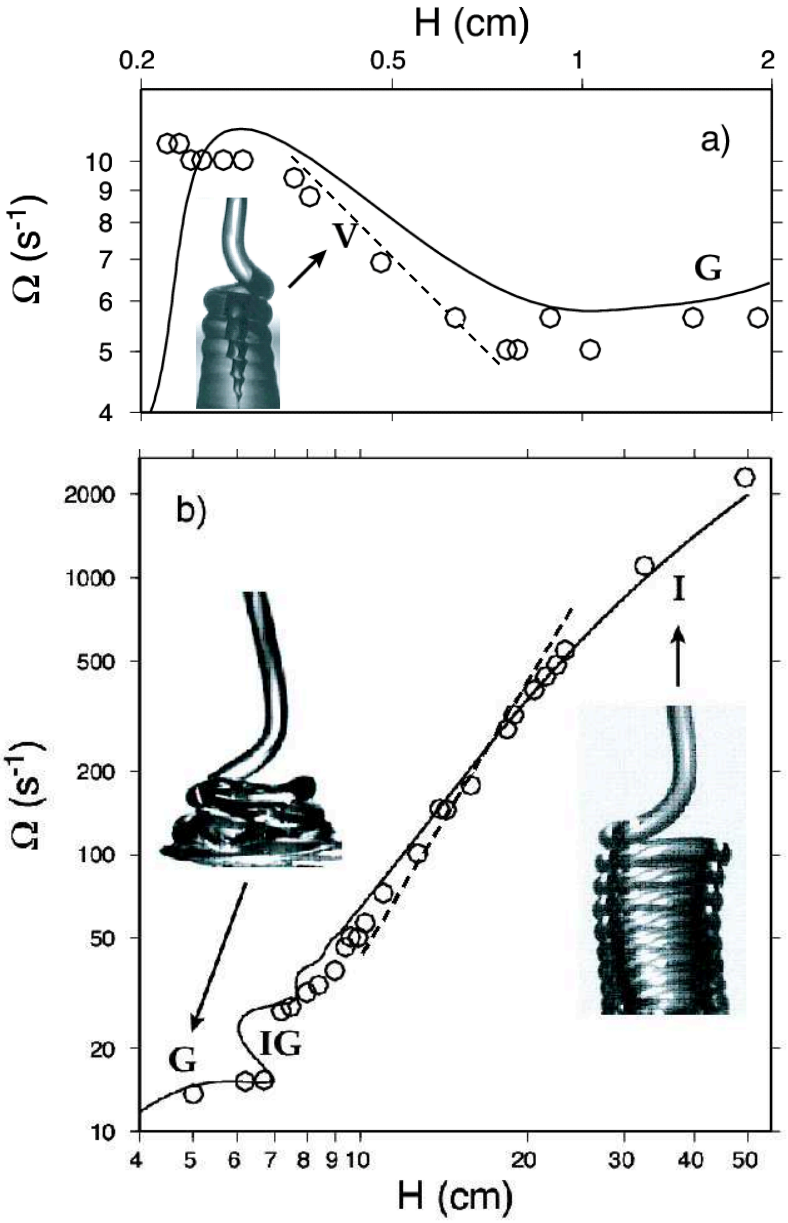

Figure 2.6: Curves of angular coiling frequency vs fall height showing the existence of four distinct coiling regimes: Viscous V, gravitational G, inertio-gravitational IG, and inertial I. Experimental measurements are denoted by circles and numerical calculations based on slender-rope theory by solid lines. Error bars on the experimental measurements of Ω and H are smaller than the diameter of the circles in most cases. The typical appearance of the coiling rope in the V, G, and I regimes is shown by the inset photographs. a) Slow inertia-free coiling with ν =1000 cm^2/s, $a_0 = 0.034$ cm, and $Q = 0.0038$ cm^3/s. The dashed line shows the simplified viscous coiling scaling law 2.5. b) High-frequency coiling with ν =300 cm^2/s, $a_0 = 0.25$ cm, and $Q = 0.094$ cm^3/s. The dashed line shows the inertial coiling scaling law 2.9.

gravitational coiling, and the high frequencies to inertial coiling. These data show two remarkable features. First, and contrary to what happens in the viscous regime, the coiling frequency increases with increasing height. Second, there appears to be a discontinuous jump in the frequency at $H \approx 7$ cm, we will discuss it in detail in next chapter.

The increase of frequency with height in the inertial regime can be understood qualitatively as follows. From equation 2.9, we expect $\Omega \propto a_1^{10/3}$ in the inertial regime. The (a priori unknown) radius a_1 is in turn controlled by the amount of gravitational thinning that occurs in the 'tail' of the falling rope, above the helical coil. Now the dominant forces in the coil and in the tail need not be the same: indeed, in many of our inertial coiling experiments, inertia is important in the coil but relatively minor in the tail, where gravity is balanced by viscous resistance to stretching. In the limit $a_1 \ll a_0$ corresponding to strong stretching, this force balance (Ribe 2004) implies

$$a_1 \propto (Q\nu/g)^{1/2} H^{-1}, \tag{2.10}$$

which when combined with equation 2.9 yields:

$$\Omega_I \propto H^{10/3}, \tag{2.11}$$

which is shown by the dashed line in Fig. 2.6 (b), and is in reasonable agreement with the experimental measurements. The latter agree still more closely with the full numerical solution (solid line), which includes additional terms that were neglected in the simple scaling analysis leading to equation 2.11. The steady decrease in the slope of $\Omega(H)$ for $H > 20$ cm is due to the increasing effect of inertia in the tail of the rope, which inhibits gravitational stretching and increases a_1 relative to the value predicted by equation 2.10.

By the same way as viscous-gravitational transition, there should exist a universal curve describing the transition from gravitational to inertial coiling as H increases. Fig. 2.7(b) shows a log-log plot of Ω/Ω_G versus Ω_I/Ω_G for our experimental data (symbols), together with the numerical prediction (solid line). The agreement is

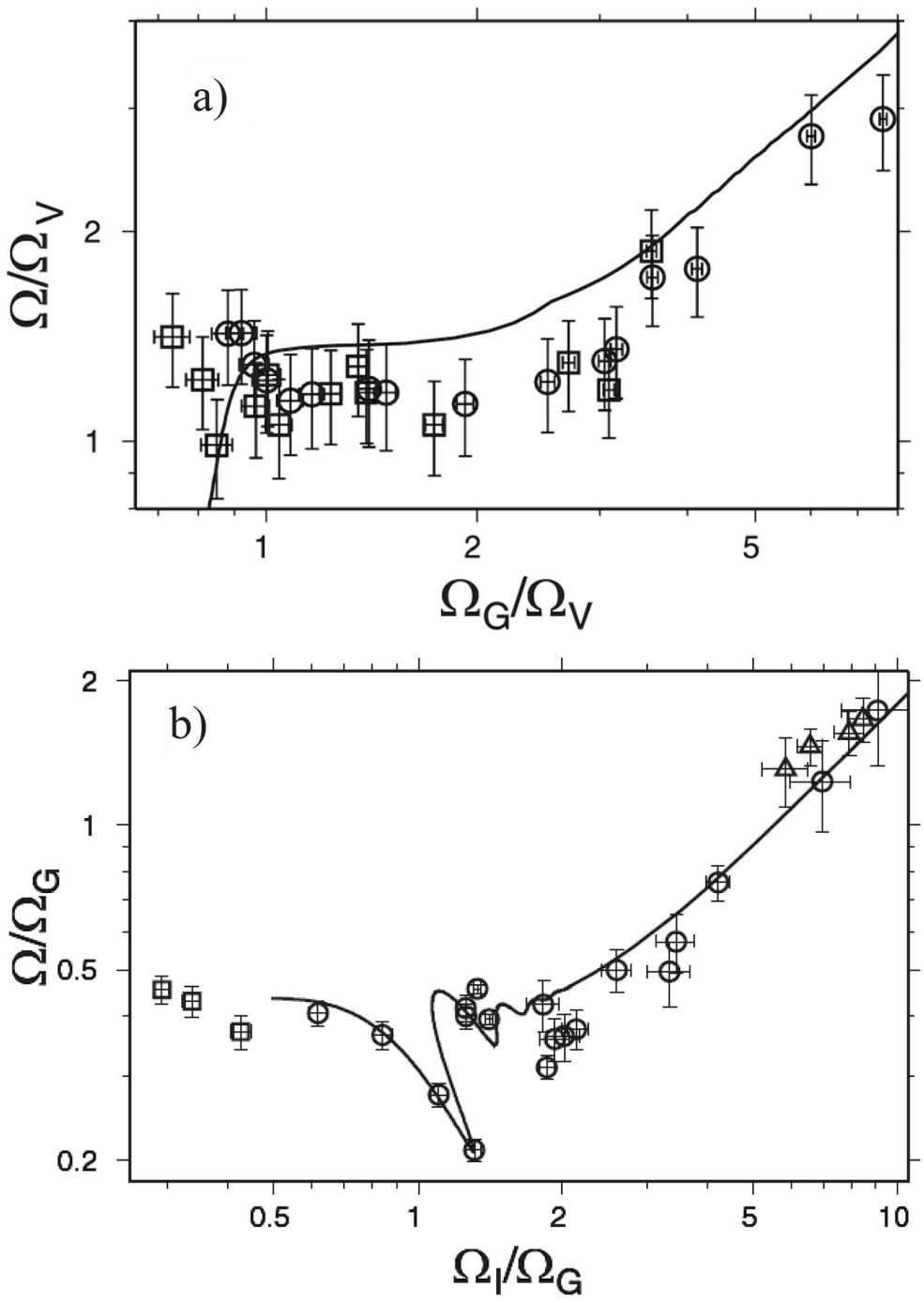

Figure 2.7: a) Transition from viscous to gravitational coiling. Rescaled coiling frequency using the scales Ω_V and Ω_G, for an experiment performed using the low-frequency setup with $\nu = 1000$ cm^2/s, $d = 0.068$ cm, and $Q = 0.0038$ cm^3/s (circle),$Q = 0.0044$ cm^3/s (squares). Solid line: prediction of the slender-rope numerical model for $\nu = 1000$ cm^2/s, $d = 0.068$ cm, and $Q = 0.0038$ cm^3/s. Numerical predictions for $Q = 0.0044$ cm^3/s is very similar and close to this curve. Portions of the solid curve with slopes zero (left) and unity (right) correspond to viscous and gravitational coiling, respectively. Error bars primarily reflect uncertainty in estimation of a_1. b) Transition from gravitational to inertial coiling. Rescaled parameters using the scales Ω_G and Ω_I . Results are shown for experiments with $\nu = 300$ cm^2/s, $d = 0.5$ cm, $Q = 0.094$ cm^3/s (circles), 0.085 cm^3/s (squares) and 0.104 cm^3/s (triangles). Solid line: prediction of the slender-rope numerical model for ν =300 cm^2/s, $a_0 = 0.25$ cm, and $Q = 0.094$ cm^3/s. Numerical predictions for $Q = 0.085$ and 0.104 cm^3/s is very similar and close to this curve. Portions of the solid curve with slopes zero and unity correspond to gravitational and inertial coiling, respectively.

very good, especially in the transition regime between gravitational coiling (constant Ω/Ω_G) and inertial coiling ($\Omega/\Omega_G \propto \Omega_I/\Omega_G$). Evidently the gravitational-inertial transition, such as the viscous-gravitational one, can be rescaled in such a way that the behavior is universal.

2.5 Prediction of the Coiling Frequency of Honey at the Breakfast Table

We conclude by using our results to predict the frequency of inertial coiling of honey on toast. Fig. 2.8 (a). For typical viscosity and falling height of honey on toast at breakfast table the coiling usually happens in inertial regime. A complete scaling law for the frequency in terms of the known experimental parameters is obtained by combining the inertial coiling law $\Omega \sim 0.18\Omega_I$ with a numerical solution for a_1 valid when $a_1 \ll a_0$. Ribe's calculations [31] yields:

$$\Omega = 0.0135 g^{5/3} Q^{-1/3} \nu^{-2} [\frac{H}{K(gH^3/\nu^2)}]^{10/3} \tag{2.12}$$

Where the function K is shown in Fig. 2.8 (b). To test this law, we measured the coiling frequency of honey ($\nu = 350$ cm^2/s) falling a distance $H = 7$ cm at a rate Q= 0.08 cm^3/s onto a rigid surface. The measured frequency was 16 s^{-1}, while that predicted with the help of equation 2.12 is 15.8 s^{-1}.

2.6 Radius of the Coil and the Rope

The equation (2.1) shows that the forces per unit length acting on the rope depend critically on the radius R of the coil and the radius a_1 of the rope within the coil. Here we present a systematic series of laboratory measurements of R and a_1, and compare them to the predictions of Ribe's slender-rope numerical model (Appendix). Most previous experimental studies of liquid rope coiling have focussed on measuring

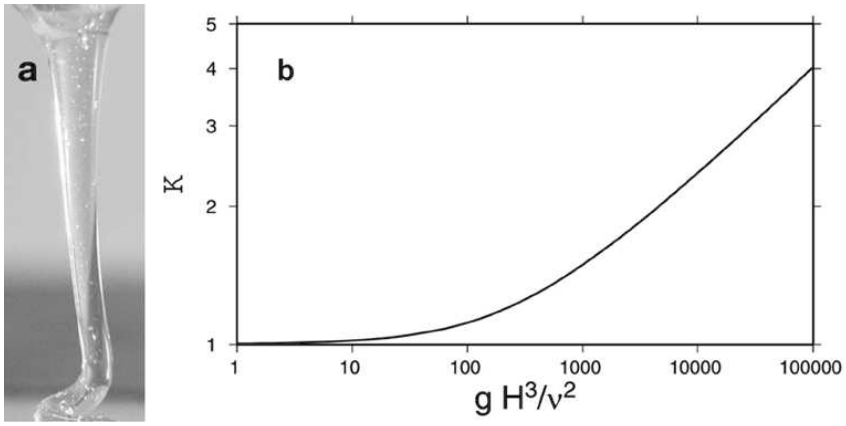

Figure 2.8: Examples of liquid rope coiling. (a) Coiling of honey (viscosity $\nu = 60$ cm^2/s) falling a distance $H = 3.4$ cm. (b) Function K in equation 2.12. $K(x \to \infty) \sim (2x)^{1/4}/(\sqrt{3}\pi)$

the coiling frequency. Only a few experiments [17, 31] have measured the radius a_1 in addition, and none (to our knowledge) has presented measurements of the coil radius R.

The measurements we present here were obtained in eight experiments with different values of ν, d, and Q [32].

2.6.1 Radius of the Coil

Fig. 2.9 shows the coil radius R as a function of the height for the eight experiments. The agreement between the measured values and the numerics (with no adjustable parameters) is very good overall. The coil radius is roughly constant in the gravitational regime, which is represented by the relatively flat portions of the numerical curves at the left of panels b, c, d, e, g, and h. The subsequent rapid increase of the coil radius with height corresponds to the beginning of the inertio-gravitational regime. At greater heights within the inertio-gravitational regime, the coil radius exhibits a multivalued character similar to the one we have already seen for the frequency (e.g., Fig. 2.6 b).

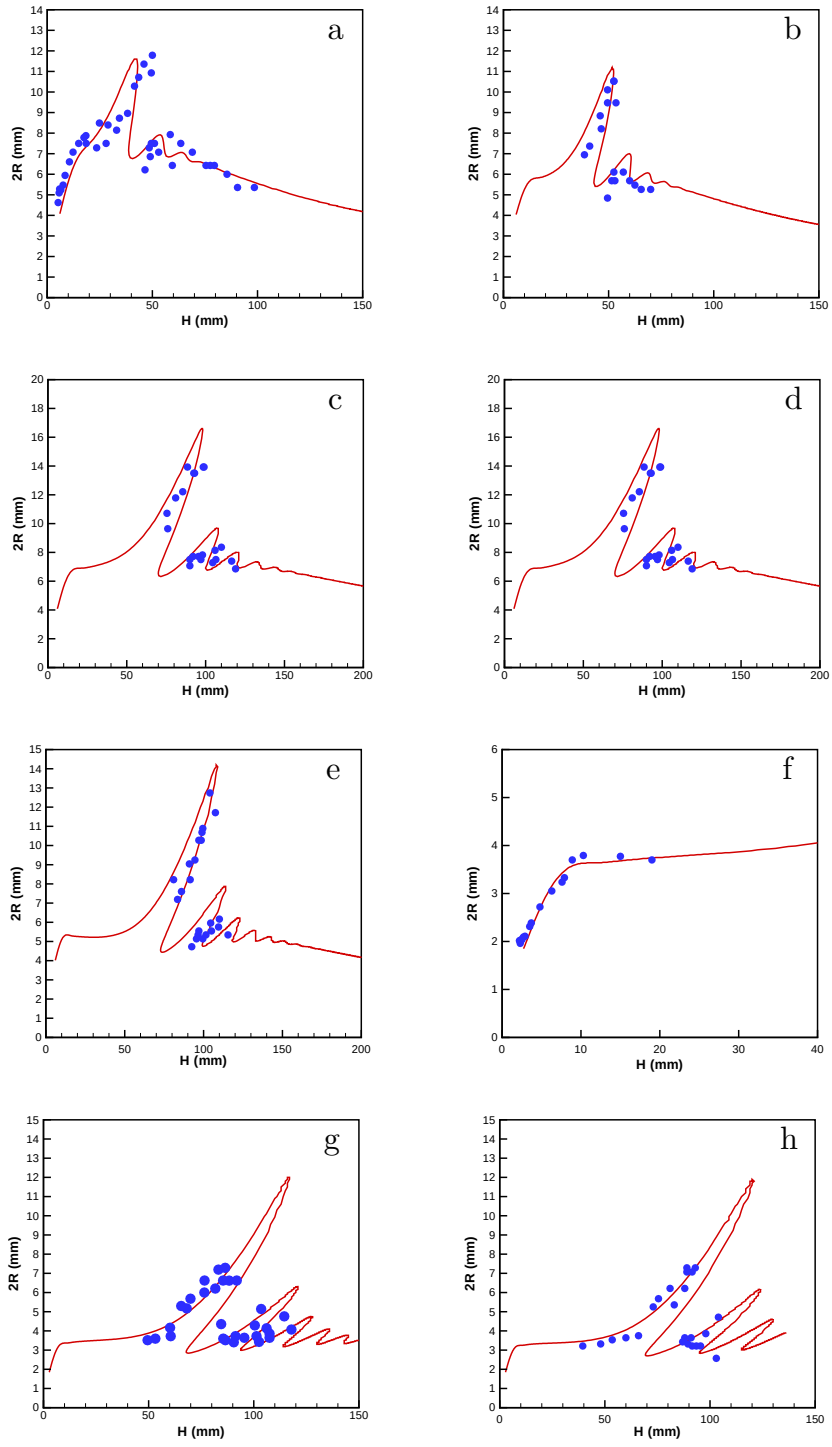

Figure 2.9: Coil diameter $2R$ as a function of height for eight experiments with different values of (Π_1, Π_2). a: (297, 2.8), b: (465, 2.35), c: (1200, 2.08), d: (1742, 2.99), e: (3695, 2.19), f: (7143, 3.67), g: (9011, 3.33), h: (10052, 3.18). The circles and the solid line show the experimental measurements and the predictions of the slender-rope numerical model, respectively. Surface tension effect was included in numerical calculations for these experiments.

2.6.2 Diameter of the rope

The structure of the curves $a_1(H)$ (Fig. 2.10) is much simpler, showing in most cases a monotonic decrease as a function of height that reflects the increasing importance of gravitational stretching of the falling rope. The only significant departures from the simple structure are the rapid decrease of a_1 as a function of H in the viscous regime (leftmost portions of panels f and g) and a small degree of multivaluedness in the inertio-gravitational regime. The agreement between the measured values and the numerics is good, although the latter tend to be somewhat lower than the former on average.

The decrease of a_1 is due to gravitational stretching of the tail with negligible vertical inertia, even in the "inertial" regime $1.2 \leq H(g/\nu^2)^{1/3} \leq 2$. Again, the apparent paradox is resolved by noting that inertia, like gravity, can be simultaneously dominant in the coil and negligible in the tail. Vertical inertia eventually becomes important in the tail as well when $H(g/\nu^2)^{1/3}$ exceeds a value ≈ 3.

2.7 Secondary Buckling

In the high-frequency inertial regime, the rapidly coiling rope can pile up to a great height, forming a hollow fluid column whose length greatly exceeds the rope diameter. When the height of the column exceeds a critical value H_c, it collapses under its own weight (Fig. 2.11), and the process then repeats itself with a well-defined period that greatly exceeds the coiling period. We call this phenomenon 'secondary buckling', as opposed to the 'primary' buckling that is responsible for coiling in the first place.

As a first step towards a physical understanding of secondary buckling, we apply dimensional analysis to measurements of the critical height from 13 different laboratory experiments with fixed kinematic viscosity ν, the surface tension coefficient γ, diameter of orifice d, the flow rate Q and different height from orifice to pile of fluid. The critical buckling height H_c can depend on the fluid density ρ, the kinematic viscosity ν, the surface tension coefficient γ, the coil radius R, the rope diameter $d_1 \equiv 2a_1$, and the flow rate Q, or (equivalently) the effective velocity $U_0 \equiv Q/2\pi d_1 R$

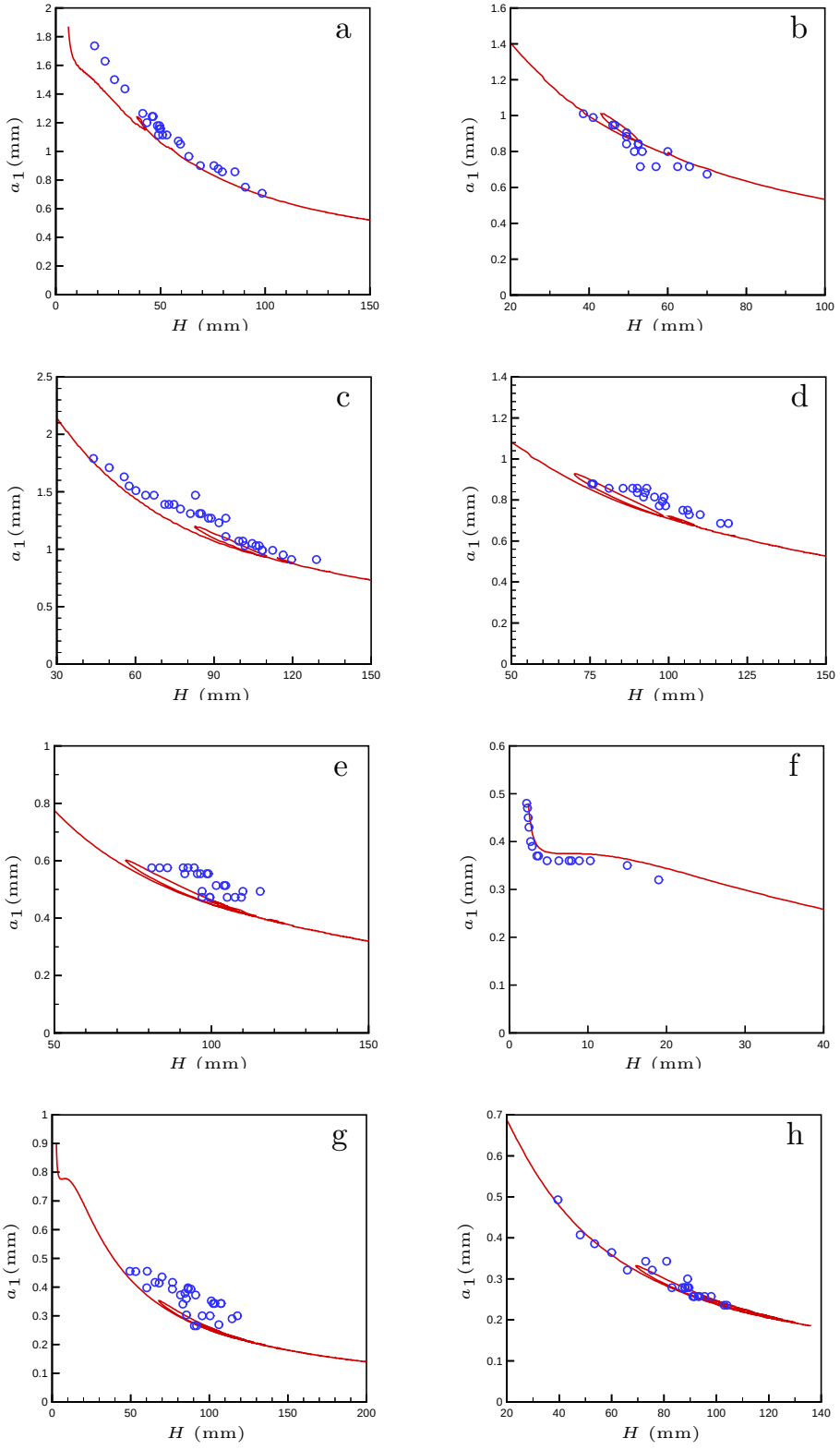

Figure 2.10: Rope radius a_1 within the coil as a function of height, for the same experiments as in Fig. 2.9.

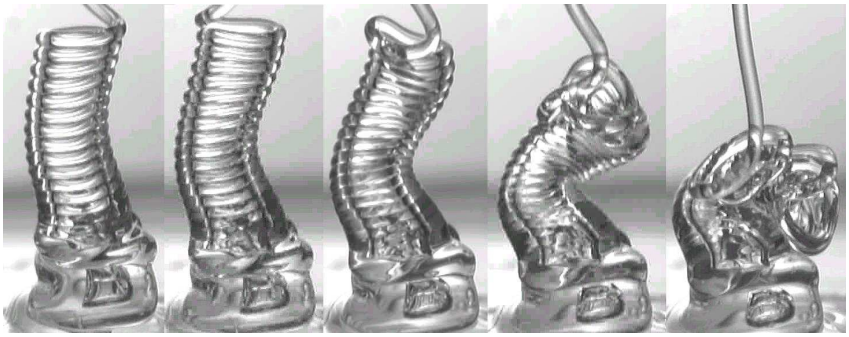

Figure 2.11: Secondary buckling of the coil in the inertial regime, in an experiment performed using the high-frequency setup, with $\nu = 125$ cm^2/s, $d = 0.15$ cm, $Q = 0.072$ cm^3/s, and $H = 14$ cm. Time between two photographs is nearly 0.1 s.

at which fluid is added to the top of the column. From these seven parameters four dimensionless groups can be formed, which we take to be

$$G_0 = \frac{H_c}{d_1}, \quad G_1 = \frac{\nu U_0}{g d_1^2}, \quad G_2 = \frac{\gamma}{\rho g d_1^2}, \quad G_3 = \frac{R}{d_1}. \tag{2.13}$$

The groups G_0, G_1 and G_2 are identical to those used by Tchavdarov et al [4, 33] in their study of the onset of buckling in plane liquid sheets. Now we can write

$$\frac{H_c}{d_1} = f(G_1, G_2, G_3), \tag{2.14}$$

where the functional dependence remains to be determined.

Fig. 2.12 shows the measured values of H_c/d_1 for our thirteen experiments as functions of G_1 (a), G_2 (b), and G_3 (c). For comparison, Fig. 2.12a also shows the critical buckling height for plane liquid sheets [4], which is independent of the surface tension for $G_1 > 20$ when $G_2 \leq 0.9$ (the largest value of G_2 considered by Yarin and Tchavdarov [33]).

Fig. 2.12 shows that the buckling height increases with increasing the dimensionless flow rate G_1. The trend of the data is roughly consistent with the slope $d(\ln H_c)/d(\ln G_1) \approx 0.2$ for a planar film (solid line in Fig. 2.12a). The observed

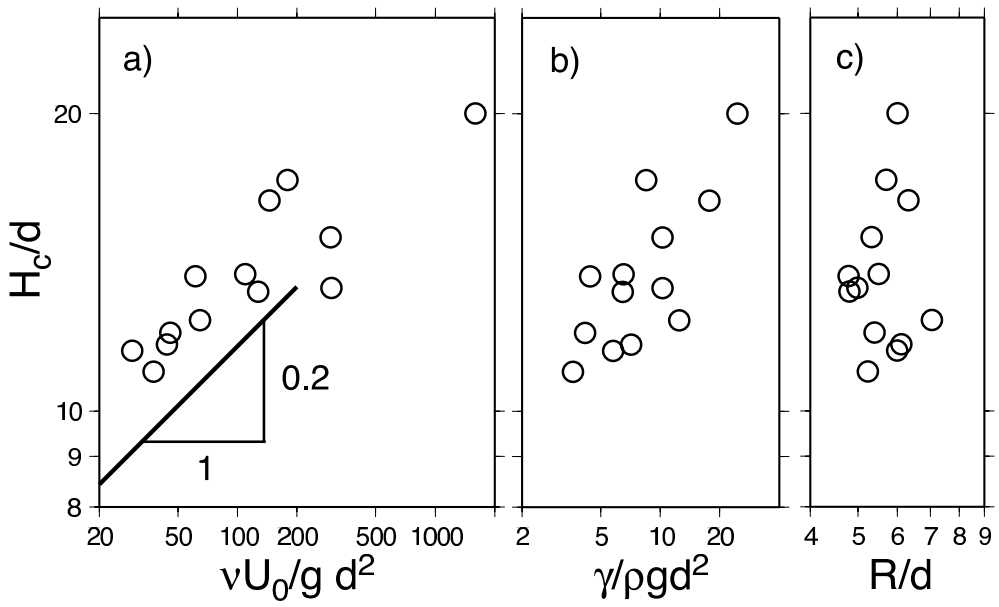

Figure 2.12: Critical height H_c for secondary buckling as a function of the dimensionless parameters G_1 (a), G_2 (b), and G_3 (c) defined by equation 2.13. The solid line in part (a) is the critical buckling height predicted by a linear stability analysis for a planar film.

buckling heights also appear to increase with increasing G_2 (Fig. 2.12b). This dependence has no analog in the case of a planar film, for which the predicted value of H_c at high flow rates is independent of the surface tension [33]. However, we note that the total range of variation of the parameter R/d_1 is less than a factor of 2 in our experiments, (Fig. 2.12c), so it is difficult to infer whether the buckling height depends on R/d_1 or not.

2.8 Conclusion

In this chapter we presented experimental investigation of the coiling of a liquid rope on a solid surface and compare these results with predictions of a numerical model for this problem. We explained three different regimes of coiling (viscous, gravitational and inertial) and presented the experimental measurements of frequency vs. height in each regime. We showed that in transition from gravitational to inertial coiling, the frequency was multivalued and could jump between two frequencies during the time. We also presented measurements of the radii of the coil and the rope, which were in agreement with the numerical predictions. Finally, we studied the secondary buckling, which is the buckling of the column of the coils in high frequencies, and used dimensional analysis to reveal a systematic variation of the critical column height as a function of the parameters of the problem.

Chapter 3

Multivalued inertio-gravitational regime

3.1 Introduction

The experimental observations of chapter 2 show an oscillation between two frequencies at a fixed fall height near the gravitational to inertial transition. Ribe (2004) predicted that multivalued curves of frequency vs. height should be observed when coiling occurs in the gravitational-to-inertial transitional regime corresponding to intermediate fall heights.

According to Fig.2.3 for $0.4 \leq H(g/\nu^2)^{1/3} \leq 1.2$, the viscous forces in the coil are balanced by both gravity and inertia, giving rise to a complex transitional regime. The curve of frequency vs. height is now multivalued, comprising a series of roughly horizontal "steps" connected by "switchbacks" with strong negative slopes. For the example of Fig. 2.3, up to five frequencies are possible at a given height. Near the turning points, the frequency obeys a new "inertio-gravitational" (IG) scaling.

In this chapter we seek systematically characterize the multivalued regime of liquid rope coiling using a combination of laboratory experiments and compare with the results of Ribe.

3.2 Experimental Methods

We have used the first setup (Fig.2.2 a) and the working fluids were different silicone oils ($\rho = 0.97$ g cm^{-3}, $\nu = 125$, 300, 1000 or 5000 cm^2 s^{-1}, $\gamma = 21.5$ dyne cm^{-1}). The flow rate Q was determined to within $\pm 4.5\%$ by recording the volume of fluid in the syringe as a function of time. This technique permitted access to portions of the (Π_1, Π_2) plane that are hard to reach with free (gravity-driven) injection. The coiling frequency was determined by counting frames of movies taken with a CCD camera (25 frames s^{-1}), this method allows us to measure the frequency for the experiments that oscillate between different states. For each point (Π_1, Π_2) investigated, separate sets of measurements were obtained by increasing and decreasing the height over the range of interest, and in one case additional measurements were made at randomly chosen heights. The raw fall heights were corrected by subtracting the height of the pile of fluid on the plate beneath the coil. This ensures proper comparability with the numerical solutions, in which no pile forms because the fluid laid down on the plate is instantaneously removed. To avoid unintentional bias, the experiments were performed and the fall heights corrected before the corresponding curve of frequency vs. height was calculated numerically. The effect of surface tension was included in all numerical calculations.

A disadvantage of forced injection is that unwanted "die-swell" [37] occurs in some cases as the fluid exits the orifice. The radius of the tail then varies along the rope in a way significantly different than that predicted by our numerical model. Die-swell was negligible in all the experiments with $\nu = 1000$ cm^2 s^{-1}, but significant ($\approx 10 - 15\%$ increase in radius) in some experiments performed with lower viscosities. Here we report only experiments for which die-swell did not exceed 10%.

For fall heights within a certain range, we observed two, three or even four different steady coiling states with different frequencies, each of which persisted for a time before changing spontaneously into one of the others (Fig. 3.3).

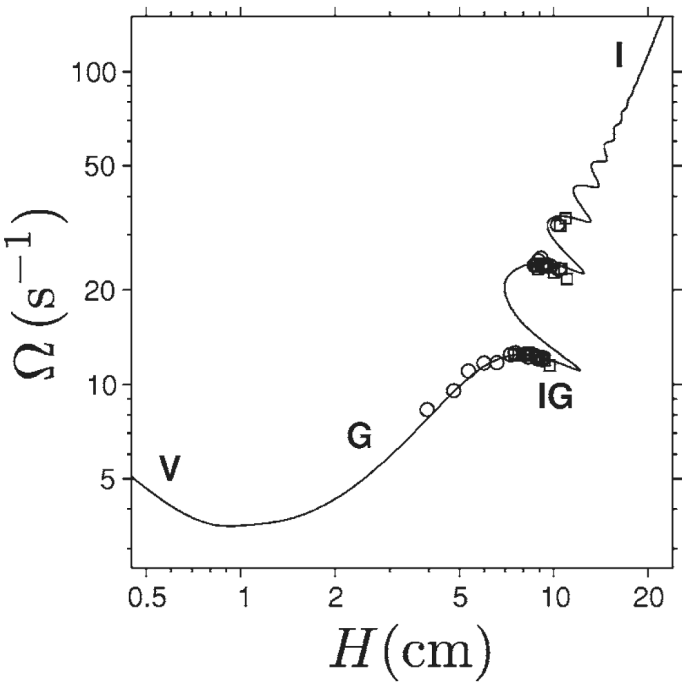

Figure 3.1: Regimes of liquid rope coiling. The symbols show experimental observations of the coiling frequency Ω as a function of the fall height H for an experiment performed using viscous silicone oil ($\rho = 0.97$ g cm^{-3}, $\nu = 1000$ cm^2 s^{-1}, $\gamma = 21.5$ dyne cm^{-1}) with $d = 0.068$ cm and $Q = 0.00215$ cm^3 s^{-1} [34]. The solid line is the numerically predicted curve of frequency vs. height for the same parameters. Portions of the curve representing the different coiling regimes are labeled: viscous (V), gravitational (G), inertio-gravitational (IG), and inertial (I).

3.3 Inertio-Gravitational Coiling

According to Fig. 2.3 and Fig. 3.1 between the gravitational and inertial parts of the curve of frequency vs. height there is a region in which the frequency is multivalued, comprising a series of roughly horizontal "steps" connected by "switchbacks" with strong negative slopes. The curve exhibits four turning points (labelled $i - iv$ in Fig. 2.3) where it folds back on itself. The additional "wiggles" at larger values of $H(g/\nu^2)^{1/3}$ are not turning points because the slope of the curve always remains positive. For the example of Fig. 2.3, up to five frequencies are possible at a given height, three of them on the roughly horizontal steps and two others on the switchback lines.

Near the turning points, the frequency obeys a new "inertio-gravitational" (IG) scaling: unlike the first three regimes, the frequency of IG coiling is determined by the balance of forces acting on the long tail portion of the rope above the coil, which behaves like a whirling viscous string that deforms primarily by stretching, gravity, centrifugal inertia, and the viscous forces that resist stretching are all important here, and coiling at a fixed height can occur with different frequencies [34].

3.3.1 Experimental Observations

In the laboratory, coiling in the inertio-gravitational regime is inherently time dependent, taking the form of aperiodic oscillation between two quasi-steady states with different frequencies for a given fall height. Such an oscillation occurs, e.g., at $H \approx 7$ cm in the experiment of Fig. 2.6(b). The typical appearances of the two quasi-steady states are shown in Fig. 3.2. Note first that the coil radius $R = U_1/\Omega$ is always smaller for the state with the higher frequency, because the axial velocity U_1 of the rope being laid down (which depends only on the fall height) is nearly the same for both states. Moreover, the pile of fluid beneath the coil is taller at the higher frequency, because rope laid down more rapidly can mount higher before gravitational settling stops its ascent. This is because the pile height is controlled by a steady-state balance between addition of fluid (the coiling rope) at the top, and removal of fluid at the bottom by gravity-driven coalescence of the pile into the pool of fluid spreading on the plate. The coalescence rate increases linearly with the pile height, and the rate at which fluid addition builds up the pile ($\equiv Q/4\pi R a_1$) is larger for the high-frequency state. The height of the pile must therefore also be larger for this state.

The origin of the time-dependence of inertio-gravitational coiling is revealed by the curves of $\Omega(H)$ for steady coiling. The coexistence of two or more states at the same fall height reflects the multivalued character of the curve of frequency vs height, which is illustrated in more detail in Fig. 3.1. The symbols show coiling frequencies measured in an experiment performed using viscous silicone oil ($\rho = 0.97$ g cm^{-3}, $\nu = 1000$ cm^2 s^{-1}, $\gamma = 21.5$ dyne cm^{-1}) with $d = 0.068$ cm and $Q = 0.00215$ cm^3 s^{-1} [34], and the solid line shows the curve of frequency vs height predicted numerically

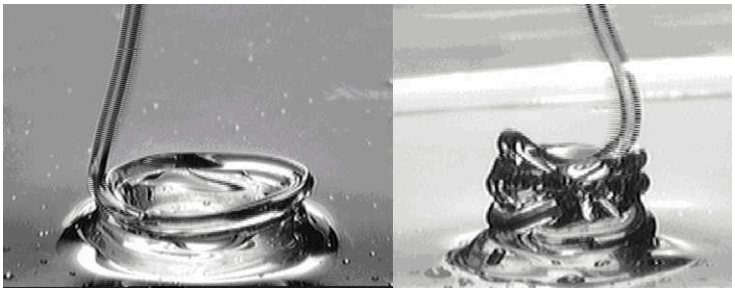

Figure 3.2: Coexisting coiling states in an experiment with $\nu = 300$ cm^2/s, $Q = 0.041$ cm^3/s, $d = 1.5$ mm and $H = 4.5$ cm. (a) low-frequency state; (b) high-frequency state.

for the same parameters by Ribe [19]. The numerically predicted frequencies of these steady states are in fact identical to the frequencies of the two quasi-steady states observed in the laboratory.

3.3.2 Time dependence of IG coiling and transition between states

Here we investigate the time-dependence of inertio-gravitational coiling in more detail, focusing on the multiplicity of the coexisting states and the fine structure of the transitions between them. We begin by noting that the multivaluedness of a given curve $\Omega(H)$ can be conveniently characterized by the number N of turning (fold) points it contains. Here we define turning points as points where $d\Omega/dH = \infty$ and $d^2\Omega/dH^2 > 0$; thus $N = 2$ for the solid curve in Fig. 2.6(b). Ribe showed [34] that N is controlled primarily by the value of the dimensionless parameter Π_1 scaling as $N \sim \Pi_1^{5/32}$ in the limit $\Pi_1 \to \infty$. The experiment of Fig. 2.6(b) has $\Pi_1 = 313$, which is not large enough for the multivalued character of $\Omega(H)$ to appear with full clarity. Accordingly, we used our low-frequency setup (Fig. 2.2(a)) to perform an experiment with $\nu = 1000$ cm^2/s and a very low flow rate $Q = 0.00258$ cm^3/s, corresponding to $\Pi_1 = 8490$. The numerically predicted $\Omega(H)$ (Fig. 3.3 solid line) now has $N = 6$, with up to 7 distinct steady states possible at a fixed fall height

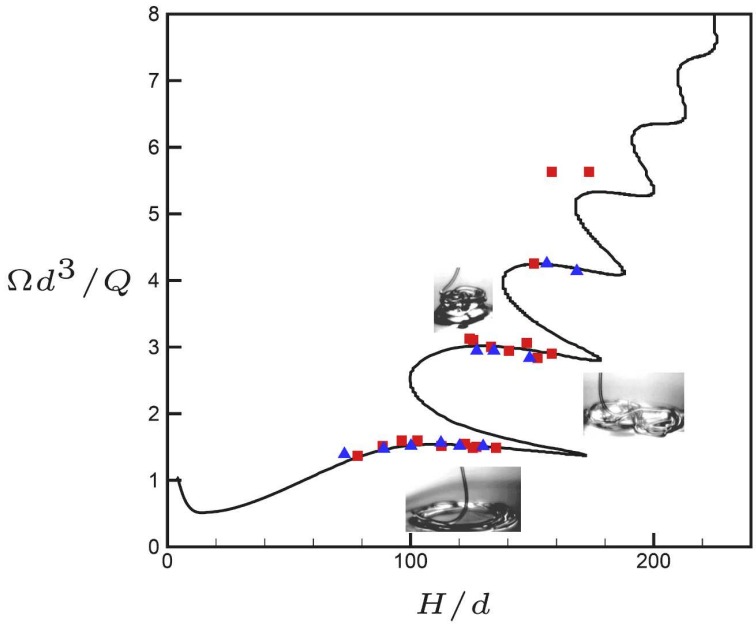

Figure 3.3: Rescaled coiling frequency as a function of the rescaled fall height, for an experiment performed using the low-frequency setup with $\nu = 1000$ cm^2/s, $d = 0.068$ cm, and $Q = 0.00258$ cm^3/s. Symbols: experimental measurements obtained with the fall height increasing (squares) and decreasing (triangles). Solid line: prediction of the slender-rope numerical model. Figures show geometry of coexisting coiling states in an experiment performed with $\nu = 1000$ cm^2 s^{-1}, $d = 0.068$ cm, $Q = 0.0042$ cm^3 s^{-1} ($\Pi_1 = 6725$, $\Pi_2 = 3.76$). The total (uncorrected) fall height is 7.1 cm, and the radius of the portion of the rope shown is 0.028 cm. left, bottom: low-frequency state; left, top: high-frequency state; right: transitional "figure of eight" state.

($H/d \approx 170$, where $d \equiv 2a_0$). The experimental measurements (solid symbols in Fig. 3.3) group themselves along four distinct branches or 'steps' that agree remarkably well with the numerical predictions, except for a small offset at the highest step. To our knowledge this is the first experimental observation of four distinct steps in inerto-gravitational coiling [32]. We did not observe any coiling states along the backward-sloping portions of the $\Omega(H)$ connecting the steps, these states seems to be unstable to small perturbations [35]. We will investigate it more accurately by comparing the experimental results with a linear stability analysis for these parts of the curves, in the next sections.

The experiments also provide some insight into the mechanism of the transition

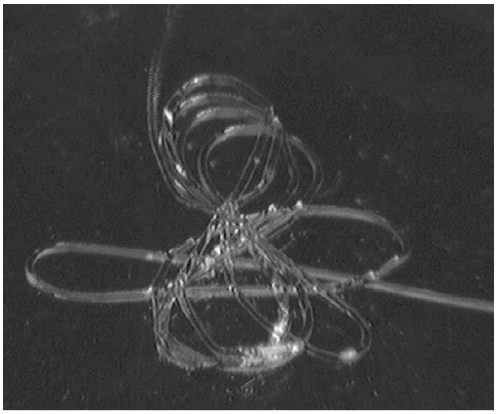

Figure 3.4: Intermediate 'figure of eight' state for an experiment with $\nu = 5000$ cm^2/s, $Q = 0.00145$ cm^3/s, $d = 0.068$ cm , and $H = 16.5$ cm.

between coexisting coiling states. These occur spontaneously, and appear to be initiated by small irregularities in the pile of fluid already laid down beneath the coiling rope. In most (but not all) cases, the transition occurs via an intermediate 'figure of eight' state, an example of which is shown in Fig. 3.4. During a low to high frequency transition, the initially circular coil first changes to a 'figure of eight' whose largest dimension is nearly the same as the diameter of the starting coil. The new, high-frequency coil then forms over one of the loops of the 'figure of eight' . If the new coil forms over the loop of the 'eight' that was laid down first, the sense of rotation (clockwise or counterclockwise) of the new coil is the same as that of the old. If however the new coil forms over the second loop, the sense of rotation changes.

Further understanding of the transition can be gained by measuring the coiling frequency and the sense of rotation as a function of time (Fig. 3.5). The experimental measurements (circles) show a clear oscillation between two states whose frequencies agree closely with the numerically predicted frequencies of steady coiling at the fall height in question (horizontal portions of the solid line). The oscillation is irregular, with no evident characteristic period, in agreement with the hypothesis that transitions are initiated by irregularities in the fluid pile. The only clear trend we were able to observe was that the low-frequency state tends to be preferred when the coiling occurs close to the gravitational regime (i. e., for lower heights), while the

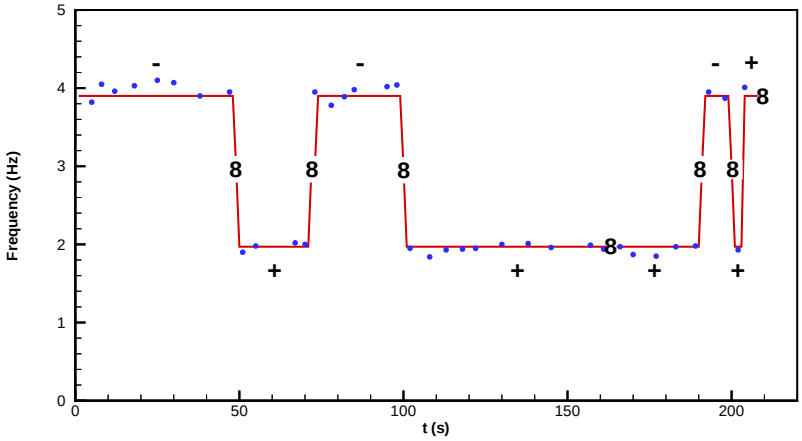

Figure 3.5: Coiling frequency as a function of time for the experiment of Fig. 3.3 and $H = 8.55$ cm. The experimental measurements are shown by circles, and the numerically predicted frequencies for the fall height in question are represented by the horizontal portions of the solid line. The symbol '8' indicates the appearance of an intermediate 'figure of eight' state, as described in the text. The '+' and '-' signs indicate counter-clockwise and clockwise rotation, respectively. The oscillation shown is between the two lowest 'steps' in Fig. 3.3.

high-frequency state is preferred near the inertial regime (greater heights). The sense of rotation (indicated by the symbols '+' or '-' in Fig. 3.5) usually changes during the transition, but not always. All the transitions in Fig. 3.5 occur via an intermediate 'figure of eight' state (indicated by the symbol '8'), but in other experiments we have observed the 'figure of eight' without any transition, as well as transitions that occur without any 'figure of eight'.

3.4 Whirling Liquid String Model

In pure gravitational coiling with negligible inertia the rope is nearly vertical except in a thin boundary layer near the contact point (near the pile) where viscous forces associated with bending are significant. As H increases, however, the displacement of the rope becomes significant along its whole length, even though bending is still confined to a thin boundary layer near the contact point. But at the end of gravitational regime and close to the turning point in the frequency vs. height curves, it

appears that the dynamics of this regime is controlled by the tail of the rope, and that the bending boundary layer plays a merely passive role.

We now demonstrate that the dynamics of the tail provide the key to explaining the multivaluedness of the frequency-height curve. Numerical simulations show that the rates of viscous dissipation associated with bending and twisting in the tail are negligible compared to the dissipation rate associated with stretching. The tail can therefore be regarded as a "liquid string" with negligible resistance to bending and twisting, whose motion is governed by a balance among gravity, the centrifugal force, and the axial tension associated with stretching. The balance of gravity and the centrifugal force normal to the tail requires

$$\rho g A \sin\theta \sim \rho A \Omega^2 y, \tag{3.1}$$

where A is the area of the cross-section of the tail, θ is its inclination from the vertical, and y is the lateral displacement of its axis. Because $y \sim R$ and $\sin\theta \sim R/H$, (3.1) implies that Ω is proportional to the scale

$$\Omega_{IG} = \left(\frac{g}{H}\right)^{1/2}, \tag{3.2}$$

which is just the angular frequency of a simple pendulum.

Ribe has shown that [34] the lateral displacement y (according to Fig. 3.6) of the axis of the string satisfies the boundary value problem:

$$k^{-1}\sin k(1-\tilde{s})y'' - y' + \tilde{\Omega}^2 y = 0, \qquad y(0) = 0, \quad y(1) \text{ finite}, \tag{3.3}$$

where primes denote differentiation with respect to the dimensionless arclength $\tilde{s} = s/H$ and $\tilde{\Omega} = \Omega(H/g)^{1/2}$. The three terms in (3.3) represent the axis-normal components of the viscous, gravitational, and centrifugal forces, respectively, per unit length of the string. The dimensionless parameter k measures the degree of gravity-induced

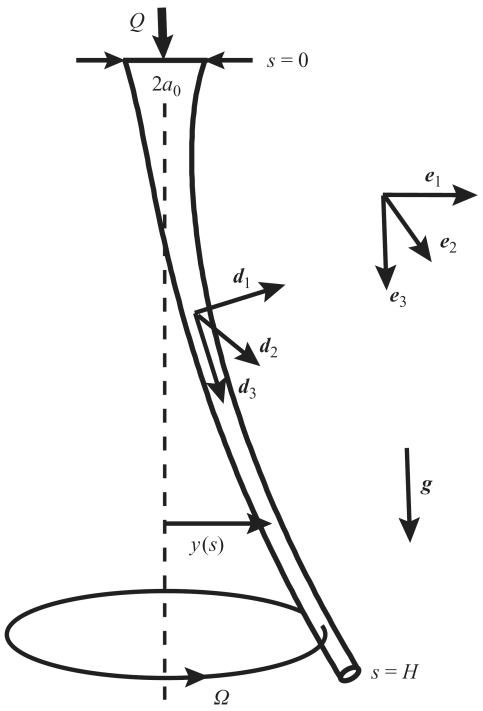

Figure 3.6: Geometry of liquid rope coiling in the inertio-gravitational regime. e_i $(i = 1, 2, 3)$ are Cartesian unit vectors fixed in a frame rotating with the rope, and d_i are orthogonal material unit vectors defined at each point on its axis, d_3 being the tangent vector. The parameters Q, a_0, H, R, and Ω are defined as in Fig. 2.1a. Geometry of the tail, modeled as an extensible string with negligible resistance to bending and twisting. This string lies in the plane normal to e_2, and $d_1 \cdot e_2 = 0$. The lateral displacement of the axis from the vertical is $y(s)$, where s is the arclength measured from the injection point.

stretching of the string, and satisfies the transcendental equation

$$0 = 2B \cos^2 \frac{k}{2} - 3k^2, \tag{3.4}$$

where B is the buoyancy number defined as $B \equiv \pi a_0^2 g H^2 / \nu Q$. The limit $k = 0$ $(B = 0)$ corresponds to an unstretched string with constant radius, whereas a strongly stretched string has $k = \pi$ $(B \to \infty)$.

Equations (3.3) define a boundary-eigenvalue problem which has non-trivial solutions only for particular values $\tilde{\Omega}_n(k)$ of the frequency $\tilde{\Omega}$. Fig. 3.7 shows the first

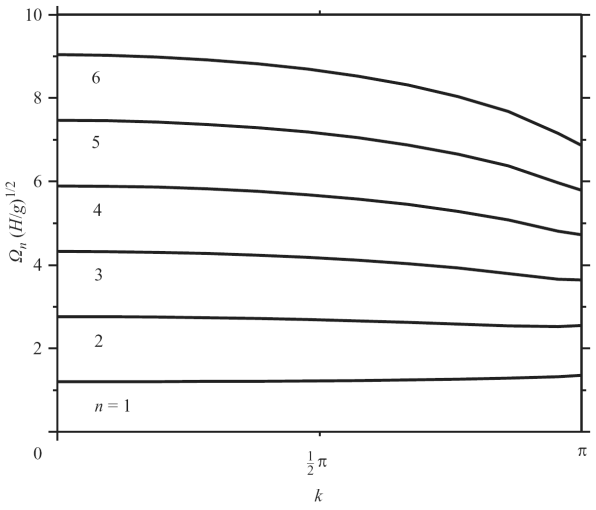

Figure 3.7: First six eigenfrequencies $\Omega_n(k)$ of the boundary-value problem (3.3) for a whirling liquid string.

six of these eigenfrequencies as functions of k, Ribe has solved using AUTO 97 [34]. In the limit $k = 0$ we recover the classical solution for the eigenfrequencies of an inextensible chain, which satisfy $J_0(2\tilde{\Omega}_n(0)) = 0$, where J_0 is the Bessel function of the first kind of order 0.

To test whether these eigenfrequencies correspond to the multiple frequencies seen in the full numerical solutions, Ribe rescale the numerically predicted curves of frequency vs. height to curves of Ω/Ω_{IG} vs. Ω_G/Ω_{IG}. On a log-log plot, these rescaled curves should exhibit distinct segments with slopes of unity and zero, corresponding to gravitational ($\Omega \propto \Omega_G$) and inertio-gravitational ($\Omega \propto \Omega_{IG}$) coiling, respectively. Fig. 3.8 shows Ω/Ω_{IG} vs. Ω_G/Ω_{IG} for $\Pi_1 = 10^3$, 10^5, and 10^6. As expected, the rescaled curves clearly display a transition from gravitational coiling on the left to inertio-gravitational coiling on the right. Moreover, the multiple frequencies in the rescaled curves correspond very closely to the whirling string eigenfrequencies $\Omega_n(\pi)$ in the "strong stretching" limit $k = \pi$, the first six of which are shown by the black bars at the right of Fig. 3.8. We conclude that a rope coiling in the inertio-gravitational mode

does indeed behave as a whirling liquid string with negligible resistance to bending and twisting.

3.5 Comparison with experiment

We now compare the predictions of the thin-rope numerical model with laboratory data. Fig. 3.9 shows the coiling frequency Ω measured as a function of height H for the five points (Π_1, Π_2) together with curves of $\Omega(H)$ predicted numerically for the same parameters. The observations and the numerical predictions agree extraordinarily well for experiments (b)-(e), which were all performed with $\nu = 1000$ cm^2 s^{-1}. The somewhat poorer agreement for case (a) ($\nu = 300$ cm^2 s^{-1}) is probably due to die-swell, which was about 10% in this experiment. The measurements are concentrated along the roughly horizontal steps of the numerically predicted curves, leaving the "switchback" portions in between almost entirely empty. In all experiments, two coexisting coiling states with different frequencies exist over a small but finite range of fall heights; in experiment (b), we observed three such states at $H \approx 10.8$ cm. In experiments (a)-(d), the states observed along the first step in the curve extend right up to the first turning point. In experiment (e), by contrast, the coiling "jumps" to the second step before the first turning point is reached.

3.6 Resonant Oscillation of the Tail in Mutivalued Regime

The multiple 'spikes' in the scaled curves of frequency vs. height in Fig. 3.8 strongly suggest that IG coiling may reflect a resonance phenomenon. Recall that the frequency of gravitational coiling is controlled by the dynamics in the 'coil' portion of the rope. Therefore if the frequency set by the coil happens to be close to an eigenfrequency of the tail, the coil will excite a resonant oscillation of the tail. Accordingly, the spikes in Fig. 3.8 can be interpreted as resonant oscillations that occur when

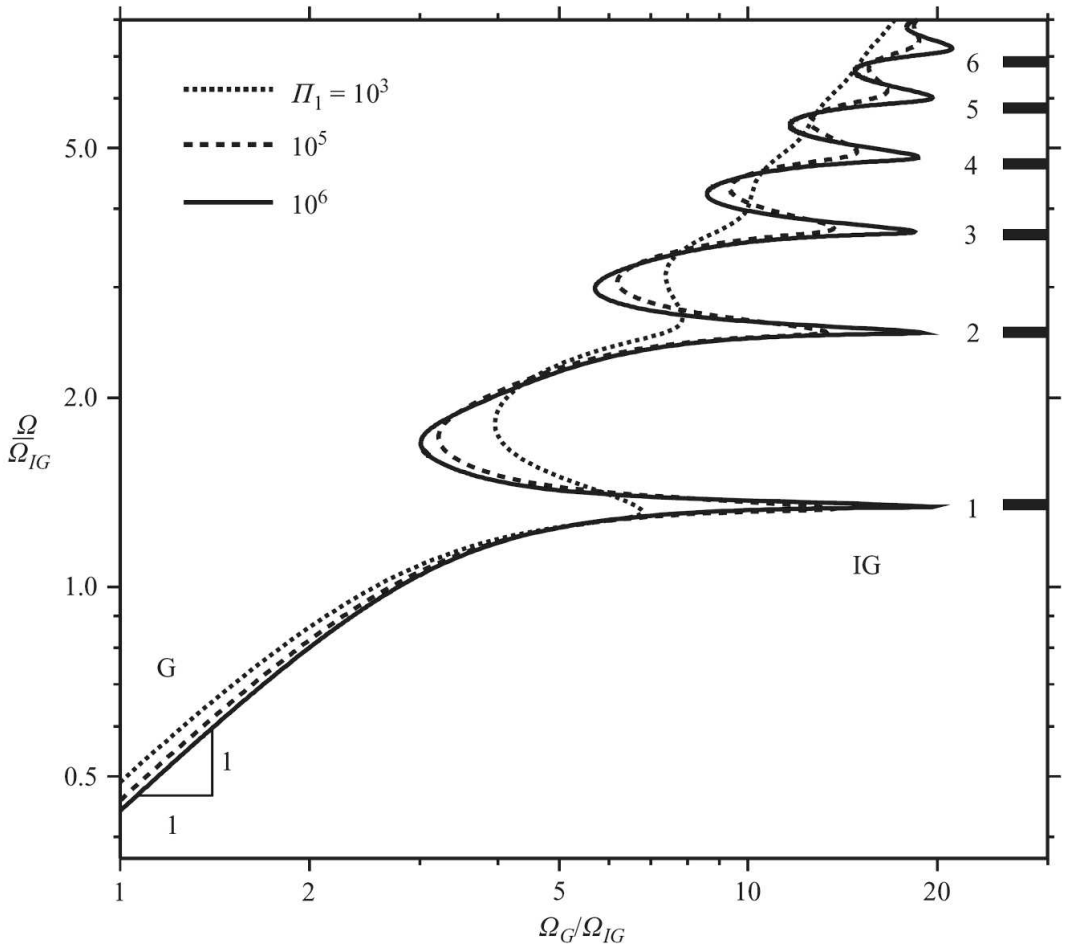

Figure 3.8: Ω/Ω_{IG} vs. Ω_G/Ω_{IG} in the limit of strong stretching ($a_1/a_0 \ll 1$) for $(\Pi_1, \Pi_2) = (10^3, 0.316)$ (dotted line), $(10^5, 0.316)$ (dashed line), and $(10^6, 0.562)$ (solid line.) Segments of the curves representing gravitational and inertio-gravitational coiling are denoted by G and IG, respectively. The horizontal black bars (right) indicate the first six eigenfrequencies of a strongly stretched ($k = \pi$) whirling liquid string (Fig. 3.7).

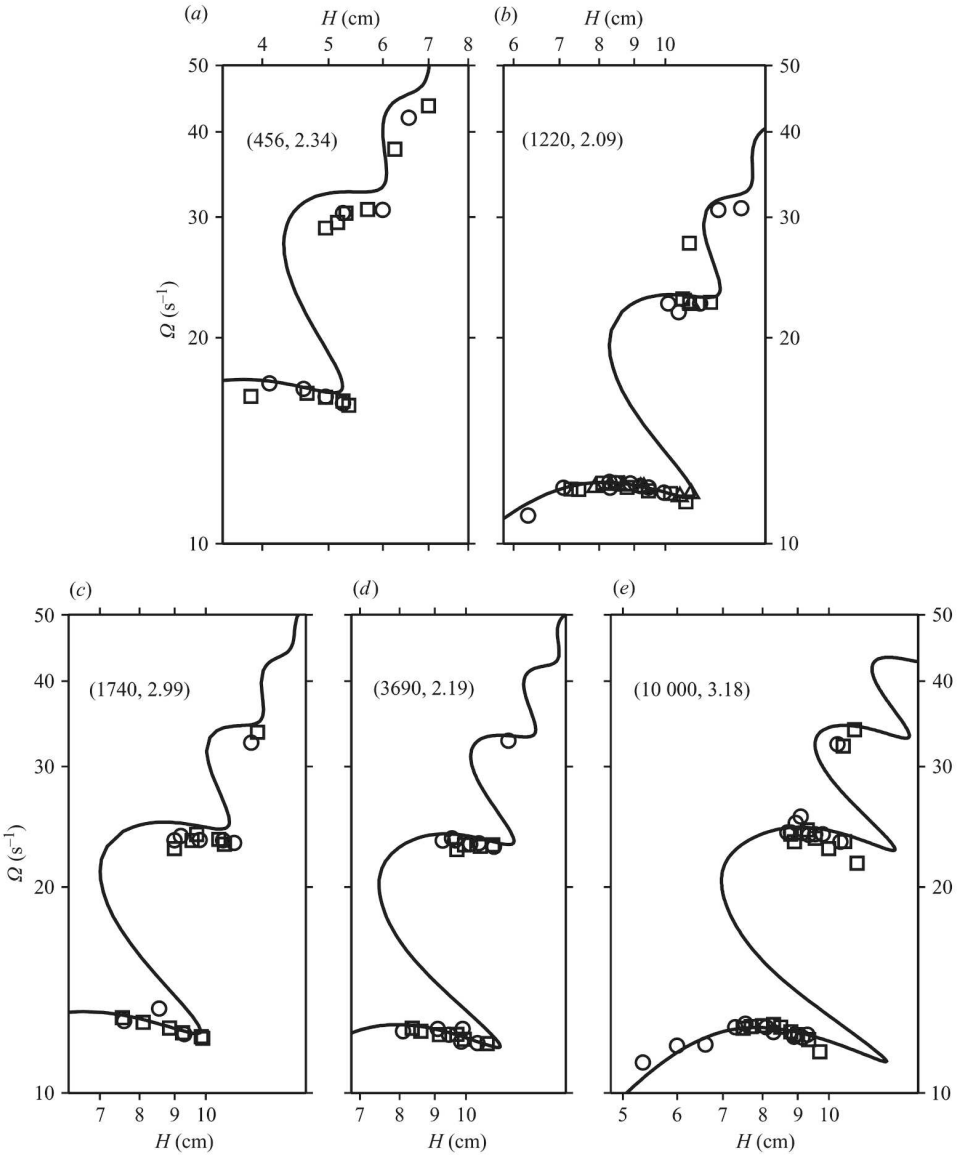

Figure 3.9: Comparison of experimentally measured (symbols) and numerically predicted (solid lines) frequencies as functions of height for the experiments. The fluid viscosity was $\nu = 300$ cm^2 s^{-1} for experiment (a) and 1000 cm^2 s^{-1} for experiments (b)-(e). Values of (Π_1, Π_2) for each experiment are indicated in parentheses. Measurements were obtained in series with H increasing (squares), decreasing (circles), and varied randomly (triangles.) Error bars on H are smaller than the size of the symbols. Error bars on Ω, which in most cases do not exceed $\pm 5\%$, have been omitted for clarity.

$0.5\Omega_G \approx \Omega_n$, where $0.5\Omega_G$ is the frequency of gravitational coiling and Ω_n is one of the whirling string eigenfrequencies shown in Fig. 3.7.

An important problem remaining to be solved is that of the stability of our numerical solutions. The experiments (Fig. 3.9) show that observable states of steady coiling in the multivalued regime are concentrated along the nearly horizontal steps in the curve of frequency vs. height below turning points. None of the steady states we observed lies on the steeply sloping switchback between the first two steps, and only in two cases (Fig. 3.9a and b) did we observe states that may lie on the second (less steeply sloping) switchback. This suggests that states along the first switchback (at least) may be unstable to small perturbations.

3.7 Stability of Liquid Rope Coiling

As shown in Fig. 3.9, the observed frequencies in 'inertio-gravitational' regime are concentrated along the roughly horizontal 'steps' of the $\Omega(H)$ curve, leaving the steeper portions with negative slope ('switchbacks') empty. The absence of observed steady coiling states along the switchbacks suggests that such states may be unstable to small perturbations. Here we investigate this question by compering experiments with results of a linear stability analysis that have been done by Ribe *et al.* [35].

Here we present the results of stability analysis for three of the laboratory experiments have been shown in Fig. 3.9, [34], in each of which the coiling frequency Ω is measured as the fall height H is varied for fixed values of the hole diameter d, the flow rate Q, and the fluid properties ρ, ν, and γ. Each experiment is therefore defined by particular values of the dimensionless groups Π_1, Π_2, Π_3. The effect of surface tension was included in numerical calculations so we need the non dimensional parameter for the surface tension (Π_3). To carry out the stability analysis for a given experiment, Ribe *et al.* first calculated numerically the dimensionless frequency $\Omega(\nu/g^2)^{1/3} \equiv \tilde{\Omega}$ of steady coiling as a function of the dimensionless height $H(g/\nu^2)^{1/3} \equiv \tilde{H}$. This yields a curve similar to that shown (in dimensional form) in Fig. 3.9. Next, he chose a trial value of $\tilde{H}$, and use the 'pull/push' procedure described in appendix, to search

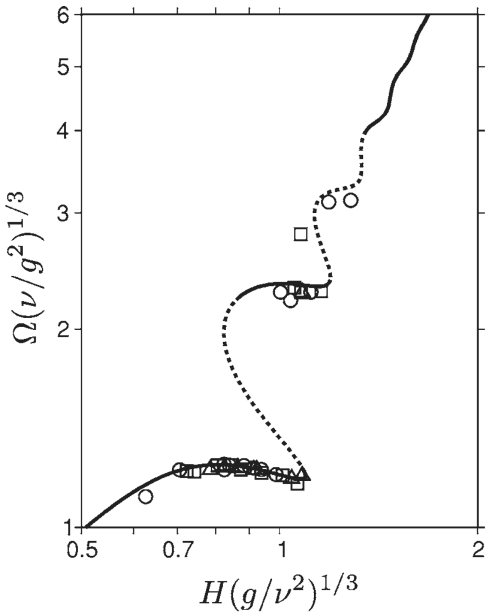

Figure 3.10: Stability of steady coiling with $\Pi_1 = 1220$, $\Pi_2 = 2.09$, and $\Pi_3 = 0.019$. The continuous curve shows the numerically calculated frequency of steady coiling as a function of height. The solid and dashed portions of the curve indicate stable and unstable steady states, respectively, as predicted using the numerical stability analysis described in the text. Symbols indicate experimental measurements [34] obtained in series with H increasing (squares), decreasing (circles), and varied randomly (triangles.)

for unstable modes having $\Re(\sigma) > 0$, which σ is growth rate. Then he continued any such modes in both directions along the curve $\tilde{\Omega}(\tilde{H})$, monitoring σ to identify the fall heights at which $\Re(\sigma)$ becomes zero, i.e. at which the mode in question becomes stable. By repeating this procedure for different trial values of $\tilde{H}$ along the curve $\tilde{\Omega}(\tilde{H})$, he determined the portions of the curve that represent unstable steady states.

The results of this procedure are shown in Figs. 3.10 - 3.12 for the parameters (Π_1, Π_2, Π_3) corresponding to the three laboratory experiments referred to above. In each figure, the symbols indicate experimental measurements obtained in series with H increasing (squares), decreasing (circles), and varied randomly (triangles.) The continuous curve in each figure shows the numerically calculated curve $\hat{\Omega}(\hat{H})$ for steady coiling, and its solid and dashed portions indicate stable and unstable steady states, respectively. Overall, the agreement between the numerical calculations and

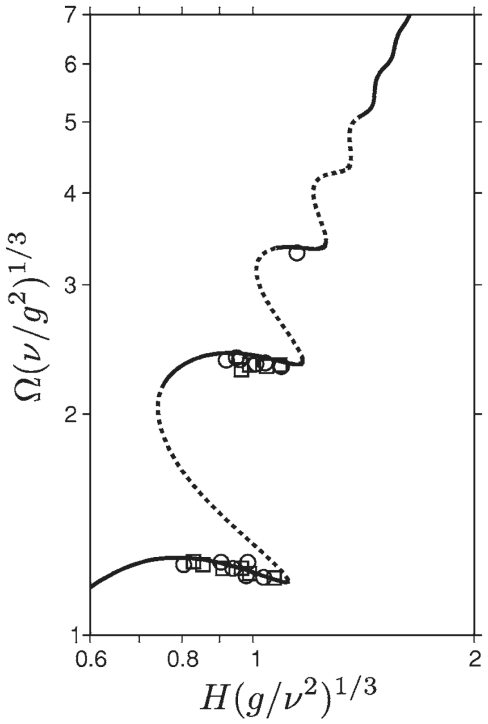

Figure 3.11: Same as Fig. 3.10, but for $\Pi_1 = 3690$, $\Pi_2 = 2.19$, and $\Pi_3 = 0.044$.

the experiments is very close: the observed steady states are concentrated along the stable portions of the calculated curves, leaving the unstable portions almost entirely 'unpopulated'. The only significant exceptions are the three measurements with the highest frequencies in Fig. 3.10, which lie close to an unstable segment of the calculated curve.

However, the growth rate of the instability along this portion of the curve is very small ($\sigma \approx 0.02\Omega$), implying that the coiling rope executes $\Omega/2\pi\sigma \approx 8$ revolutions during the time required for a perturbation to grow by a factor e. This may explain why apparently steady states such as those in Fig. 3.10 are observed despite their instability.

Using the Ribe *et al.*'s numerical results helps to explain the mechanism by which steady coiling becomes unstable. The steady coiling solution comprises an interior region in which bending is negligible and two boundary layers near the injection and contact points where significant bending is concentrated. In the interior, the rope

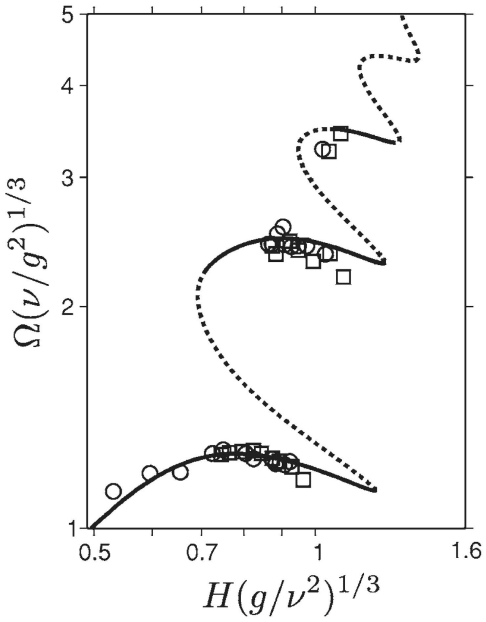

Figure 3.12: Same as Fig. 3.10, but for $\Pi_1 = 10050$, $\Pi_2 = 3.18$, and $\Pi_3 = 0.048$.

behaves essentially as a 'whirling viscous string' [34]: the lateral deflection increases smoothly downward and the gravitational force is balanced about equally by the viscous force associated with axial stretching and by (centrifugal) inertia. In the lower (and more dynamically significant) boundary layer, the gravitational force is balanced almost entirely by the viscous force associated with bending, with inertia playing a subsidiary role. The structural features of the eigenmode are concentrated in the lower boundary layer, where the gravitational force is balanced primarily by viscous forces. The mechanism of the instability therefore involves a balance between gravity and the viscous resistance of the rope to bending, with inertia playing a secondary role. This conclusion can be verified by 'turning off' all the inertial terms in the perturbation equations, while holding constant all the other parameters in the numerical code. The instability still occurs; but the growth rate is now more than double the 'true' growth rate predicted by the full numerical model with all inertial terms retained. This demonstrates that inertia is not essential to the instability, but that it nevertheless significantly influences the growth rate.

A comparison of Figs. 3.10-3.12 raises a further question: how does the number

N_s of stable segments of the curve $\Omega(H)$ depend on the experimental parameters? The stable segments are confined for the most part to the roughly horizontal portions ('steps') of the $\Omega(H)$ curve. Ribe *et al.* [34] showed that the total number N of (stable and unstable) steps in the curve scales as $N \sim \Pi_1^{5/32}$ in the limit when $\Pi_1 \to \infty$ and gravitational stretching of the rope is strong ($a_1 \ll a_0$). Figs. 3.10-3.12 suggest that N_s also increases with Π_1: $N_s = 2$ for $\Pi_1 = 1220$, and $N_s = 3$ for $\Pi_1 = 3690$ and 10050. Moreover, the fourth step in Fig. 3.12 is only slightly unstable ($\sigma \approx 0.004\Omega$), suggesting that $\Pi_1 = 10050$ may be just below the value above which $N_s = 4$. Unfortunately, numerical convergence becomes difficult to achieve when Π_1 and/or Ω is too large, and we were therefore not able to determine a scaling law for N_s. For now, we can only speculate that it scales in the same way as the total number of steps, viz., $N_s \sim \Pi_1^{5/32}$.

3.8 Conclusion

In this chapter we investigated experimentally and theoretically a curious feature of this instability: the existence of multiple states with different frequencies at a fixed value of the fall height. Using a numerical model based on asymptotic 'thin rope' theory, we determined curves of coiling frequency Ω vs. fall height H as functions of the fluid viscosity ν, the diameter d of the injection hole, the volumetric injection rate Q, and the gravitational acceleration g. In addition to the three coiling modes previously identified (viscous, gravitational, and inertial), we find a new multivalued "inertio-gravitational" mode that occurs at heights intermediate between gravitational and inertial coiling. The frequencies of the individual branches are proportional to $(g/H)^{1/2}$, and agree closely with the eigenfrequencies of a whirling liquid string with negligible resistance to bending and twisting. The predictions of the numerical model are in excellent agreement with laboratory experiments. The experiments further show that interbranch transitions in the inertio-gravitational regime occur via an intermediate state with a "figure of eight" geometry that usually changes the sense of rotation of the coiling but not always.

Comparing the experimental results with results of a linear stability analysis shows that steady coiling in the multivalued 'inertio-gravitational' (IG) regime is stable only along discrete segments of the frequency vs. height curve, the distribution of which agrees very well with high-resolution laboratory measurements. The stability analysis further shows that coiling is stable at all heights in the three remaining regimes (viscous, gravitational, and inertial), in agreement with the experiments in chapter 2 [31]. Analytical theory, numerical analysis, and laboratory experiments thus come together to offer a consistent portrait of steady coiling over the whole range of fall heights and frequencies at which the phenomenon occurs. The dominant balance of (perturbation) forces in the instability is between gravity and the viscous resistance to bending of the rope; inertia is not essential, although it significantly influences the growth rate.

Chapter 4

Spiral Bubble Pattern in Liquid Rope Coiling

4.1 Introduction

The study of spirals in nature goes back a few centuries, when for instance Swammerdam was one of the first to try and describe the beautiful forms of certain seashells [38]. The standard work on spontaneous pattern formation in Nature, Darcy Thompson's "On Growth and Form" [38] describes a multitude of spiral patterns; besides shells he discusses for instance spiral patterns of seeds in sunflowers, but also the helical structure of branches or leaves on a growing plant stem. All these spirals are self-organized, but still obey rather strict mathematical rules; shells are generally logarithmic spirals in which the distance between successive loops grows in a precisely determined fashion with increasing distance from the center [39]. For phyllotaxis (the sunflower spirals), Douady and Couder [40] have shown with a clever laboratory experiment that the spirals form due to a self-organized growth processes: new seeds are generated at a fixed frequency in the center and through a steric repulsion repel each other; the maximization of the distance between the seeds then leads to a special subtype of logarithmic spiral pattern: the golden or Fibonacci spiral.

However not all spirals in nature are due to a steric repulsion between the elements constituting it. Over the past few years, self-organized spiral waves have been studied extensively [41] . These dynamic spirals form spontaneously in excitable media [42, 43]

and have been observed in systems as different as catalytic surface oxidation [44], the Belousov-Zhabotinsky chemical reaction [45, 46, 47, 48, 49] , aggregating colonies of slime mold [50, 51] and heart tissue where spiral waves in the contracting heart tissue are believed to be one of the causes role in cardiac arrhythmia and fibrillation [52].

In this chapter we present a simple laboratory experiment that demonstrates the condition for the formation of spiral waves. In previous chapters we investigated how the frequency and radius of the coiling depends on the orifice diameter, the height of fall, flow rate, and the fluid viscosity. We showed that there are four different regimes of coiling that depend strongly on the height of fall. During the coiling some air can be captured by the moving fluid and make some bubbles. In a relatively small region of the parameter space the buckling coil will trap air bubbles in a very regular way, and these air bubbles will subsequently form surprising and very regular spiral patterns. We also present a very simple model that explains how these beautiful patterns are formed, and how the number of spiral branches and their curvature depends on the coiling frequency, the frequency of precession of the coiling center, the total flow rate, and the fluid film thickness. The main finding is that in addition to the coiling frequency, to get the spiral waves the center of the coil needs to precess with a second, different frequency. We show that this is both a necessary and sufficient condition to get Fermat's spirals. The idea that two different frequencies is sufficient and necessary to produce spirals was suggested theoretically (Hakim and Karma [41]) but has never been observed experimentally, to our knowledge.

A picture of steady 'liquid rope coiling' is shown in Fig. 4.1. Depending on the fluid viscosity, the pile of coils can have different shapes. In viscous regime for relatively high viscosities ($\nu \approx 1000$ cm^2/s) the pile remains intact for several coiling periods, becomes quite high, and has a shape like a corkscrew. For relatively low viscosities ($\nu \approx 100$ cm^2/s) the pile disappears within one or two coiling periods, and remains very low. In both these cases there are no bubbles generated.

For large falling heights ($H(g/\nu^2)^{1/3} \geq 1.2$) that inertial terms are important and the frequency of coiling is very high the viscous decay time is so big compared to the coiling time so the coiling filament forms a liquid tube that builds up, buckles under its own weight once a certain height is reached (Fig. 2.11), and starts rebuilding

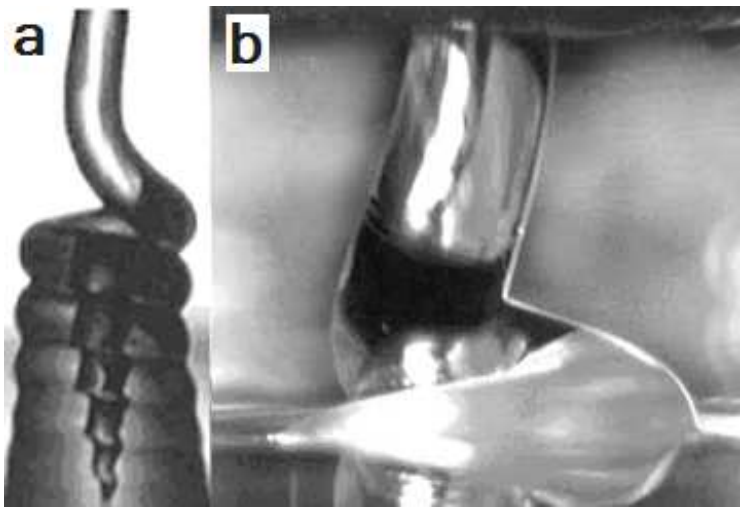

Figure 4.1: Liquid rope coiling. Depending on the fluid viscosity, the coils can either build up in a tall pile not unlike a corkscrew (a), or vanish into the bulk of the fluid within one coiling period (b). a) silicone oil with $\nu = 1000$ cm^2/s, injected from an orifice of radius $a_0 = 0.034$ cm at a volumetric rate $Q = 0.0044$ cm^3/s. Effective fall height $H = 0.5$ cm, The diameter of the portion of the rope shown is 0.06 cm. b) silicone oil with $\nu = 125$ cm^2/s, falling from an orifice of radius $a_0 = 0.2$ cm at a flow rate $Q = 0.1$ cm^3/s. Fall height is 1.5 cm. The diameter of the portion of the rope shown is 0.4 cm.

with a period. This second buckling traps an air bubble each time, but the patterns formed by these bubbles are very irregular. In this case we have tow different size for bubbles, very fine bubbles that forms during the coiling their size is less than the radius of the filament, and large bubbles with a size comparable to the diameter of the liquid tube. These bubbles form during the second buckling.

Inside a quite narrow region of the gravitational regime we observe the formation of very regular and beautiful spiral patterns (Fig. 4.2). What happens is the following. In all other regimes of coiling, the newly formed coil falls exactly on top of the one that was laid down previously. However in the gravitational regime, there is a slight irregularity in the position of the coils, leading to a slightly 'messy' pile of coils. This irregularity is due to the fact that the center of coiling tends to displace itself on a circle of its own, clearly with a frequency that is slower than that of the coiling. It is during the coalescence of two coils that are not exactly on top of each other that the small air bubbles are formed, and are trapped in the liquid due to the high viscosity. The bubbles are then advected away from the center radially by the flow, due to the action of gravity on the pile of material (Fig. 4.3). In a small range of height in gravitational regime the frequency of coiling and frequency of precession are in a way that the bubbles trapped regularly and this leads to the spiral patterns.

4.2 Experimental Process

We have performed these experiments using the first setup (Fig. 2.2 a) with silicone oils of different viscosities (ν = 100, 300, 1000, and 5000 cm^2/s) but have observed spiral patterns only for a viscosity of 300 cm^2/s. We also used different orifice diameters (d = 0.68, 1.5, 1.6, and 2.5 mm) and while we saw some irregular patterns for an orifice of 0.68 mm with flow rate of 0.02 cm^3/s and falling height of 30 mm, clear spiral patterns were observed for the 1.5 mm and 1.6 mm orifices with flow rates between 0.047 and 0.137 cm^3/s and heights between 32 and 50 mm.

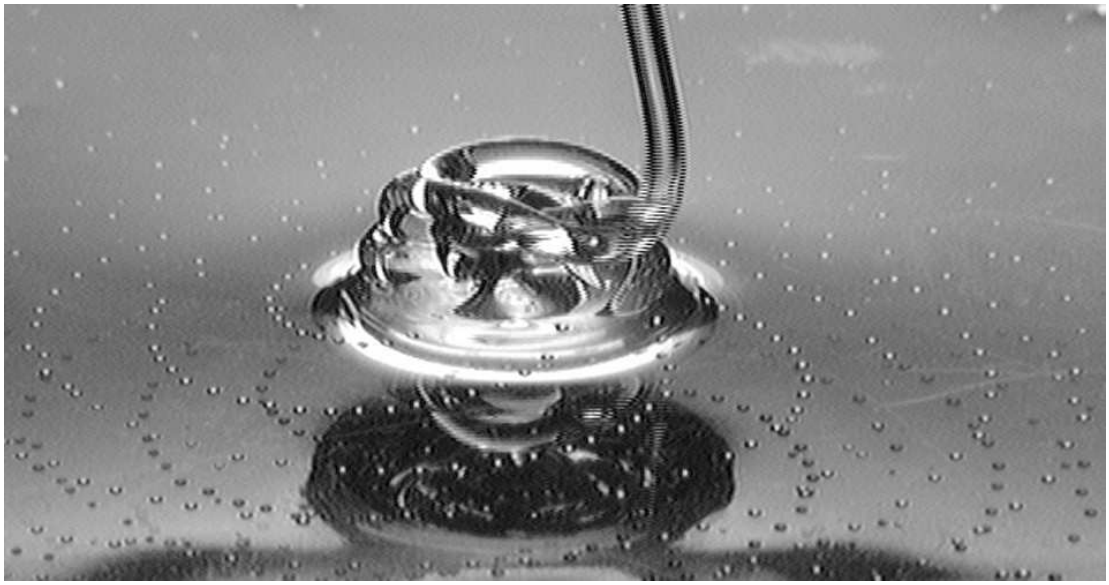

Figure 4.2: Inside a quite narrow region of the control parameter space, the coiling rope traps bubbles of air which form nice spiral patterns. Notice how the subsequent coils are displaced with respect to each other. The diameter of the pile is about 1 cm.

Figure 4.3: The process of air trapping and bubble formation. Reflection and refraction on the curved surface of the coils makes it difficult to study the details of bubble formation, but one can still follow the dynamics as seen in this series of pictures showing one cycle of bubble formation in two branches - one just above the center of the picture, and one in the upper right corner.

4.3 The Regime of Spiral Bubble Patterns

In the lowest part of the gravitational regimes there is a precession in the moving of the coil and there are some irregular bubbles, with increasing the height the bubble pattern become more regular and some unclear spiral pattern is observed. Increasing the height make the patterns more clear and finally near the upper end of the gravitational regime the patterns become unclear and disappear. Fig. 4.4 shows the numerically predicted curve of frequency vs. height using Ribe's method, for one of the experiment and the clear spiral pattern have been observed in a range of height between 3 to 4 cm from the orifice, before the step of frequency in the curve. At 4.5 cm from the orifice transition from low frequency level to high frequency level observed with no regular spiral pattern, so the spiral regime happens in gravitational before the inertio-gravitational regime. According to the numerical prediction the frequency of coiling in spiral regime should be nearly constant.

In all of the cases that spiral have been observed, the spiral patterns have five branches and five bubbles were generated after formation of nearly four coils. The bubble sizes increase with increasing flow rate and also depends on the height. For clear patterns the bubbles are larger than unclear patterns. The curvature of the branches depend on the flow rate, the falling height, and the direction of coiling. If the coiling direction is reversed after an external perturbation of the filament, the curvature of the branches changes sign as seen in Fig. 4.5. Changing the height lead to change the angular distance between every two bubbles in one branch and it changes the shape of the branches (Fig.4.6). While the branches are curved in most of the relevant parameter region, they can be almost straight (Fig.4.6(c)). We also observe that the shape of the patterns depends on the stagnation flow of the pile on the surface; if we modify the experiment by using a plane with boundaries at some distance from the center the stagnation flow will be slower and the branches closer together.

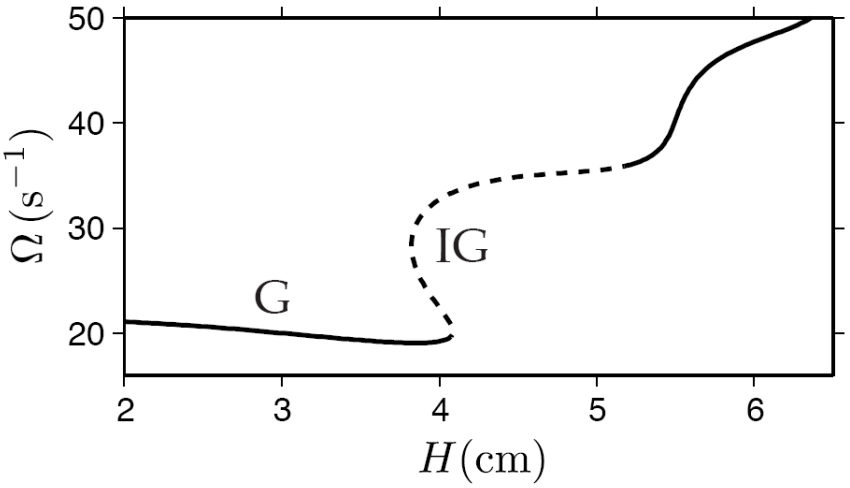

Figure 4.4: Angular coiling frequency Ω vs. fall height H for an experiment with $\nu = 300$ cm^2 s^{-1}, $d = 1.6$ mm, and $Q = 0.137$ cm^{3}s^{-1}, predicted numerically using the method of [19]. The symbols G and IG indicate portions of the curve corresponding to gravitational and inertio-gravitational (multivalued) coiling, respectively. The dashed portion of the curve indicates steady coiling states that are unstable to small perturbations, as determined using the method of [35]. Clear spiral patterns were observed in the height range $H = 3 - 4$ cm, before the turning point in the numerical curve that marks the onset of IG coiling [34]. The experimentally measured angular frequencies of coiling and precession were 17 ± 1 s^{-1} and 4 ± 1 s^{-1}, respectively.

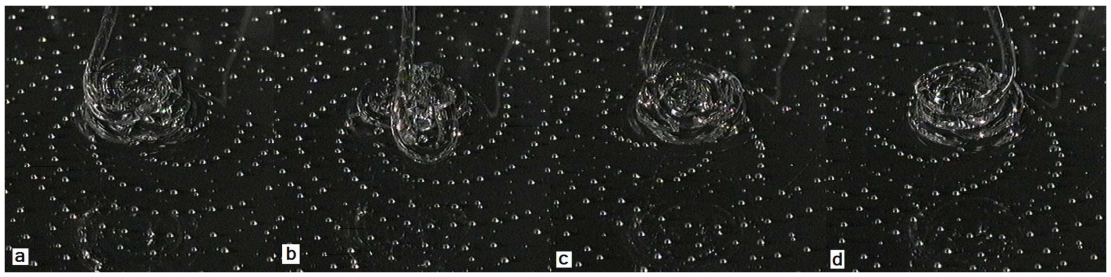

Figure 4.5: In rare instances the liquid rope spontaneously changes the direction of coiling. When this happens the curvature of the spiral pattern changes sign; (a) the rope is coiling clockwise when viewed from above and the spirals are curving clockwise when going towards the center. (b) The coil is in the middle of changing direction. Notice the 'extra coil' outside the pile. (c) the rope is now coiling in the counter clockwise direction and the spiral pattern is disturbed near the pile. (d) the coiling is counter clockwise and the curvature of the spiral pattern have changed sign.

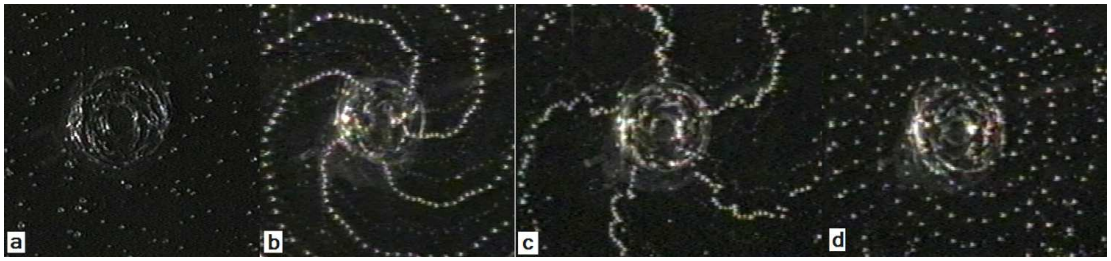

Figure 4.6: Increasing the height from a to d lead to change the angular distance between every two bubbles in one branch and it changes the shape of the branches. In all of these experiments the coiling was in a same direction the number of branches are 5. Photos were taken from below and the reflection of light from the glass substrate lead to appear some extra branches.

4.4 A Simple Model For The Spiral Pattern Formation

Using the experimental observations we now present a simple model for the formation of the spirals. The bubbles are generated because the center of coiling is not stationary but moves a little between each coil, and air is trapped between coils displaced with respect to each other. Subsequently the bubbles are transported radially with the stagnation flow. This will give rise to a Fermat's spiral (i.e. a spiral obeying $r = \pm a\theta^{0.5}$, where r is the radius, a some constant, and θ the angle), since $r \sim t^{0.5} \sim \theta^{0.5}$. To model this we assume that the coiling center moves on a circle of its own, and the path laid down by the coiling filament is then given by

$$X(t) = r_2 \cos(2\pi F_2 t) + r_1 \cos(2\pi F_1 t) \tag{4.1}$$

$$Y(t) = r_2 \sin(2\pi F_2 t) - r_1 \sin(2\pi F_1 t) \tag{4.2}$$

where r_2 and F_2 is the radius and frequency of the circle described by the motion of the coiling center, while r_1 and F_1 is the radius and frequency of coiling around this point (Fig. 4.7). The minus sign is there because the coiling was observed to always be in the opposite direction of the rotation of the coiling center and we want

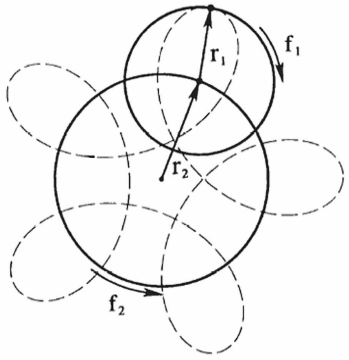

Figure 4.7: Coiling around a center which moves on a circle of its own. r_1 and F_1 are the radius and frequency of coiling, while r_2 and F_2 are the radius and frequency of precession of the coiling center. The direction of precession is in the opposite direction than that of the coiling. Here $r_2/r_1 = 1.43$ and $F_1/F_2 = 4$,[48].

to keep F_1 and F_2 positive. From our experiments we find that F_1/F_2 and r_1/r_2 are both about four. If we use these values to compute the path of the filament we observe that if F_1/F_2 is four exactly, the path will repeat itself after one rotation of the bubble generator while the path will be slightly shifted for each rotation if F_1/F_2 is only approximately but not exactly four (Fig. 4.8). Our experimental observations are consistent with one bubble being trapped at points 1 through 5 in Figs. 4.8, 4.9. This means that five bubbles will be generated for each four coils which is exactly what we observed experimentally when counting bubbles and coils. The reason for this is that the frequency of the coiling and the frequency of the rotation of the coiling center adds in the following way: A bubble is formed each time the vector from the rotation center to the coiling center is parallel to the vector from the coiling center to the filament laid down (see Fig. 4.7). That is, bubbles are formed at a frequency identical to the frequency of the rotation of the dot product.

$$\vec{r_1} \cdot \vec{r_2} = r_1 r_2(\cos(2\pi F_1 t)\cos(2\pi F_2 t) \tag{4.3}$$

$$- \sin(2\pi F_1 t)\sin(2\pi F_2 t)) \tag{4.4}$$

$$= r_1 r_2 \cos(2\pi(F_1 + F_2)t) \tag{4.5}$$

So the frequency of bubble generation is F_1+F_2 and the ratio of bubbles generated to the number of coils will be $(F_1 + F_2)/F_1$. For the measured value of $F_1/F_2 \approx 4$, this gives $(F_1 + F_2)/F_1 \approx 5/4$ just as observed. From the frequency of bubble generation one can also predict the number of spiral branches to be $n(F_1+F_2)/F_2$, where n is the smallest natural number that makes $n(F_1 + F_2)/F_2$ approximately a natural number. The reason that n must be there is that if F_1/F_2 is say 4.33, then $(F_1 + F_2)/F_2$ is 5.33 and it will take three rotations of the coiling center to add a bubble to all branches and start adding to the first one again - totaling 16 branches. The reason that $n(F_1 + F_2)/F_1$ needs not exactly be a natural number is that if it is sufficiently close, say 4.98, the bubbles will not be seen as being part of 50 branches but rather 5 branches that are slightly curved.

In order to test this model directly against our experiments we did a simple numerical simulation, where we assume that the coiling center precess with frequency F_2, the coiling happens with frequency F_1, and bubbles generated move radially with a speed given by $v = Q/(2\pi rh)$, where Q is the total flow rate, r the radial position, and h the height of the fluid film. In Fig. 4.10 we show a fit of this simple model to experimental data. The measured values are: F_1=2.7 Hz, F_2=0.7 Hz, Q=0.047 cm^{3}s^{-1}, and h=4 mm. The fitting parameters used to obtain agreement between the experimental bubbles and the model are: F_1=2.7 Hz, F_2=0.7 Hz, Q=0.047 cm^{3}s^{-1}, and h=3.6 mm, so the agreement is very good. In practice we inserted the experimentally obtained values in the model and saw what should be changed in order to obtain the best agreement. As we measured F_1, F_2, and Q we trusted those values and tried to change only h which gave a good match at h=3.6 mm. We attribute the slight difference between the two obtained values for h to the approximation $v = Q/(2\pi rh)$. Since the bubbles are near the top of the fluid, they will move slightly faster than the average as assumed above. This means that the average flow speed in the model must be slightly higher than the actual flow speed, which requires that flow takes place in a film with a slightly lower hight than the actual height. This simple model thus provides us with a not only qualitatively but also quantitatively detailed understanding of the formation of the spiral bubble patterns.

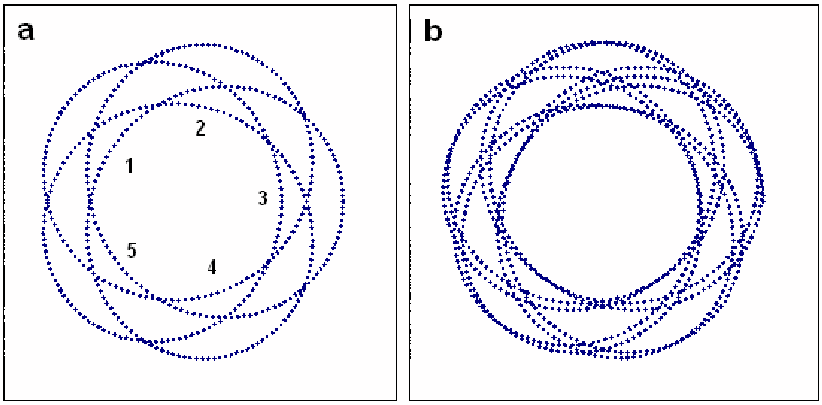

Figure 4.8: A model of the path laid down by the coil for the experimentally measured values of $r_1/r_2 \approx 4$ and $F_1/F_2 \approx 4$. (a) the path exactly repeats itself when $F_1/F_2 = 4$ giving rise to straight radial branches (Fig. 4.9(a), bubbles are generated at positions 1, 2, 3, 4, and 5. (b) When $F_1/F_2 = 3.9$ the path is slightly displaced for each precession, which gives rise to curved spiral branches (Fig. 4.9)(b).

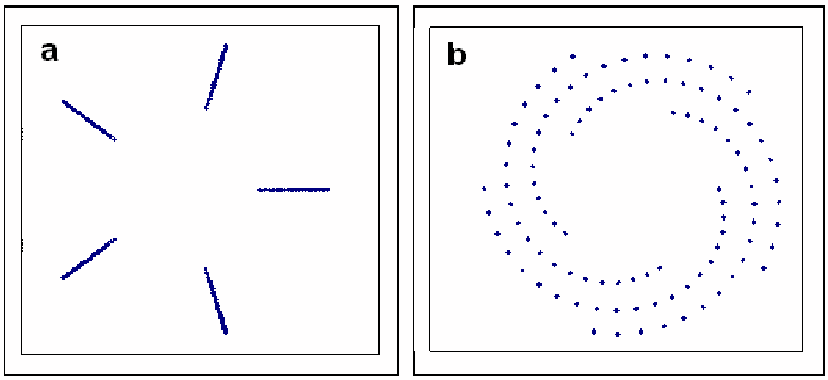

Figure 4.9: Patterns of bubbles generated at positions 1, 2, 3, 4, and 5 in Fig. 4.8. If F_1/F_2 is equal 4 exactly the loop is closed and the bubble branches are radial, but if F_1/F_2 is only approximately 4 the loop is open and the bubble branches will be curved.

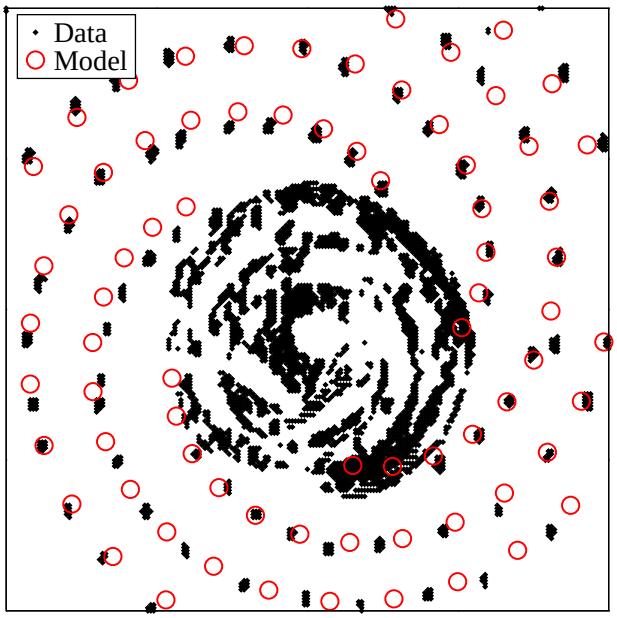

Figure 4.10: A fit of the theoretical model for the bubble patterns to the experimental data. The parameters of the model are: the frequencies of coiling $F_1 = 2.7\ Hz$, $F_2 = 0.7\ Hz$, the flow rate $Q = 0.137\ \mathrm{cm^3 s^{-1}}$, and the film height $h = 3.6\ mm$. The corresponding values measured directly from the experiment are $F_1 = 2.7\ Hz$, $F_2 = 0.7\ Hz$, $Q = 0.137\ \mathrm{cm^3 s^{-1}}$, and $h = 4$ mm.

4.5 Conclusion

In conclusion, we have shown the surprising formation of neatly ordered bubble patterns due to a superposition of two frequencies. In the coiling problem these correspond to the frequency of coiling and the frequency of precession of the center of the coils. Our experiment and the simple model rather convincingly shows that the existence of two different frequencies is sufficient to obtain such spiral patterns. This specific spiral is a particular type of an Archemedian spiral ($r = a\theta^{1/n}$), namely the Fermat's spiral: $r = a\theta^{1/2}$, as for a bubble $r \sim t^{1/2}$ and $\theta \sim t$ so that $r \sim \theta^{1/2}$.

Chapter 5

Rope Coiling

5.1 Introduction

All mountaineers know that a rope held vertically with its lower end in contact with a surface will coil spontaneously when it is dropped. The initial stage of the coiling is just the buckling of the rope under its own weight. In general, when a solid material buckles the subsequent non-linear evolution of the instability can occur in two ways. If the material is very stiff, it will break : it is for this reason that the resistance of structures to buckling and breaking is a key parameter in architecture and construction engineering. If on the other hand the material is sufficiently flexible, the structure remains intact but undergoes a large finite-amplitude deformation whose dynamics are essentially nonlinear. In many cases, the cause of the nonlinearity is the breakdown at large strain of an initially linear relation between stress and displacement, either because the nonlinear (quadratic) terms in the elastic strain tensor [1] become significant or because the material no longer satisfies Hooke's law. Much progress has been made recently in understanding these sorts of nonlinear behavior in structures such as crumpled sheets of paper [53, 54, 55, 56] and crumpled wires [57]. The other principal cause of nonlinearity is purely geometrical: the fact that the final (deformed) shape of the structure is unknown because it is far from that of the initial state. This sort of nonlinearity can obtain even if the material's elasticity is perfectly linear and Hookean, the classic example being the large deformation of elastic rods

and filaments described by the so-called Kirchhoff equations (for a review, see [58].) Manifestations of the geometrically nonlinear dynamics of elastic rods include the kinking of telephone cables on the ocean floor [59], handedness reversal in the coiled tendrils of climbing plants [60], the supercoiling of DNA strands [61], and the steady coiling of elastic ropes that we study here.

Some indication of the complex behavior that we might expect to find in elastic rope coiling is provided by the analogous phenomenon of 'liquid rope coiling', which we have explained in the previous chapters. In contrast to the liquid case, elastic rope coiling has received little attention. To our knowledge, no systematic experimental study of the phenomenon exists. The sole investigation of which we are aware is the numerical analysis of [20], who solved a system of asymptotic "slender body" equations for the steady coiling of a linearly elastic rope. These authors clearly identified (their eqn. (2.4)) a coiling regime in which elastic forces are balanced by gravity, and their Fig. 1 implies the existence of a second regime in which both gravity and inertia are negligible. However,it turns out that the terms representing inertia (Coriolis, centrifugal, and local) in the equations of [20] all have the wrong sign, and so their numerical results that involve inertia are incorrect.

Due to the apparent similarity of this phenomenon with liquid rope coiling, the theoretical analysis is similar, taking into account the elastic properties of the rope instead of fluid properties. Because in the case of a solid rope there is no gravitational stretching, the numerical investigation should in fact be easier than the liquid coiling. In contrast, the experiments are more difficult since the experimental parameters for a rope are not as easily controllable as those for the fluid.

In this chapter we present an experimental study of the coiling of elastic ropes falling onto (or being pushed against) a solid surface then we compare our experimental results with a numerical model [62], that is similar to [20] but with all the signs corrected. Our results show that coiling can occur in three distinct regimes - elastic, gravitational, and inertial - depending on how the elastic forces that resist the bending of the rope are balanced. Moreover, we find that the inertial regime comprises two distinct limits in which the rope's nearly vertical upper portion supports resonant "whirling string" and "whirling shaft" eigenmodes, respectively. By

means of a scaling analysis of the equations governing steady coiling, we determine quantitative scaling laws for the different regimes that relate the coiling radius and frequency to the fall height, the feed rate, and the rope's material properties. The correctness of these laws and the rich phase diagram they imply are validated by the excellent agreement of the experiments with the numerical predictions.

5.2 Experimental Methods

We used two different experimental setups to access the different coiling regimes. In the first setup (Fig.5.1), ordinary rope or sewing thread was wound onto a wheel, which was then rotated by an electric motor at a fixed rate (linear velocity on the circumference 0.3-200 cm s^{-1}) to feed the rope down through a hole onto a glass plate or thick piece of paper located 2-200 cm below. The coil radius was measured using calipers, and in some cases by counting pixels on photographs, to within 0.2 mm. The main experimental difficulty here is that commercially available ropes have a natural curvature equal to that of the spool onto which they are wound, and so tend to coil with a characteristic length scale close to that of spool's circumference. We eliminated the natural curvature in the ropes we used either by ironing them (thin ropes) or by wetting them with water and suspending them with a weight attached to the lower end (for thicker ropes.)

To achieve coiling at very low fall heights, we used a second setup in which pieces of spaghetti 24-26 cm long that had been presoftened by soaking in water were ejected downward from a vertical glass tube. The diameters (before soaking) of the two types of spaghetti were 1.3 mm or 1.9 mm, and 1.7 mm and 2.5 mm after soaking. The inner diameters of the tubes containing them were 2.5 mm and 2.7 mm, respectively. The spaghetti were loaded into the tube by placing them in water and using a syringe to suck them up (together with a surrounding layer of water), and were then ejected either using the syringe (for high U) or by pushing with a thin rod (to achieve lower values of U.) In both cases, U was measured by frame counting on movies taken with a webcam operating at 15 frames s^{-1} or a rapid CCD camera giving up to 1000

frames s^{-1}. Small fall heights H were measured to within 0.2 mm from photographs, and larger heights to within 1 mm using a ruler. The mass per unit length λ of each rope was measured by weighing a given length of it.

5.3 Young's Modulus Measurements

The Young's modulus E of different ropes was measured by observing the downward deflection of short pieces of the rope having one end clamped horizontally and the other end free. This also provided a severe test on any spontaneous curvature of the rope; it was verified in all cases that the deflection did not depend on the orientation of the rope. The linear theory of elastic rods [63] predicts that

$$\frac{\partial y^4}{\partial l^4} = -\frac{g\lambda}{EI} \tag{5.1}$$

$I = \frac{\pi a^4}{4}$ is the moment of inertia for rotation about an axis that coincides with diameter and a is the radius of the rope.

According to the Fig. 5.2 and because one end is free and other end is fixed, we have following boundary conditions:

$$(l = 0 : y = 0, \frac{\partial y}{\partial l} = 0)\&(l = L : y = D, \frac{\partial y^2}{\partial l^2} = 0, \frac{\partial y^3}{\partial l^3} = 0) \tag{5.2}$$

if we solve this partial deferential equation with these boundary conditions we will have the deflection of the free end of a rod of length L is:

$$D = \frac{8\lambda g}{2\pi E a^4} L^4 \tag{5.3}$$

For each rope, we measured D to within 0.05 mm using digital calipers for several different lengths L and then estimated E by least-squares regression of the data using the above formula (Fig. 5.3). Table 1 shows the values of λ and E for the different ropes we used; the error on the measurement of E is on the order of 20%. The values tabulated for the spaghetti are those measured after soaking for 2.5 hours (smaller

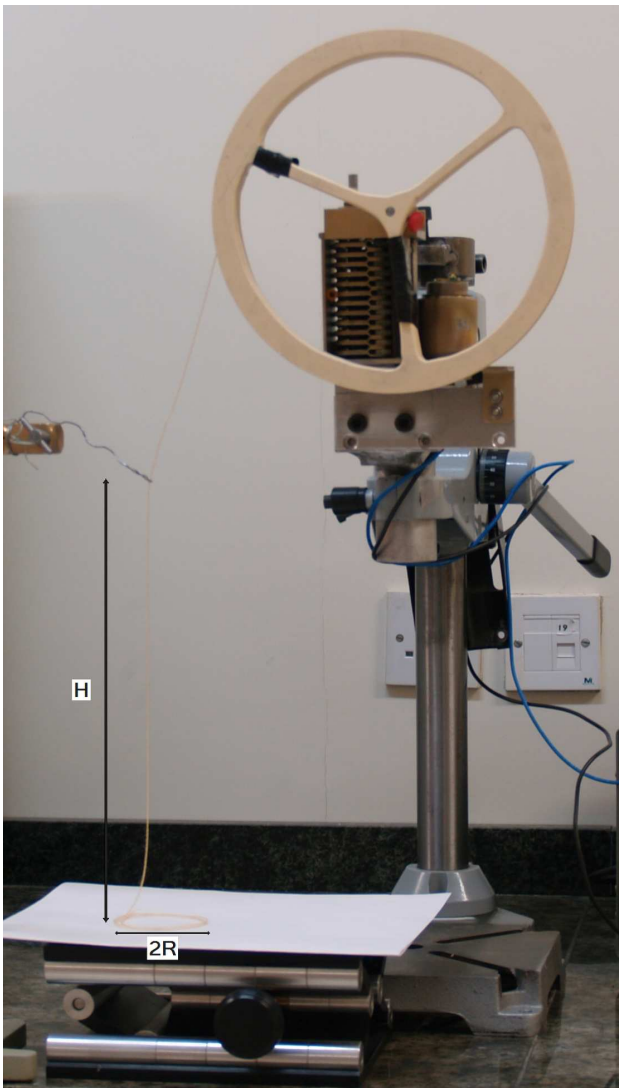

Figure 5.1: The first setup for rope experiment.

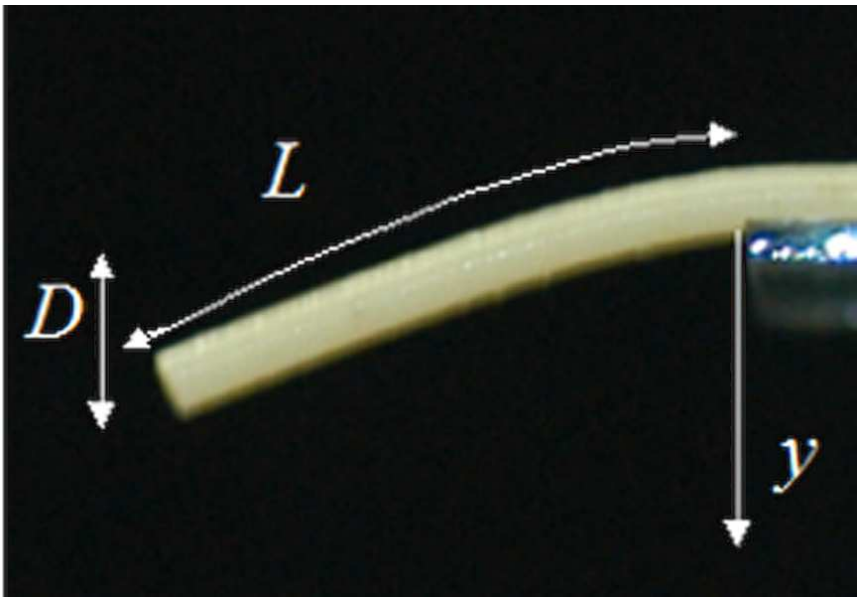

Figure 5.2: Deflection of Spaghetti.

diameter) and 6 hours (larger diameter) in water at 25° C.

5.4 Experimental Observations

For most of the ropes listed in Table 1 we carried out two series of experiments: one varying the fall height H with the feed rate U fixed, and a second varying U with H fixed. Fig. 5.4 shows some of the typical coiling configurations we observed, and Fig. 5.5 shows a selection of our experimental measurements of the coil radius R as a function of H and U. Two different types of behavior are seen, depending on whether the coiling object is spaghetti fed from very low heights ($\leq$ 1.3 cm in Fig. 5.5) or thread fed from a height of at least several cm. For the spaghetti (Fig. 5.4 a; open squares in Fig. 5.5), R increases with H (Fig. 5.5a) but is nearly independent of U (Fig. 5.5b.) For threads, R also increases with height (open circles and solid squares in Fig. 5.5 a.) However, the dependence on U is more complicated: R is first nearly independent of U, then increases, then decreases by a factor ≈ 2, and may

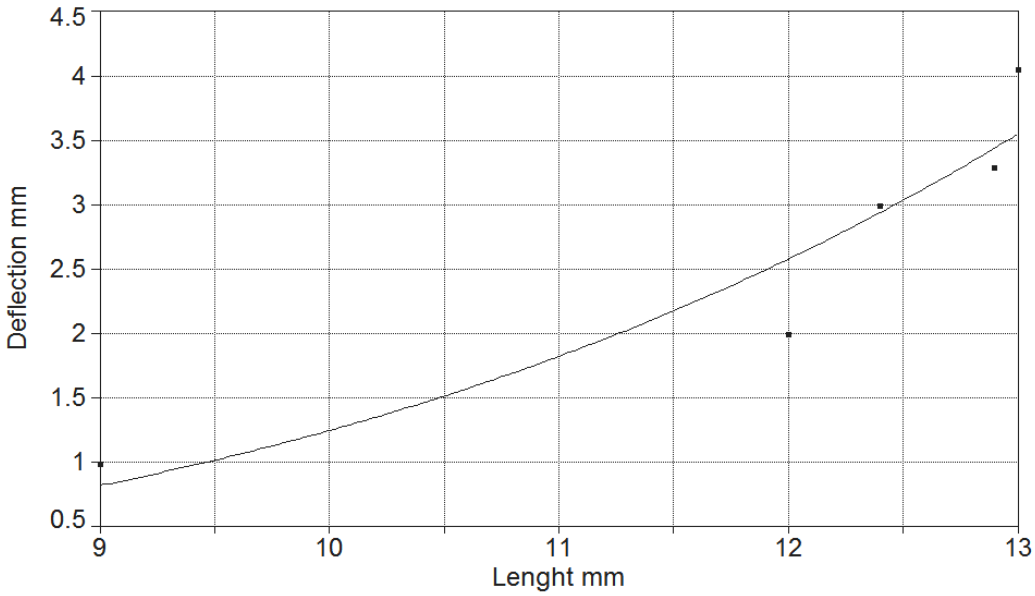

Figure 5.3: Deflection vs. length for spaghetti N°7, after 6 hours soaking in water, Error bars on the length and deflection are less than 0.5 mm, $D = aL^4$ is the general form of the solid curve that was fitted to the experimental data using Tablecurve software, $a = 1.2 * 10^{-4}$ mm^{-3}, R^2 =0.885.

Rope	Composition	λ (kg m^{-1})	d (mm)	E (Pa)
1	Polyester thread	0.000299	1.5	1.5×10^5
2	Cotton thread	0.00011	0.5	2.9×10^6
3	Cotton Thread	0.00011	0.5	1.5×10^7
4	Thick Cotton Thread	0.00024	1	8.2×10^5
5	Thin cotton rope	0.00237	3.35	1.9×10^5
6	Silk thread	0.00029	0.75	8.5×10^6
7	Thick cotton rope	0.02169	6.5	4.1×10^6
8	Cotton Thread	0.001	0.6	2×10^6
9	Polyester Rope	0.04	3	2×10^7
10	Spaghetti no. 5	0.0027	1.7	6.9×10^4
11	Spaghetti no. 7	0.006	2.5	5.2×10^4

Table 5.1: Physical property of some ropes and spaghetti; the error on the measurement of E is on the order of 20%.

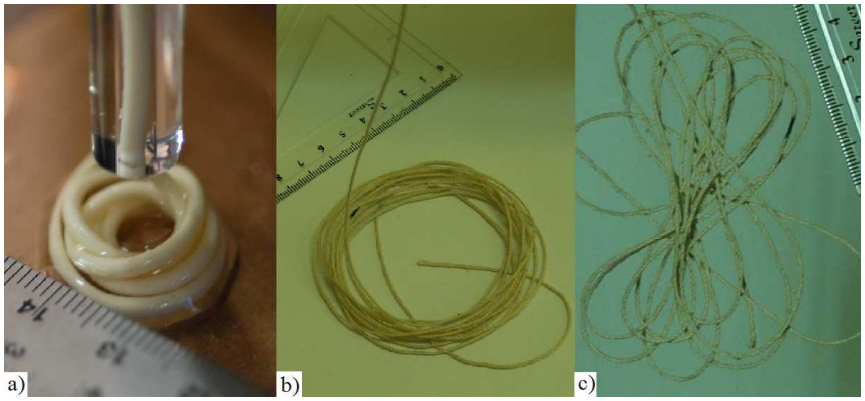

Figure 5.4: Typical coiling configurations for some of the ropes whose physical properties are listed in Table 1. The numbers on the scale in each panel indicate cm. (a) rope type 10, $H = 1.2$ cm, $U = 26$ cm/s; (b) rope type 4, $H = 30$ cm, $U = 2.3$ cm/s; (c) rope type 4, $H = 80$ cm, $U = 100$ cm/s.

even increase slightly again (open and solid circles in Fig. 5.5b.) Moreover, at high feed rates the thread sometimes becomes unstable to an unsteady 'figure of eight' coiling mode (Fig.5.4c) that can persist as long as the length of the thread permits, in contrast to the transient nature of such patterns in liquid rope coiling [34, 32].

5.5 Numerical Slender-rope Model

The diversity of behavior shown in Fig. 5.5 can be understood with the help of an asymptotic "slender rope" model. The equations we use are those of [20], but with corrections to the sign of the inertial terms and the expression for the moment of inertia I ($\equiv \pi d^4/64$) of the rope's cross-section about a diameter. These equations describe the steady (in the co-rotating reference frame) motion of a slender rope acted on by gravity, inertia, and the elastic forces that resist bending, and constitute a thirteenth-order system of ODEs in which the independent variable is the arclength s along the rope's axis. Because both the coil radius R and the length ℓ of the rope between the feeding point and the contact point are unknown *a priori*, fifteen boundary conditions are required. We solved the resulting two-point boundary value problem using the continuation method described by [20].

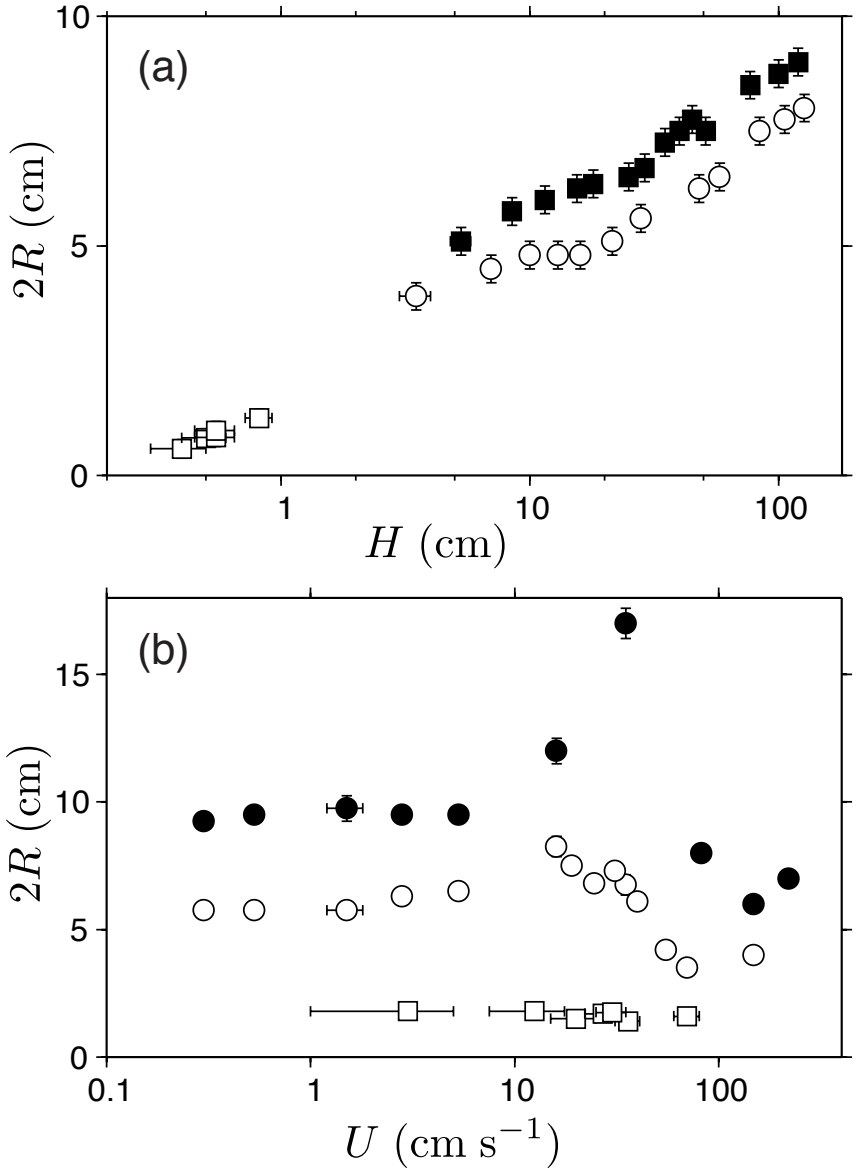

Figure 5.5: Selected experimental measurements of the coil radius R. (a) R as a function of fall height H for rope type 10 with $U = 2$ cm/s (open squares), rope type 1 with $U = 10$ cm/s (solid squares), and rope type 2 with $U = 10$ cm/s (open circles.) (b) R as a function of feed rate U for rope type 10 with $H = 1.3$ cm (open squares), rope type 1 with $H = 50$ cm (solid circles), and rope type 2 with $H = 100$ cm (open circles.) The physical properties of the ropes are listed in Table 1.

Because the numerical solutions predict the existence of resonant eigenmodes (see below), it is natural to discuss the results in terms of the coiling frequency $\Omega \equiv U/R$ rather than the coil radius R. Nondimensionalization of the governing equations shows that the dimensionless coiling frequency $\hat{\Omega} \equiv \Omega(d^2E/\rho g^4)^{1/6}$ depends only on the dimensionless fall height $\hat{H} \equiv H(\rho g/d^2E)^{1/3}$ and the dimensionless feed rate $\hat{U} \equiv U(\rho/d^2g^2E)^{1/6}$. Fig. 5.6 shows numerically calculated curves of $\hat{\Omega}(\hat{H})$ for for several values of $\hat{U}$. Coiling can occur in either of three regimes, depending on how the elastic forces that resist the bending of the "coil" portion of the rope are balanced. Per unit rope length, the magnitudes of the elastic (E), gravitational (G), and inertial (I) forces in the coil are

$$F_E \approx Ed^4R^{-3} \quad F_G \approx \rho g d^2, \quad F_I \approx \rho d^2 U^2 R^{-1}. \tag{5.4}$$

In the first regime, which we call "elastic" coiling, both gravity and inertia are negligible ($F_G, F_I \ll F_E$) and the net elastic force acting on every element of the rope is zero. A second "gravitational" regime occurs when inertia is negligible and the elastic forces are balanced by gravity ($F_G \approx F_V \gg F_I$.) Finally, "inertial" coiling occurs when gravity is negligible and the elastic forces are balanced by inertia ($F_I \approx F_V \gg F_G$.) The corresponding coiling frequencies Ω_E, Ω_G and Ω_I can be found by estimating the coil radius R and then using the relation $\Omega = U/R$ for conservation of volume flux at the moving contact point. For elastic coiling, $R \sim H$. For gravitational and inertial coiling, R is obtained from the force balances $F_G \approx F_E$ and $F_I \approx F_E$, respectively. The results are

$$\Omega_E \sim UH^{-1}, \;\; \Omega_G \sim U(\rho g/d^2E)^{1/3}, \;\; \Omega_I \sim U^2(\rho/d^2E)^{1/2}, \tag{5.5}$$

The above expression for Ω_E corresponds to the portions of the curves with slope $= -1$ (labeled E) on the left side of Fig. 5.6. The scaling law for Ω_G (equivalent to eqn. (2.4) of [20]) corresponds to the nearly horizontal portions of the curves labeled G at the bottom right of Fig. 5.6 (the numerics show that Ω_G also depends on H, but in a way that is too weak to be determined by scaling analysis.) Finally, the scaling

law for Ω_I corresponds to the horizontal lines labeled I at the upper right of Fig. 5.6.

Fig. 5.6 reveals a surprising complexity in the inertial regime, where $\hat{\Omega}(\hat{H})$ oscillates about the horizontal lines defined by the expression (5.5) for Ω_I. This behavior reflects the presence of resonant eigenmodes in the "tail" of the rope that are excited whenever one of their natural frequencies is close to the inertial frequency Ω_I set by the coil. Two limiting forms of these resonant modes can be identified. In the first limit, represented e.g. by the rightmost portion of the curve $\hat{\Omega}(\hat{H})$ for $\hat{U} = 1.0$ in Fig. 5.6, the tail of the rope behaves as a steadily whirling elastic "string" (i.e., a rope with zero bending resistance) under gravity. If the string is nearly vertical, its lateral deflection $r(s)$ satisfies the (singular) eigenvalue problem

$$0 = g(H - s)r'' - gr' + \Omega^2 r, \quad r(0) = 0, \;\; r(H) \text{ finite} \tag{5.6}$$

where primes indicate differentiation with respect to the arclength $s \in [0, H]$ measured along the string from the feeding point $s = 0$. The three terms in (5.6) represent the components perpendicular to the string's axis of the elastic tension, the gravitational force, and the centrifugal force, respectively. The problem (5.6), which also describes the small oscillations of a hanging chain [63], has eigenfrequencies Ω_n^{string} that satisfy $J_0(2\beta) = 0$, where $\beta = \Omega_n^{\text{string}}(H/g)^{1/2}$ and J_0 is the Bessel function of the first kind of order zero. The first six eigenfrequencies Ω_n^{string} are shown by the dotted lines with slope $-1/2$ near the center of Fig. 5.6. Note the close coincidence of Ω_n^{string} for $n \geq 5$ with the segments of the curve $\hat{\Omega}(\hat{H})$ for $\hat{U} = 1.0$. Moreover, in the limit $\hat{H} \to \infty$ the frequency Ω_G of the gravitational mode merges smoothly with the frequency Ω_1^{string} of the gravest whirling string mode.

In the second limit, the tail behaves as what Love [63] (§ 286) called a "whirling shaft", in which the centrifugal force is balanced by the elastic resistance to bending. The lateral displacement of the tail now satisfies

$$\frac{Ed^2}{16\rho} r'''' = \Omega^2 r. \tag{5.7}$$

Solving (5.7) subject to the boundary conditions $y(0) = y'(0) = 0$ (clamped end) and $y''(H) = y'''(H) = 0$ (free end), we find that the eigenfrequencies Ω_n^{shaft} satisfy $\cos p \cosh p = -1$, where $p^2 = 4H^2(\rho/d^2E)^{1/2}\Omega_n^{\text{shaft}}$. The first six of these eigenfrequencies are shown by dashed lines with slope -2 on Fig. 5.6. For $n \geq 5$, Ω_n^{shaft} aligns closely with the segments of the curves $\hat{\Omega}(\hat{H})$ for $\hat{U} = 3.16$ and 10.

The phase diagram implied by the curves $\hat{\Omega}(\hat{H}, \hat{U})$ in Fig. 5.6 is shown as an inset at the upper right of the same figure. The $(\hat{H}, \hat{U})$-plane is divided into three broad regions representing elastic (E), gravitational (G) and inertial (I) coiling. The inertial region in turn comprises two parts corresponding to the "whirling string" and "whirling shaft" resonant modes, with a smooth transition between them.

5.6 Comparison With Experiment and With Liquid Rope Coiling

Fig. 5.7 shows the dimensionless coiling frequencies measured in four series of experiments (circles), together with the predictions of the numerical model for the same values of H, U, λ, E, and d (solid lines.) Three of the four regimes (E, G, and I_{string}) are clearly captured by the experiments, and the fourth (I_{shaft}) is represented by the topmost circle in Fig. 5.7 d. The excellent agreement between the numerics and the experiments is strong evidence for the validity of the scaling laws and the general phase diagram presented above.

In closing, we compare the behavior of coiling elastic and liquid 'ropes'. The primary difference between the two is that a falling liquid rope is stretched by gravity, so that its diameter decreases downward from the hole from which it was ejected. Allowing for this effect, however, one finds that liquid rope coiling has 'viscous' and 'gravitational' regimes that are exactly analogous to the elastic and gravitational coiling regimes, respectively, of an elastic rope [19, 31]. Matters are somewhat more complicated if inertia is significant. Ribe et al. [34] showed experimentally and theoretically that liquid ropes can support "whirling string" resonant modes analogous to those documented here, but with eigenfrequencies that are modified by the rope's

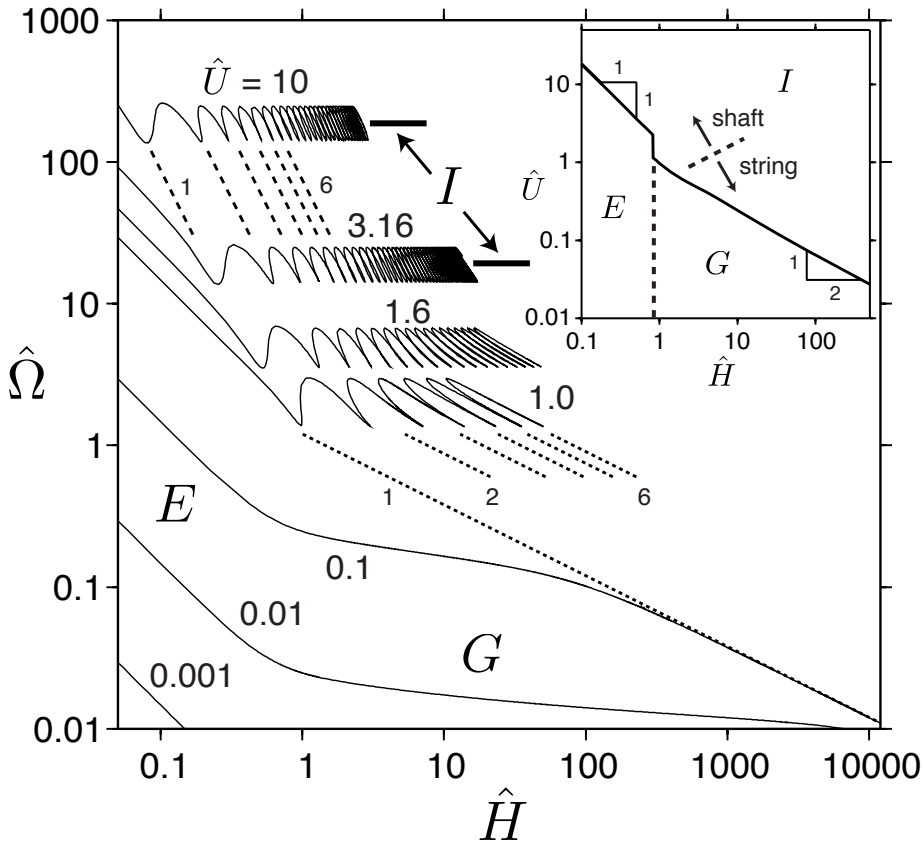

Figure 5.6: Main portion: Dimensionless coiling frequency $\hat{\Omega} \equiv \Omega(d^2E/\rho g^4)^{1/6}$ as a function of dimensionless fall height $\hat{H} \equiv H(\rho g/d^2E)^{1/3}$ for several values of the dimensionless feed rate $\hat{U} \equiv U(\rho/d^2g^2E)^{1/6}$. The curves for $\hat{U} \geq 1.0$ continue indefinitely to the right (continuations not shown for clarity.) Thick horizontal bars correspond to the inertial frequency Ω_I defined by (5.5). The first six "whirling string" and "whirling shaft" eigenfrequencies are indicated by dotted and dashed lines, respectively. Inset: Phase diagram for elastic coiling as a function of $\hat{H}$ and $\hat{U}$. The coiling frequency $\hat{\Omega}(\hat{H}, \hat{U})$ is multivalued everywhere above the solid line. The vertical dashed line indicates the approximate location of the smooth transition between elastic (E) and gravitational (G) coiling. The dashed line in the inertial (I) portion of the diagram indicates a smooth transition between "whirling string" and "whirling shaft" resonant modes.

nonuniform diameter. By contrast, there is no experimental or numerical evidence that "whirling shaft" eigenmodes can exist on liquid ropes, probably because of viscous damping. But even the whirling string modes on a liquid rope disappear if the fall height is sufficiently great, at which point coiling occurs in the 'pure' inertial regime identified by [18]. This regime has no equivalent in an elastic rope, for which the resonant modes seen in Fig. 5.6 appear to persist (as far as one can tell from the numerics) to arbitrarily large heights.

5.7 Conclusions

In this chapter we have investigated coiling of a falling rope using a combination of laboratory experiments with cotton threads and softened spaghetti. we measured the elastic modulus of the ropes by measuring the downward deflection of short pieces of the rope having one end clamped horizontally and the other end free. This allows to compare our experimental results with a numerical model based on asymptotic "slender rope" theory that was introduced by Ribe [62]. We found that coiling can occur in three distinct regimes - elastic, gravitational, and inertial - depending on how the elastic forces that resist the bending of the rope are balanced. Moreover, we find that the inertial regime comprises two distinct limits in which the rope's nearly vertical upper portion supports resonant "whirling string" and "whirling shaft" eigenmodes, respectively. We presented a complete phase diagram for rope coiling in the fall height-feed rate space, together with scaling laws for the coiling radius and frequency as a function of height, feed rate, and the rope's material properties. The validity of these results is confirmed by the excellent agreement between the experiments and the numerics.

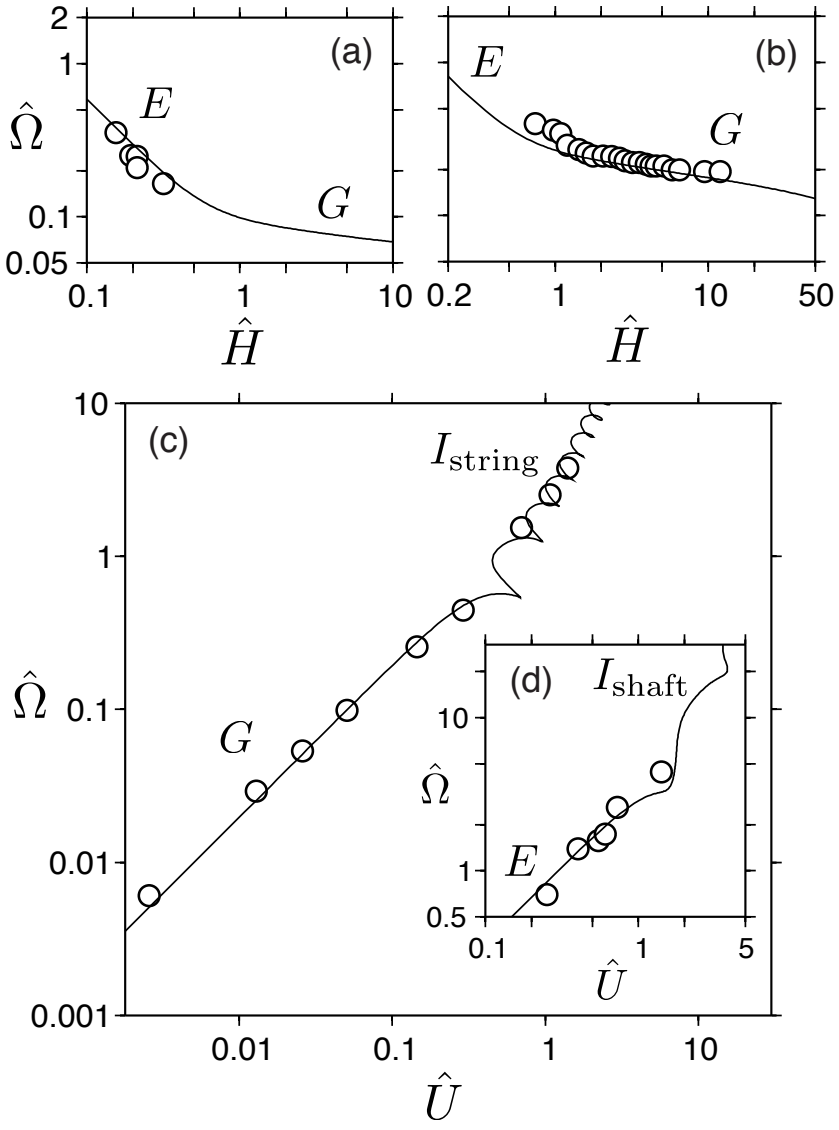

Figure 5.7: Comparison of experimentally measured (symbols) and numerically calculated (solid lines) coiling frequencies. The dimensionless frequency $\hat{\Omega}$, fall height $\hat{H}$ and feed rate $\hat{U}$ are defined in the text. The symbols E, G, and I indicate elastic, gravitational, and inertial coiling, respectively, and the subscripts "string" and "shaft" indicate the dominant resonant mode type in the portion of the inertial regime in question. Error bars reflecting the composite (propagated) errors of Ω, H, U, λ, d and E are comparable to the symbol sizes in most cases and are omitted for clarity. (a) Rope type 10 with $U = 2$ cm/s; (b) Rope type 3 with $U = 10$ cm/s; (c) Rope type 3 with $H = 30$ cm; (d) Rope type 10 with $H = 1.3$ cm.

Chapter 6

General Conclusion

When a falling fluid jet impacts unto a horizontal surface it buckles and starts to coil, as one sees when playing with the spoon in the honey jar. It is a common observation that a vertically held rope will coil spontaneously when its lower end is in contact with a surface, and its upper end is let loose: a circular pile of rope will form spontaneously on the surface. The coiling problem is very complicated, since it involves the non-linear elastic behavior of the rope or the simultaneous stretching and bending of the liquid jet. In spite of the generality of the coiling phenomenon, it has not been studied in great detail. In this thesis we have tried to propose a detailed experimental study of the coiling instability in viscous and elastic filaments.

A High viscosity can allow for instabilities like buckling instability, which happens only for high viscous liquids (orders of magnitude more viscous than water with a viscosity of $\sim$ 1 mPa.s). What happens when a falling fluid jet impacts unto a horizontal surface depends profoundly on the Reynolds number. If it is above some critical value a hydraulic jump with a region of supercritical flow is formed. If it is decreased below this value, a less spectacular regime is encountered, where the jet simply descends into the bulk of the fluid in a stagnation flow. Both regimes can be seen when one turns on the water and the water falls into a sink. If the Reynolds number is decreased further below some even lower critical value however, the jet becomes unstable and starts buckling as one sees at the breakfast table when pouring honey on the toast.

In chapter 2, we studied the coiling instability for a liquid thread. We report a

detailed experimental study of the coiling instability of viscous jets on solid surfaces. In the experiment a viscous fluid with density ρ, kinematic viscosity ν and surface tension γ is injected at a volumetric rate Q from a hole of diameter $d = 2a_0$ and then falls a distance H onto a solid surface. In general, the rope comprises a long, nearly vertical "tail" and a helical "coil" of radius R near the plate. The motion of a coiling jet is controlled by the balance between viscous forces, gravity and inertia. The dynamical regime in which coiling takes place is determined by the magnitudes of the viscous (F_V), gravitational (F_G) and inertial (F_I) forces. We found that the frequency of coiling was strongly controlled by the height of fall, and changing the height lead to transition through three different regimes of coiling (viscous, gravitational and inertial). For small dimensionless heights $H(g/\nu^2)^{1/3} < 0.08$, coiling occurs in the viscous (V) regime, in which both gravity and inertia are negligible and the net viscous force on each fluid element is zero. Coiling is here driven entirely by the injection of the fluid, like toothpaste squeezed from a tube. At $0.08 \leq H(g/\nu^2)^{1/3} \leq 0.4$, when inertia is negligible, viscous forces in the coil are balanced by gravity ($F_G \approx F_V \gg F_I$,), giving rise to gravitational (G) coiling. When the height gradually increases to $H(g/\nu^2)^{1/3} \approx 1.2$, a third mode, 'inertial' coiling is observed. We present experimental measurements of frequency vs. height in each regime and measured the radii of the coil and the jet and compared them to a numerical calculation of the coiling. We also describe "secondary buckling", which is the buckling of the column of coils in the high frequency regime, and present measurements of the critical (buckling) height of the column. In order to physically understand secondary buckling, we apply dimensional analysis to measurements of the critical heights of different laboratory experiments.

In the transition from gravitational to inertial coiling ($0.4 \leq H(g/\nu^2)^{1/3} \leq 1.2$), the frequency vs. height was multivalued, and could jump between two frequencies during time. In chapter 3 we investigated experimentally the coexistence of multiple coiling states with different frequencies at a fixed value of the fall height. In addition to the three coiling modes previously identified (viscous, gravitational, and inertial), we found a new multivalued "inertio-gravitational" coiling mode that occurs at heights intermediate between gravitational and inertial coiling, where the rope is strongly stretched by gravity. The frequencies of the individual branches in the frequency vs.

height curves, are proportional to $(g/H)^{1/2}$ (the pendulum frequency), and agree closely with the eigen frequencies of a whirling liquid string with negligible resistance to bending and twisting. The laboratory experiments are in excellent agreement with predictions from the numerics. Inertio-gravitational coiling is characterized by oscillations between states with different frequencies, and we present experimental observations of four distinct branches of such states in the fall height-frequency space. The transitions between coexisting states have no characteristic period, may take place with or without a change in the sense of rotation, and usually but not always occur via an intermediate figure of eight state. Based on the experimental results we proposed that, where we have no experimental data on the frequency vs. height curve there should be an instability. Using linear stability analysis we could subsequently show that the multivalued portion of the curve of steady coiling frequency vs. height comprises alternating stable and unstable segments and steady coiling in the multivalued 'inertio-gravitational' (IG) regime is stable only along discrete segments of the frequency vs. height curve, the distribution of which agrees very well with our measurements. The stability analysis further shows that coiling is stable at all heights in the three remaining regimes (viscous, gravitational, and inertial), also in agreement with the experiments.

In a relatively small region in the gravitational coiling regime the buckling coil will trap air bubbles in a very regular way, and these air bubbles will subsequently form surprising and very regular spiral patterns. We investigated this phenomenon in chapter 4. Near the horizontal surface where the filament starts to coil there is a pile of fluid, the shape and the dynamic of the pile depends on the viscosity of fluid, the flow rate, the frequency of coiling and also on the height of fall. Depending on system parameters there can be generation of bubbles in the pile of fluid, the size and distribution of which depends on the dynamics of the pile. In all of the experiments the spirals have five branches and five bubbles were generated after formation of about four coils. The direction of coiling determines the direction of the spirals. The curvature of the branches also depends on the height of fall and the radial speed of the moving fluid on the substrate. We also presented a very simple model that explains how these beautiful patterns are formed, and how the number of spiral branches and

their curvature depends on the physical parameters of the problem. In this model we assumed that the coiling center moves on a circle of its own. Different ratios of the radii and frequencies of coiling and precession can lead to different paths for the filament on the substrate. When we put our experimentally measured parameters into the model we found a path with five triangular loops that we inferred are where the bubbles were generated. Finally we have shown that the surprising formation of neatly ordered bubble patterns is due to a superposition of two frequencies. In the coiling problem these correspond to the frequency of coiling and the frequency of precession of the center of the coils. Our experiment and the simple model rather convincingly shows that the existence of two different frequencies is sufficient to obtain such spiral patterns. This specific spiral is a particular type of an Archemedian spiral ($r = a\theta^{1/n}$), namely the Fermat's spiral: $r = a\theta^{1/2}$, as for a bubble $r \sim t^{1/2}$ and $\theta \sim t$ so that $r \sim \theta^{1/2}$.

We pursue our study considering solid ropes All mountaineers know that when a rope is dropped it forms some coils. The initiation of this is that the rope buckles under its own weight. In general, when a solid material buckles there are two possibilities for the non-linear evolution of the buckling instability. If the material is stiff, it will generally break and the resistance to buckling (and hence breaking) is therefore a key parameter in architecture and construction engineering, that has consequently been studied extensively. On the other hand, if the material is sufficiently flexible, it will not break, but rather do what the rope does, and start coiling. The geometrical non-linear elastic behavior of thin flexible rods, has attracted less attention than the breaking problem, and this is what needs to be understood to describe ropes. In chapter 5 we presented an experimental study of "solid rope coiling", we studied the coiling of both real ropes and spaghetti falling or being pushed onto a solid surface. We also compared our experimental results with a numerical model based on asymptotic "slender rope" theory. We found that coiling can occur in three distinct regimes, (elastic, gravitational, and inertial) depending on how the elastic forces that resist the bending of the rope are balanced. Moreover, we found that the inertial regime comprises two distinct limits in which the rope's nearly vertical upper portion supports resonant "whirling string" and "whirling shaft" eigenmodes, respectively.

We presented a complete phase diagram for rope coiling in the fall height-feed rate space, together with scaling laws for the coiling radius and frequency as a function of height, feed rate, and the rope's material properties. The validity of these results is confirmed by the excellent agreement between the experiments and the numerics.

Appendix A

Numerical Model

A.1 Introduction:

The equations for a thin viscous rope have been derived by Entov and Yarin [22, 23], who described the geometry of the rope's axis using the standard triad of basis vectors from differential geometry (the unit tangent, the principal normal, and the binormal). Here we present the numerical model that Ribe has introduced to investigate the coiling problem and that we have used throughout this thesis to compare to our experimental results.

A.2 Numerical model for liquid coiling and the homotopy method to solve the equations:

Using a numerical approach, Ribe [19] modelled coiling in the whole frequency range, and found three coiling modes with different dynamics. The configuration he studied is shown in Fig. 2.1. A fluid with kinematic viscosity ν and volumetric flow rate Q is injected through a hole of radius a_0 and falls a distance H onto a plate. It is assumed that the jet's point of contact with the plate rotates with angular velocity Ω and describes a circle of radius R. In most cases, the jet consists of a long, nearly vertical 'tail', which feeds fluid to a 'coil' next to the plate.

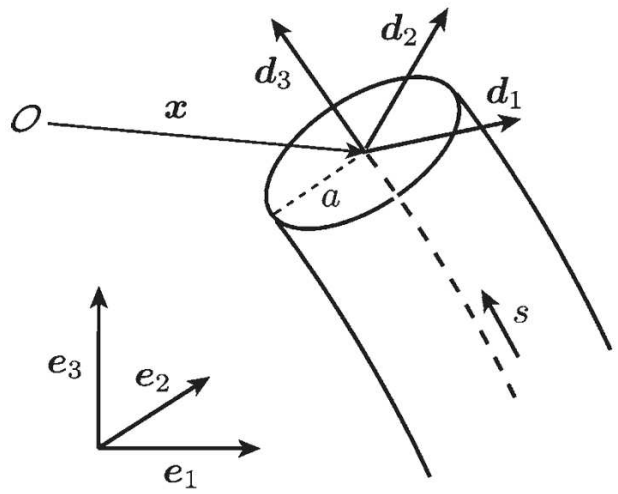

Figure A.1: Geometry of a viscous jet. The Cartesian coordinates of the jet's axis relative to an arbitrary origin O are $\vec{x}(s)$, where s is the arc-length along the axis. The jet's radius is $a(s)$. The unit tangent vector to the jet axis is $\hat{d}_3(s) \equiv \vec{x}'$, and $\hat{d}_1(s)$ and $\hat{d}_2(s) \equiv \hat{d}_3 \times \hat{d}_1$ are material unit vectors in the plane of the jet's cross-section. [19].

Here we present Ribe's formulation [19] in which the basis vectors normal to the rope's axis are material vectors that are convected with the fluid.

To write the governing equations of the steady coiling, we consider a slender jet whose radius is everywhere much smaller than the local radius of curvature of its axis. This allows us to reduce the three-dimensional Navier-Stokes equations for the flow within the jet to one-dimensional equations for a line having finite resistance to stretching, bending, and twisting. The problem is then reduced to a steady, time-independent motion by working in a reference frame that rotates with the coil. All the dependent variables are then functions only of the arc-length s along the jet axis, which ranges from $s = 0$ (the injection point) to $s = l$ (the point of contact with the plate). We denote the differentiation with respect to s by a prime. All Latin indices range over the values 1, 2, and 3, while Greek indices range over 1 and 2 . The Einstein summation convention over repeated indices is assumed throughout.

Figure A.1 shows an element of a slender viscous jet with variable radius $a(s)$. The Cartesian coordinates of the jet's axis relative to unit vectors $\hat{e}_i$ rotating with the

coil are $\vec{x}(s)$, defined such that $(x_1, x_2, x_3) = (0, 0, 0)$ is the point where the fluid is injected. The vector $\hat{e}_3$ points up, opposite to the gravitational acceleration $\vec{g} = -g\hat{e}_3$. At each point on the jet's axis, we define a set of three orthogonal unit vectors including the tangent vector $\hat{d}_3(s) \equiv \vec{x}\,'$ and two vectors $\hat{d}_1(s)$ and $\hat{d}_2(s) \equiv \hat{d}_3 \times \hat{d}_1$ in the plane of the jet's cross-section. The vectors $\hat{d}_1$ and $\hat{d}_2$ are arbitrary, but are assumed to be material vectors rotating with the fluid. Let y_1 and y_2 be orthogonal coordinates normal to the jet axis in the directions $\hat{d}_1$ and $\hat{d}_2$, respectively. The Cartesian coordinates of an arbitrary point within the jet are then

$$\vec{r}(s, y_1, y_2) = \vec{x} + y_1\hat{d}_1 + y_2\hat{d}_2 = \vec{x} + \vec{y}. \tag{A.1}$$

The orientation of the local basis vectors relative to the Cartesian basis is described by the matrix of direction cosines

$$d_{ij} \equiv \hat{d}_i \cdot \hat{e}_j = \begin{bmatrix} q_1^2 - q_2^2 - q_3^2 + q_0^2 & 2(q_1q_2 + q_0q_3) & 2(q_1q_3 - q_0q_2) \\ 2(q_1q_2 - q_0q_3) & -q_1^2 + q_2^2 - q_3^2 + q_0^2 & 2(q_2q_3 + q_0q_1) \\ 2(q_1q_3 + q_0q_2) & 2(q_2q_3 - q_0q_1) & -q_1^2 - q_2^2 + q_3^2 + q_0^2 \end{bmatrix}, \tag{A.2}$$

where $q_i(s)$ are Euler parameters satisfying

$$q_0^2 + q_1^2 + q_2^2 + q_3^2 = 1. \tag{A.3}$$

Use of the Euler parameters avoids the polar singularities associated with the more familiar Eulerian angles. The ordinary differential equations satisfied by x_i and q_j are

$$x_i' = d_{3i}, \tag{A.4}$$

$$q_0' = \frac{1}{2}(-\kappa_1 q_1 - \kappa_2 q_2 - \kappa_3 q_3), \tag{A.5}$$

$$q_1' = \frac{1}{2}(\kappa_1 q_0 - \kappa_2 q_3 + \kappa_3 q_2), \tag{A.6}$$

$$q_2' = \frac{1}{2}(\kappa_1 q_3 + \kappa_2 q_0 - \kappa_3 q_1), \tag{A.7}$$

$$q_3' = \frac{1}{2}(-\kappa_1 q_2 + \kappa_2 q_1 + \kappa_3 q_0), \tag{A.8}$$

where $\vec{\kappa} \equiv \kappa_i \hat{d}_i$ is the curvature vector that measures the rates of change of the local basis vectors along the jet axis according to the generalized Frenet relation

$$\vec{d}_i\,' = \vec{\kappa} \times \hat{d}_i. \tag{A.9}$$

The velocity of a fluid particle in the jet relative to the rotating reference frame (to first order in the lateral coordinates y_1 and y_2) is

$$\vec{u} = U\hat{d}_3 - \frac{1}{2}U'\vec{y} + \vec{\omega} \times \vec{y}, \tag{A.10}$$

where

$$\vec{\omega} = \kappa_1 U \hat{d}_1 + \kappa_2 U \hat{d}_2 + \omega_3 \hat{d}_3 \tag{A.11}$$

is one-half the vorticity at the jet axis ($y_1 = y_2 = 0$), $U(s)\hat{d}_3(s)$ is the velocity along the axis, and $\omega_3(s)$ is the angular velocity (spin) of the fluid about the axis. The second term on the right-hand side of equation A.10 is the lateral velocity induced by stretching of the axis at a rate U'. The third term represents the velocity associated with bending and twisting of the jet.

Because the base vectors $\hat{d}_i$ are convected with the fluid, their angular velocity as they travel along the jet axis is the sum of the angular velocity $\vec{\omega}$ of the flow and any additional spin that is imparted to the vectors $\hat{d}_1$ and $\hat{d}_2$ when they are injected at ($s = 0$). Now $\hat{d}_1$ and $\hat{d}_2$ can only be steady in the rotating frame if they are injected at

$s = 0$ in such a way as to follow the rotation of the jet as a whole. This is equivalent to imparting to $\hat{d}_1$ and $\hat{d}_2$ and additional spin of magnitude $-\Omega$, where the minus sign accounts for the fact that $\hat{e}_3$ points up and $\hat{d}_3(0)$ down. The evolution equation for $\hat{d}_i$ is therefore

$$U\vec{d}_i\,' = (\vec{\omega} - \Omega\hat{d}_3) \times \hat{d}_i, \tag{A.12}$$

where the left-hand side is the (steady) convective rate of change of $\hat{d}_i$ along the jet axis. Substitution of the Frenet relations A.9 into A.12 yields the fundamental condition for the steadiness of $\hat{d}_i(s)$:

$$\kappa_3 = U^{-1}(\omega_3 - \Omega) \tag{A.13}$$

Equation A.13 allows κ_3 to be eliminated from all the equations that follow.

Equations for the global balance of force and moment in the jet are obtained by integrating the Navier-Stokes equations over the jet's cross-section S. The dynamical variables that then appear are the stress resultant vector

$$\vec{N} \equiv N_i\hat{d}_i = \int_S \vec{\sigma} dS \tag{A.14}$$

and the bending/twisting moment vectors

$$\vec{M} \equiv M_i\hat{d}_i = \int_S \vec{y} \times \vec{\sigma} dS, \tag{A.15}$$

where $\vec{\sigma}$ is the stress vector acting on the jet's cross-section. The quantities N_3, M_1, M_2, and M_3 measure the jet's resistance to stretching, bending in two orthogonal directions, and twisting, respectively. The resultants N_1 and N_2 are the integrals of the shear stresses that accompany bending and twisting, and are generally small.

The integrated balance of forces per unit jet length is

$$\rho A[\vec{\Omega} \times (\vec{\Omega} \times \vec{x}) + 2\vec{\Omega} \times \vec{U} + U\vec{U}'] = \vec{N}\,' + \rho A\vec{g}, \tag{A.16}$$

where $A = \pi a(s)^2$ is the area of the jet's cross-section. The two terms on the right-hand side represent the viscous force that resists deformation of the jet and the force of gravity, respectively. The three inertial terms on the left-hand side represent the centrifugal force, the Coriolis force and the accelerations due to variations in the axial velocity $\vec{U} \equiv U\hat{d}_3$, respectively.

The integrated torque balance is

$$\rho I \vec{K} = \vec{M}\,' + \hat{d}_3 \times \vec{N} + \rho I[(\vec{g} \times \hat{d}_3)\vec{\kappa} - (\vec{\kappa} \times \vec{g})\hat{d}_3], \tag{A.17}$$

where $I \equiv \pi a^4/4$ is the moment of inertia of jet's cross-section and the components of $\vec{K} \equiv K_i \hat{d}_i$ are

$$K_\alpha = U(U\kappa_\alpha)' - \Omega U' d_{\alpha 3} - \Omega^2 \kappa_\alpha d_{3\beta} x_\beta + \epsilon_{\alpha\beta 3}[\Omega d_{\beta 3}(\Omega d_{33} + 2\omega_3) + U\kappa_\beta(\Omega + \omega_3)], \tag{A.18}$$

and

$$K_3 = 2U\omega_3' - 2U'(\Omega d_{33} + \omega_3) + \Omega^2 \kappa_\alpha d_{\alpha\beta} x_\beta + 4\epsilon_{\alpha\beta 3}\Omega U d_{\alpha 3}\kappa_\beta. \tag{A.19}$$

Four additional differential equations appear in the form of constitutive relations for the stress resultant N_3 and the moments M_1, M_2, and M_3. The derivation outlined in [19] yields

$$N_3 = 3\eta A U', \tag{A.20}$$

$$M_1 = 3\eta I[(U\kappa_1)' + \kappa_2(\omega_3 - \kappa_3 U)], \tag{A.21}$$

$$M_2 = 3\eta I[(U\kappa_2)' + \kappa_1(\omega_3 - \kappa_3 U)], \tag{A.22}$$

$$M_3 = 2\eta I \omega_3', \tag{A.23}$$

where η is the dynamic viscosity. Finally, the system of equations is closed by eliminating the jet radius, using the volume flux conservation relation

$$\pi a^2 U = Q. \tag{A.24}$$

Equations A.4-A.12, A.16, A.17, and A.20-A.23 are a system of 17 first-order differential equations with two unknown parameters (Ω and l). Ribe numerically solved these equations with 19 boundary conditions [19], using the program Auto97, [24, 25, 26] and found Ω as a function of H.

Auto97 implements an automatic continuation (homotopy) method, wherein a simple analytical solution of the governing equations that satisfy some boundary conditions but not all of them, and then is gradually adjusted by changing the continuation parameters until the numerical solution satisfies all the boundary conditions. Before solving, the equations and boundary conditions are non-dimensionalized.

For the liquid coiling problem the starting point is an analytical solution of the equations for a (non-coiling) jet having the form of a quarter of a circle in the absence of gravity and inertia, which satisfies five of the boundary conditions. Beginning from this analytical solution with continuation parameters set to zero, the numerical procedure consists in gradually increasing the continuation parameter until a solution of the full coiling problem is reached. Thus "continuation" or "homotopy" method is a general procedure in which an existing solution is changed slightly by varying slightly one or more of the parameters on which it depends.[24, 27]

A.3 Linear stability analysis for instability of liquid coiling in multi-valued regime :

The experiments described in detail in chapter 2 show that steady liquid coiling can in some cases be unstable. In collaboration with Ribe, we used linear stability analysis to investigate this instability [35], here we propose a brief explanation of the calculation that we have used through this thesis. The basic states analyzed are numerical solutions of asymptotic 'thin-rope' equations that describe steady coiling. To analyze their stability, at first a set of general equations for an arbitrary time dependent motion of a thin viscous rope should be derived.

The starting point of analysis is a set of equations governing the unsteady motion of a thin viscous rope, i.e., one whose 'slenderness' $\epsilon \equiv a_0/L \ll 1$, where a_0 is a

characteristic value of the rope radius and L is the characteristic length scale for the variations of the flow variables along the rope. Such equations were derived by Entov and Yarin (1984)[22], who described the geometry of the rope's axis using the principal normal and the binormal from differential geometry. However, such a description leads to numerical instability when the total curvature of the axis is small. Accordingly, we use here an alternative set of equations in which the unit vectors normal to the rope's axis are material vectors that rotate with the fluid [19, 34]. In order to perform a linear stability analysis of steady coiling, the equations were written in a reference frame that rotates with angular velocity $\Omega\mathbf{e_3}$ relative to a fixed laboratory frame. Linearization of these equations about the steady coiling solutions with the boundary conditions yields a boundary-eigenvalue problem of order twenty-one that has nontrivial solutions only for particular values of the growth rate σ. This eigenvalue problem has been solved numerically[35], again using a continuation method implemented by AUTO 97. The basic idea (e.g., Keller [27], p. 235) is to relax one of the homogeneous boundary conditions in order to obtain a nonzero solution for some initial guess at the eigenvalue σ; the homogeneous boundary condition is then reimposed gradually while forcing the solution to remain nonzero and allowing σ to converge to the true eigenvalue. So three new adjustable real parameters β_i $(i = 1, 2, 3)$, should be introduced into the boundary conditions which are then varied gradually to refine an initial guess for the (possibly complex) eigenvalue σ [64]. The problem is initialized by setting $\beta_1 = \beta_2 = \beta_3 = 0$ and making an initial guess for the growth rate σ. The solution procedure then comprises two steps. First, 'pulling' β_3 away from 0 to some finite value (e.g., 1) with σ fixed, letting β_1 and β_2 float freely. Then β_3 is 'pushed' gradually back to 0 with β_1 and β_2 fixed, leaving the real and imaginary parts of σ free to float. At the end of this process, one has both an eigenvalue σ and the full set of associated complex eigenfunctions for the twenty-one perturbation variables. High accuracy is ensured by solving the equations for the steady basic state simultaneously in the same program, on the same numerical grid as the perturbation equations. The resulting system is of order 59 (17 steady variables plus the real and imaginary parts of 21 perturbation variables).

Bibliography

[1] L. D. Landau and E. M. Lifshitz, *Theory of Elasticity*, Pergamon Press, Oxford (1959).

[2] G. I. Taylor, "Instability of jets, threads, and sheets of viscous fluid", *Proc. Intl. Congr. Appl. Mech.* Springer (1968).

[3] J. O. Cruickshank, "Low-Reynolds-number instabilities in stagnating jet flows", *J. Fluid Mech.* **193**, 111–127 (1988).

[4] B. Tchavdarov, A. L. Yarin & S. Radev, "Buckling of thin liquid jets", *J. Fluid. Mech.* **253**, 593–615 (1993).

[5] J. O. Cruickshank & B. R. Munson, "Viscous fluid buckling of plane and axisymmetric jets", *J. Fluid Mech.* (1981).

[6] J. D. Buckmaster, *J. Fluid Mech.*, **61**, 449 (1973).

[7] J. D. Buckmaster, A. Nachman, and L. Ting, "The buckling and stretching of a viscida", *J. Fluid Mech.* **69**, 1 (1975).

[8] M.F. Tome and S. McKee, *Int. J. Numer. Methods Fluids* **29**, 705 (1999).

[9] J.R.A. Pearson, *Mechanics of Polymer Processing*, Elsevier, Amsterdam (1985).

[10] R. W. Griffiths & J. S. Turner, "Folding of viscous plumes impinging on a density or viscosity interface", *Geophys. J.* **95**, 397–419 (1988).

[11] H. E. Huppert, "The intrusion of fluid mechanics into geology", *J. Fluid Mech.* **173**, 557–594 (1986).

[12] M. Skorobogatiy & L. Mahadevan, "Folding of viscous sheets and filaments", *Europhys. Lett.* **52**, 532–538 (2000).

[13] J. G. Ramsay, *Folding and Fracturing of Rocks*, (McGraw-Hill) (1967).

[14] N. M. Ribe, "Periodic folding of viscous sheets", *Phys. Rev. E* **68**, 036305 (2003).

[15] N. M. Ribe, "A general theory for the dynamics of thin viscous sheets", *J. Fluid Mech.* **457**, 255 (2002).

[16] M. Brenner & S. Parachuri, "Thermal bending of liquid sheets and jets", *Phys. Fluids* **15**, 3568–3571 (2003).

[17] L. Mahadevan, W. S. Ryu, & A. D. T. Samuel, "Fluid 'rope trick' investigated", *Nature* **392**, 140 (1998).

[18] L. Mahadevan, W. S. Ryu, & A. D. T. Samuel, "Correction: Fluid 'rope trick' investigated", *Nature* **403**, 502 (2000).

[19] N. M. Ribe, "Coiling of viscous jets", *Proc. R. Soc. Lond. A* **460**. 3223–3239 (2004).

[20] L. Mahadevan and J. B. Keller, "Coiling of flexible ropes", *Proc. R. Soc. Lond.* A **452**, 1679–1694 (1996).

[21] L. Mahadevan and J. B. Keller, *SIAM J. App. Math.* **55**.1609 (1995).

[22] V. M. Entov and A. L. Yarin, "The dynamics of thin liquid jets in air", *J. Fluid Mech.* **140**, 91 (1984).

[23] A. L. Yarin, *Free Liquid Jet and Films: Hydrodinamics and Rheology*, (Wiley) 1991.

[24] Doedel, E. et al. AUTO 97: "Continuation and bifurcation software for ordinary differential equations" (2002). http://indy.cs.concordia.ca/auto/.

[25] E. J. Doedel, H. B. Keller, and J. P. Kernevez, "Numerical analysis and control of bifurcation problems, Part I", *Int. J. Bifurcation and Chaos* **1**, 493 (1991).

[26] E. J. Doedel, H. B. Keller, and J. P. Kernevez, "Numerical analysis and control of bifurcation problems, Part II", *Int. J. Bifurcation and Chaos* **1**, 745 (1991).

[27] H. B. Keller *Numerical Methods for Two-Point Boundary-Value Problems*, Dover, New York (1992).

[28] G. Barnes, & R. Woodcock, "Liquid rope-coil effect", *Am. J. Physics* **26**, 205–209 (1958).

[29] G. Barnes & R. MacKenzie, "Height of fall versus frequency in liquid rope-coil effect", *Am. J. Physics* **27**, 112–115 (1959).

[30] J. O. Cruickshank, "Viscous fluid buckling: a theoretical and experimental analysis with extensions to general fluid stability", Ph. D. thesis, Iowa State University, Ames, Iowa (1980).

[31] M. Maleki, M. Habibi, R. Golestanian, N. M. Ribe, & D. Bonn, "Liquid rope coiling on a solid surface", *Phys. Rev. Lett.* **93**.214502 (2004).

[32] M. Habibi, M. Maleki, R. Golestanian, N. Ribe, and D. Bonn,"Dynamics of liquid rope coiling", *Phys. Rev. E.* **74**, 066306 (2006).

[33] A. L. Yarin and B. M. Tchavdarov, *J. Fluid. Mech.* **307**, 85 (1996).

[34] N. M. Ribe, H. E. Huppert, M. Hallworth, M. Habibi, and D. Bonn, "Multiple coexisting states of liquid rope coiling", *J. Fluid Mech.* **555**, 275 (2006).

[35] N. M. Ribe, M. Habibi, and D. Bonn, "Stability of liquid rope coiling", *Phys. Fluids* **18**, 084102 (2006).

[36] Ribe N M, Habibi M, Bonn D, 2007 "Instabilités de flambage périodique: du laboratoire au manteau terrestre", *Reflets de la physique*, in preparation (invited contribution.)

[37] R. B. Bird, C. Armstrong, O. Hasseper *Dynamics of Polymeric Liquids.*

[38] Darcy Thompson, *On Growth and Form*, Cambridge University Press.

[39] M. P. DO CARMO, *Differential Geometry of Curves and Surfaces*, Prentice-Hall, Inc. Upper Saddle River, New Jersey (1976).

[40] Douady and Couder,*Phys. Rev. Lett.* **68**, 2098 (1992).

[41] Hakim and Karma, *Phys. Rev. E* **60**, 5073 (1999).

[42] A. T. Winfree, *When Time Breaks Down*, Princeton University Press, Princeton, NJ (1987).

[43] V. S. Zykov, *Modelling of Wave Processes in Excitable Media*, Manchester University Press, Manchester (1988).

[44] S. Jakubith, H. H. Rotermund, W. Engel, A. von Oertzen, and G. Ertl, *Phys. Rev. Lett.* **65**, 3013 (1990).

[45] A. T. Winfree, *Science* **181**, 937 (1973).

[46] W. Jahnke, W. E. Skaggs, and A. T. Winfree, *J. Phys. Chem.* **93**, 740 (1989).

[47] T. Plesser et al., *J. Phys. Chem.* **94**, 7501 (1990).

[48] G. S. Skinner and H. L. Swinney, *Physica D* **48**, 1 (1991).

[49] A. Belmonte, Q. Ouyang, and J. M. Flesselles, *J. Phys. II* **7**, 1425 (1997).

[50] W. F. Loomis, *Dictyostelium Discoideum, A Developmental System*, Academic Press, New York (1975).

[51] F. Siegert and J. Weijer, *Physica D* **49**, 224 (1991).

[52] The several review articles in the focus issue of *Chaos* **8**, 1 (1998).

[53] E. Sultan and A. Boudaoud, *Phys. Rev. Lett.* **96**, 136103 (2006).

[54] D. L. Blair and A. Kudrolli, *Phys. Rev. Lett.* **94**, 166107 (2005).

[55] G. A. Vliegenthart and G. Gompper, *Nature Materials* **5**, 216 (2006).

[56] M. BenAmar and Y. Pomeau, *Proc. R. Soc. Lond. A* **453**, 729 (1997).

[57] C. C. Donato, M. A. F. Gomes and R. E. de Souza, *Phys. Rev. E* **67**, 026110, (2003).

[58] A. Goriely and M. Tabor, *Nonlinear Dyn.* **21**, 101 (2000).

[59] J. Coyne, *IEE J. Oceanic Eng.* **15**, 72 (1990).

[60] A. Goriely and M. Tabor, *Phys. Rev. Lett.* **80**, 1564 (1998).

[61] A. Balaeff, C. R. Koudella and L. Mahadevan, *Proc. R. Soc. Lond. A* **362**,1355 (2004).

[62] M. Habibi, N. M. Ribe and D. Bonn, "Coiling of Elastic Ropes", submitted to *Phys. Rev. Lett.*.

[63] A. E. H. Love, *A Treatise on the Mathematical Theory of Elasticity*, Dover, New York.

[64] Neil M. Ribe, John R. Lister and Sunny Chiu-Webster, Stability of a dragged viscous thread: Onset of stitching in a fluid-mechanical sewing machine, *Phys. Fluids* **18**, 124105 (2006).

List of Publications

This thesis was based on the following publications:

1. M. Maleki, M. Habibi, R. Golestanian, N. M. Ribe, & D. Bonn, "Liquid rope coiling on a solid surface", *Phys. Rev. Lett.* **93**.214502 (2004).

2. M. Habibi, M. Maleki, R. Golestanian, N. Ribe, and D. Bonn, "Dynamics of liquid rope coiling", *Phys. Rev. E.* **74**, 066306 (2006).

3. N. M. Ribe, H. E. Huppert, M. Hallworth, M. Habibi, and D. Bonn, "Multiple coexisting states of liquid rope coiling", *J. Fluid Mech.* **555**, 275 (2006).

4. N. M. Ribe, M. Habibi, and D. Bonn, "Stability of liquid rope coiling", *Phys. Fluids* **18**, 084102 (2006).

5. M. Habibi, N. M. Ribe and D. Bonn, "Coiling of Elastic Ropes", submitted to *Phys. Rev. Lett.*

6. N. M. Ribe, M. Habibi, and D. Bonn, " Instabilités de flambage périodique: du laboratoire au manteau terrestre", *Reflets de la physique*,(invited contribution), in preparation.

7. M. Habibi, P. Moller, N. M. Ribe and D. Bonn, "Spontaneous generation of spiral waves by a hydrodynamic instability", submitted to *Euro. Phys. Lett.*.

Résumé:

Dans cette thèse, nous présentons une étude expérimentale des instabilités de flambage hélicoïdal pour un liquide visqueux et une corde. Puis nous comparons nos résultats à un modèle numérique. Nous avons réussi à mettre en évidence l'existence de trois régimes différents pour un filament de liquide. Nous montrons ici que dans une petite région, le flambage de la bobine conduit a l'emprisonnement de bulles d'air d'une manière très particulière, formant ainsi des structures en spirale étonnantes. Nous présentons également un modèle simple qui permet d'expliquer la formation de ces structures en spirale. Nous présentons une étude expérimentale du flambage hélicoïdal pour des cordes et des spaghetti soit lorsque ceux-ci sont poussés contre une surface soit lorsqu' ils sont laissés tomber librement. Nous démontrons qu'il existe trois régimes différents de flambage hélicoïdal possibles. Nous donnons ici un cadre expérimental et théorique pour comprendre le comportement des cordes dans les différents régimes et nous expliquons la relation entre les propriétés élastiques des matériaux et leurs propriétés de flambage hélicoïdal, en particulier avec la fréquence d'embobinage. Les prédictions numériques sont en excellent accord avec les résultats des expériences réalisées.

Summary:

In this thesis, we present an experimental investigation of the coiling instability in a liquid or a solid "rope" on a solid surface and then try to compare the results with a numerical model. We explain different regimes of coiling for a liquid rope (viscous, gravitational and inertial) and present the experimental measurements of frequency vs. height in each regime. We investigate the transition from gravitational to inertial coiling, in this regime the frequency is multivalued and can jump between two frequencies during the time. We show that between any step in frequency vs. height curve we have unstable part. We report that in a relatively small region in gravitational coiling regimes the buckling coil will trap air bubbles in a very regular way, that form spiral patterns. We also present a very simple model that explains how these patterns are formed. We present an experimental study of the coiling of both ropes and spaghetti falling onto a solid surface. We show that three different regimes of coiling are possible. We in addition provide a theoretical and numerical framework to understand and quantify the behavior of the ropes in the different regimes, the numerical predications are in excellent agreement with the experiments.